Electronic Collisions with Molecules of Biological Relevance

Christopher J. Colyer

A thesis submitted for the degree of
Doctor of Philosophy
at the University of Adelaide
March 4th 2011

Table of Contents

Abstract

Experimental studies of radiation damage in living tissue indicate that it is not just the primary ionizing particle responsible for the bulk of the radiation damage, but also secondary species generated by the ionizing particle. There is much interest in how these secondary particles, commonly electrons, interact with bio-molecules and in particular DNA.

In this thesis, I report relative triple differential cross section measurements for the electron impact ionization of formic acid, tetrahydrofuran and thymine. Formic acid can be considered one of the simplest building blocks for biological systems, particularly in the formation of glycine and amino acids. Tetrahydrofuran is a simple ring structure that can be used as a good approximation to the sugar component of the deoxyribose backbone. Thymine, together with cytosine, guanine and adenine, are the DNA bases and their interactions with electrons are considered to be of great importance. Single differential cross sections for elastic electron interactions with cytosine and thymine are also reported.

Declaration

This work contains no material which has been accepted for the award of any other degree or diploma in any university or other tertiary institution to Christopher J. Colyer and, to the best of my knowledge and belief, contains no material previously published or written by another person, except where reference has been made in the text.

I give consent for this copy of my thesis when deposited in the University Library, being made available for loan and photocopying, subject to the provisions of the Copyright Act 1968.

I also give permission for the digital version of my thesis to be made available on the web, via the University's digital research repository, the Library catalogue, the Australasian Digital Theses Program (ADTP) and also through web search engines, unless permission has been granted by the University to restrict access for a period of time.

_____

Christopher J. Colyer

March 4th 2011

Acknowledgements

There are many different organisations that have supported me during my PhD for the last four years that I would like to acknowledge. I would also like to take this opportunity to acknowledge a number of different people, who without their support and assistance this thesis would not be possible.

Firstly I would like to acknowledge the financial support of an Australian Postgraduate Award and further financial support from the Centre for Antimatter-Matter Studies. A big thank you to all the members of the Centre for Antimatter-Matter Studies for many scientific discussions, a host of different professional development opportunities and the opportunity to work with so many different, motivated people who have a common interest. I would also like to acknowledge the many people that I have collaborated with over the last four years. In no particular order, thank you to Igor Bray, Gustavo García, Friedrich Hanne, Don Madison, Ola Al-Hagan and Christophe Champion.

I would like to acknowledge the assistance of the mechanical and electronic staff at the University of Adelaide. Thanks to Blair Middlemiss, Trevor Waterhouse and Neville Wild, and a very special thank you to Peter Apoefis who has been absolutely instrumental in the operation of the laboratory. I would personally like to acknowledge the assistance of the staff of the Flinders University electronics workshop, in particular Bill Drury, Wayne Peacock and John Pesor, for being the only people who could fix a series of very troublesome power supplies. Thank you also to Prof. Michael Brunger for helping me to skip the queue to get work done.

I would like to thank the members of the Laser Lab initially for their hospitality, and later for their friendship. I would personally like to thank Sam Wallace, Mable Fong and Alex Gentleman, all of whom are PhD students who didn't necessarily start at the same time as I but who will hopefully all finish at the same time! Thank you to my co-workers over the past

four years: Dr. Mark Stevenson, Dr. Leigh Hargreaves and Dr. Susan Bellm. Thank you for helping me, educating me and treating me as an equal. I wish you all the very best in your future endeavours.

I would like to thank my associate supervisor, Prof. Jesper Munch for providing administrative advice and support to myself and the other members of my research group, at a university to which we were all very new. Thank you to all the staff and students of the School of Chemistry and Physics for your friendship and support.

I would like to give a very special thank you to my principal supervisor, Prof. Birgit Lohmann. She has not only been a brilliant supervisor who has had to deal with challenging workloads and circumstances of her own and also those of her final student, she has also become a trusted friend. Thank you for the opportunity to work with you, which was a result of good luck rather than good planning, and for all the other opportunities that came with it. It has been a pleasure, and I hope you find success and fulfilment in your new role.

Finally, I would like to acknowledge the love and support of my family. To Kate, my wife, and Melanie, my daughter, I dedicate the publication of this thesis to you.

List of Abbreviations

1CW	One Centre Coulomb Wave
ADC	Analogue-to-Digital Convertor
BBK	Branner, Briggs and Klar
BNC	Bayonet Neill-Concelman
CEM	Channel Electron Multiplier
CF	Conflat
CFD	Constant Fraction Discriminator
CPE	Correlation, Polarization and Exchange
DAQ	Data Acquisition
DDCS	Double Differential Cross Section
DEA	Dissociative Electron Attachment
DNA	Deoxyribose Nucleic Acid
DS3C	Dynamic Screening of Three Two-Body Coulomb Interactions
DSB	Double Strand Breaks
DWBA	Distorted-Wave Born Approximation
EMS	Electron Momentum Spectroscopy
FBA	First Born Approximation
FBA-TCC	First Born Approximation-Two Centre Continuum
FWHM	Full Width at Half Maximum
HOMO	Highest Occupied Molecular Orbital
IAM	Independent Atom Method
ICS	Integral Cross Section
LUMO	Lowest Unoccupied Molecular Orbital
M3DW	Molecular Three-Body Distorted-Wave

MAC	Magnetic Angle Changer
MCP	Microchannel Plate
MTCS	Momentum Transfer Cross Section
NI	National Instruments
NIM	Nuclear Instrumentation Module
OAMO	Orientation Averaged Molecular Orbital
OFHC	Oxygen-Free High Conductivity
PCI	Post Collision Interaction
PSD	Position Sensitive Detector
PTFE	Polytetrafluoroethylene
PWIA	Plane Wave Impulse Approximation
RNA	Ribose Nucleic Acid
SBR	Signal-to-Background Ratio
SCAR	Screening Corrected Additivity Rule
SDCS	Single Differential Cross Section
SS	Stainless Steel
SSB	Single Strand Breaks
TAC	Time-to-Amplitude Convertor
TC	Thermocouple
TDCS	Triple Differential Cross Section
THF	Tetrahydrofuran
TTL	Transistor-Transistor Logic

List of Figures

List of Tables

Introduction

1.1 History of Electron Impact Ionization

The process of electron impact ionization forms one of the most fundamental collision processes in atomic and molecular physics. Collision experiments can probe the kinematics of the emerging particles from an ionizing event. Complete knowledge of the ionization process occurs when the energy and momentum of all collision products are determined. The determined cross sections from ionizing collisions can play a role in understanding plasmas and space radiation, in modelling the effects of radiation damage to biological materials, and even in determining the structure of chemicals and materials.

The electron-electron technique, or (e, 2e), measures the properties of all collision particles, either directly or via conservation rules. Specifically, (e, 2e) experiments refer to electron impact ionization experiments in which an incident projectile electron (E_0, Ω_0) collides with a target atom or molecule and transfers energy to the target resulting in the formation of an ion by ejecting a bound electron from an orbital (ε_i). Both outgoing electrons are then detected in coincidence and whilst indistinguishable quantum mechanically, the faster electron is generally referred to as the scattered electron (E_a, Ω_a), while the slower electron is referred to as the ejected electron (E_b, Ω_b).

To gather the most information about the ionization process, the (e, 2e) coincidence technique is used to measure the triple differential cross section (TDCS). The TDCS is the time independent probability that, after an ionizing collision event, the two outgoing electrons, with precisely defined energies and momenta, will be scattered into particular solid angles.

Scattering experiments are a powerful tool for the investigation of the structure and collision dynamics of a target particle. The first collision experiment is usually considered to be that of Lenard [1], which was published in 1903 and focussed on the absorption of cathode

rays in materials. The most famous of the early collision experiments was conducted in 1911 by Rutherford [2], where α and β particles were scattered through a thin gold foil. Rutherford realised that measuring the angular distribution of the scattered particles determined information relating to the internal structure of the target. Ramsauer [3] performed the first electron scattering experiment in 1921, making use of a single electron beam technique to measure the total electron collision cross section for a series of gases which included H_2, N_2, He, Ne, Ar and Hg.

The first electron impact ionization experiment was published in 1928 when Langmuir and Jones [4] measured the energy lost by the incident electron during a collision with a series of different gas molecules. They reported ionization energies and resonance positions for the same gases as Ramsauer [3], which agreed with previous results. Rudberg [5] performed energy loss experiments for molecular nitrogen in 1930, in an attempt to determine the ionization and resonance energies more accurately. The importance of these two pioneering experiments was discussed in detail by Bethe [6], who utilised the first Born approximation (FBA) to calculate theoretical cross sections for elastic, inelastic and ionizing collisions.

While a majority of the early experiments focused on measuring cross sections that were differential only in energy, more information regarding the ionization process can be obtained by measuring the double differential cross section (DDCS), a measure of the angular or energy distribution for either final state electron. Hughes and McMillen [7] measured the DDCS of Argon in 1932, for a range of electron energies between 50 eV and 550 eV, and in 1938 Hughes and Mann [8] developed a new method for investigating atomic velocities where energy analysis techniques were used to measure electron Compton Profiles.

While important information can be obtained via the DDCS, some of the parameters in the collision process are undetermined, limiting complete knowledge of the ionizing process. Using (e, 2e) coincidence techniques to measure the TDCS, the ionization process can be fully determined with respect to all kinematics of the scattered and ejected electrons. The first coincident results were simultaneously published by Amaldi *et al.* [9] and Ehrhardt *et al.* [10] under different kinematic conditions and with different goals. The (e, 2e) experiments of Amaldi *et al.* used an incident energy of 15 keV for a thin carbon film target, in a coplanar symmetric geometry, where the two outgoing electrons were detected at an equal energy and angle while the incident electron energy was varied. This type of measurement is now known more commonly as a binding energy spectrum. Ehrhardt *et al.* performed coincident (e, 2e) experiments that were in a coplanar asymmetric geometry, where with a fixed scattered electron angle and fixed electron energies the detection angle of the ejected electron was varied. TDCS measurements that are differential with respect to the ejected electron angle are

commonly referred to as angular distributions. Cross section measurements were performed at incident electron energies of 114 eV and 50 eV, with ejected electron energies of 15 eV and 10.5 eV respectively, for a helium target.

While the primary purpose of electron collision experiments is to describe the physical characteristics of the ionization process under investigation, they also serve to determine the validity of the theoretical calculations. Satisfactory agreement between theoretical and experimental studies has been realised for simple atomic systems such as hydrogen [11] and helium [12-13]. At high incident electron energies, theoretical calculations also demonstrate an acceptable level of agreement with the experimental observations for heavier atoms [14-16]. However, for low to intermediate incident energies, the inclusion of all the complex interactions associated with the ionization of polyatomic systems still remains a very challenging endeavour which has been met with limited success by even the most sophisticated calculations.

1.2 Molecular (e, 2e)

Since the laying of the foundations of the (e, 2e) technique by Amaldi, Ehrhardt and others, there have been numerous dynamical (e, 2e) studies for atomic targets, and an equally impressive number of electron momentum spectroscopy (EMS) measurements for molecular systems (see Lahmam-Bennani [17] and Coplan *et al.* [18] for reviews of the former, and McCarthy and Weigold [19], McCarthy [20] and Takahashi [21] for comprehensive reviews of the latter). However, (e, 2e) literature dedicated to the dynamics of molecular systems is limited. Triply differential cross sections for molecular targets can elucidate the molecular effects responsible for perturbations in the cross section. Such perturbations in the TDCS may be influenced by the non-spherical shape of the molecular target, as well as contributions from rotationally and vibrationally excited ground states which may be present after a single direct ionizing collision [22].

The experimental difficulties associated with TDCS measurements for molecular targets arise from the ability of the experiment to resolve different molecular electronic states. Molecular orbitals can, depending on the molecular configuration of the target, be quite closely spaced in energy and contributions from the vibrational and rotational states only add to the challenge. Currently, experimental (e, 2e) results are available for H_2 [23, 22, 24-25], N_2 [26, 22, 27-33], O_2 [34], CO [29], CO_2 [35, 32], N_2O [36], C_2H_2 , H_2O [37-39] and CH_4 [40]. As a result of this thesis, experimental results have been published for formic acid [41] and tetrahydrofuran [42].

The first molecular (e, 2e) results appeared in 1975 when Jung *et al.* [22] performed a series of coplanar asymmetric measurements on molecular hydrogen. Data was recorded at incident electron energies of 100 eV and 250 eV and ejected electron energies of 4.5 eV and 9 eV, for a range of scattered electron angles between 4° and 25°. The effect of the recoiling molecular ion, due to the post-collisional rovibrational states of its electronic ground state, was investigated. Results showed the measured recoil peaks were generally weak in contrast to the observations of atomic targets under similar kinematic regimes. As most experimental (e, 2e) arrangements yield relative cross sections, there is little indication of the magnitude of the TDCS. Absolute experimental H_2 measurements by Cherid *et al.* [24] were carried out at the much higher incident electron energy of 4087 eV, again in the coplanar asymmetric geometry with ejected electron energies of 20 eV and 100 eV. Absolute values were attributed to the cross sections independently by the optical limit method and the Bethe sum rule method. Theoretical calculations using the first born approximation (FBA) and the plane wave impulse approximation (PWIA) were compared to the experimental results. The FBA calculation displayed reasonable agreement with the experimental results, while the PWIA failed to correctly predict both the shape and magnitude of the TDCS. However, it was expected that the PWIA would have difficulty in describing the 20 eV ejected electron TDCS as the impulsive (high energy) conditions were not met. For an ejected electron energy of 100 eV, the kinematic conditions corresponded to the bound Bethe ridge, when the momentum transferred by the scattered electron is equal to the momentum of the outgoing ejected electron, thus the remaining momentum is distributed to the target which is zero. PWIA calculations performed previously for helium under the same conditions showed complete agreement with experiment. The authors attribute discrepancies between the theoretical calculation and the experimental data to the crudeness of the wavefunction used in describing the initial state of molecular hydrogen, prompting further theoretical investigation.

There has been recent theoretical interest in modelling the (e, 2e) process for small diatomic molecules, such as H_2 and its heavier analogues, using both one centre Coulomb wave (1CW) [43-44] methods and distorted wave Born approximation (DWBA) approaches [45-46]. The observation of interference effects via the electron impact ionisation of a diatomic molecule may be expected due to the two molecular centres causing diffraction of the incident electron beam akin to a Young's double slit experiment. The theoretical study of Stia *et al.* [47] predicted that these interference effects should be observable in the TDCS for ionisation of diatomic hydrogen. These interference effects should be observable in the TDCS as a suppression of the recoil peak relative to the binary peak. The experimental observations of Milne-Brownlie *et al.* [25], through comparison of He and H_2 TDCSs at an incident

electron energy of 250 eV for ejected electron energies between 10 and 50 eV, indicated that the angular distribution for the ejected electron is modified due to the Young-type interference from the two molecular centres. A later study by Casagrande *et al.* [23] using a much higher incident energy of 500 eV, with ejected electron energies between 37 and 205 eV, supports this result by comparing the ratio of measured H_2 and He cross sections with the interference factor as predicted by the model of Stia *et al.* [47].

In addition to results published on diatomic hydrogen, Jung *et al.* [22] also performed several coplanar asymmetric measurements on molecular nitrogen. Results were taken at an incident energy of 100 eV and ejected energies of 3 eV and 4 eV, for three scattering angles of -8°, -15° and -25°, again with a view to observe the effect of the recoiling molecular ion. The observations were in agreement with the H_2 experimental data, with N_2 also exhibiting a very weak recoil peak. Avaldi *et al.* [27] obtained absolute N_2 data with coplanar asymmetric kinematics for the $3\sigma_g$ orbital. Maintaining an incident energy of approximately 300 eV, results are recorded for an ejected energy of 10 eV at scattering angles of 3° and 3.5° as well as for an ejected energy of 18.4 eV at scattering angles of 7.2° and 8°. While molecular theoretical models were lacking at the time, comparison was made to helium under the same kinematic conditions. This comparison provided evidence that the shape resonances of the $3\sigma_g$ orbital, known to produce significant deviations to the vibrational branching ratios, can also perturb the TDCS. Doering and Yang [28] published results from a series of coplanar asymmetric experiments investigating the ionization of the $3\sigma_g$ and $1\pi_u$ orbitals of diatomic nitrogen. The study was performed at an incident electron energy of 100 eV, at a scattering angle of 4° and for a range of ejected electron energies between 3 eV and 13 eV. In the N_2 TDCS the binary and recoil peaks were not centred about the momentum transfer direction as anticipated, rather towards larger and smaller ejected angles for the binary and recoil peaks respectively. Also, despite the small 1.1 eV difference in ionization potentials, there are distinctive differences in the TDCS of the two orbitals, which indicates that the TDCS is sensitive to the initial and final states of the molecular target under this kinematic condition.

Coplanar symmetric measurements of N_2 were performed by Rioual *et al.* [29] at incident electron energies between 90 eV and 400 eV. The TDCS exhibit satellite structures arising from the overlap of several different states of the molecular target, an effect permitted by the relatively high energy resolution of the apparatus. Comparison was also made to PWIA calculations, however the theoretical calculations did not accurately describe the experimental data. Hussey and Murray [30] also performed coplanar symmetric measurements of N_2, at incident electron energies of 25.6 eV and 76.7 eV with a view to studying the $3\sigma_g$ and $1\pi_u$ orbitals. In agreement with the work in coplanar asymmetric kinematics of Avaldi *et al.* [27],

the N_2 TDCS was shown to be sensitive to contributions from shape resonances.

For the $3\sigma_g$ state of molecular nitrogen, Gao *et al*. [48] have calculated cross sections in coplanar symmetric kinematics at incident electron energies between 35.6 and 400 eV using a distorted wave impulse approximation (DWIA) approach. By utilising a molecular wavefunction that was averaged over all orientations, calculations were greatly simplified. A comparison was made between the DWIA and the available experimental data of Rioual *et al.* [29] and Hussey and Murray [30]. The theoretical calculation was in reasonable agreement with both experiments at intermediate and high incident electron energies, but deteriorated for low incident energies. In a comparison between the DWIA and a PWIA, the DWIA showed better agreement with the experimental data, particularly at intermediate incident electron energies, with the PWIA failing to reproduce the secondary peak. Although the DWIA was able to predict the secondary peak, only qualitative agreement was achieved with experimental data. The authors highlight the success of the orientation averaging, suggesting its use in simplifying more complex theoretical approaches, and later Gao *et al.* [49] published results for the $3\sigma_g$ state of N_2 via a distorted wave Born approximation (DWBA) and a molecular three-body distorted wave (M3DW) calculation. Both coplanar symmetric and asymmetric kinematics were investigated, with incident energies in the range of 35.6-400 eV. For the symmetric arrangement, the M3DW approach yields reasonable agreement while the DWBA calculation could not correctly predict the behaviour. However, the authors previous DWIA calculations [48] still compared best to the available experimental data. In the asymmetric arrangement, the M3DW approach accurately predicts both the shape and relative magnitude of the available data, while the DWBA fails to predict the relative magnitude. This difference is attributed to post collision interaction (PCI) which is fully accounted for in the M3DW calculation, but only to first order for the DWBA approach.

Molecular nitrogen was again the subject of a later study by Naja *et al.* [31], measured in the coplanar asymmetric geometry with 600 eV incident electrons for 74 eV ejected electrons. Measurements were presented for a sum of the outer orbitals ($3\sigma_g$, $1\pi_u$ and $2\sigma_u$) as well as a separate measurement for the inner $2\sigma_g$ molecular orbital. The experimental results are characterised by a shift towards larger angles with respect to the momentum transfer direction, and a large intensity in the recoil region which occurred as a result of the large amount of momentum transferred to the target. The distributions are compared to the theoretical results of the first Born approximation-two centre continuum (FBA-TCC) model and the M3DW model with the inclusion of orientation averaged molecular orbitals (OAMO). Unfortunately, both calculations failed to reproduce the experimental cross sections, and there is some discrepancy between the absolute values of the predicted TDCSs. These orbitals and

kinematics are again probed in the later study of Lahmam-Bennani *et al.* [32], this time with the consideration of two alternate ejected electron energies, namely 37 eV and 205 eV. In this instance the results are compared solely with FBA-TCC model, which again fails at reproducing the observed shifts toward larger angles and the enhancement of the recoil intensity.

The possibility of seeing interference effects in diatomic molecules has also generated interest in molecular nitrogen as a source of Young double slit interference effects. A study of Gao *et al.* [50] predicted a strong interference effect for the ionisation of the $3\sigma_g$ state of N_2 for highly asymmetric collisions. At small scattering angles it was predicted that there would be a large interference peak near an ejected angle of 180°. Murray *et al.* [33] investigated this effect at larger scattering angles, specifically at -22°. Utilising a magnetic angle changer, a normal binary peak plus a smaller back angle peak in the vicinity of 180° is observed, supporting the possibility of Young's type interference. A M3DW calculation is also presented, and the authors highlight that the inclusion of a polarisation factor greatly reduces the magnitude of the theoretical cross section in this backward angle region to approximately the size of the measured TDCS. The more recent study of Hargreaves *et al.* [26] investigates the matter of interference effects by two separate approaches. Firstly, using asymmetric kinematics and incident and scattered electron energies of 150 eV and 10 eV respectively, the suppression of the molecular recoil peaks by comparison to atomic recoil peaks is observed in accordance with the two-centre predictions. A second method was used that involved a lower incident energy of 75 eV and symmetric energy between the two final state electrons. These results agree well with the previous study of Murray *et al*. [33], as well as an improved version of the M3DW calculation which now included the two centre distortion potentials. The peak in the TDCS at approximately 180° was still present in the improved M3DW calculation, however calculations using different nuclear separation distances suggested that this peak was not a result of two-centre scattering but instead due to an alternate type of undetermined interference.

The only (e, 2e) measurements for molecular oxygen to date were published by Yang and Doering [34], who observed the ionization of the $1\pi_g$, $1\pi_u$ and $3\sigma_g$ states. Results were recorded at a common incident electron energy of 100 eV and scattered electron angle of -4°, with ejected electron energies of 3.5 eV, 6 eV and 11 eV. The observations of Yang and Doering are compared to the available N_2 data since the $1\pi_u$ and $3\sigma_g$ orbitals are common to both molecular targets, albeit that the ionization energies are reversed. The binary lobe of the O_2 cross sections were reported to be quite similar to those for the corresponding N_2 orbital, except that the binary lobe maxima are shifted away from the momentum transfer direction to

larger angles. This suggested that the shape of the molecular orbital is more important than its energy assignment. Comparison between O_2 and N_2 in the recoil region showed remarkably different cross sections, which still remains an unanswered question.

In addition to their results on N_2, Rioual *et al.* [29] also recorded measurements for the 5σ, 1π, 4π and 3σ states of carbon monoxide using the coplanar symmetric geometry. A series of results were obtained for incident electron energies between 90 and 400 eV. Similar to their N_2 measurements, several satellite structures due to the overlap of molecular states were observed. In a comparison of the CO experimental data to a PWIA calculation, under equivalent energy conditions, the experimental cross sections were not well reproduced.

A series of coplanar symmetric measurements on the $1\pi_g$ and $4\sigma_g$ orbitals of carbon dioxide were performed by Hussey and Murray [35], at incident electron energies between 25 eV and 100 eV. Due to a lack of theoretical data, results were compared to previous N_2 studies [30] as the characteristics of the molecular orbitals are similar. A clear difference was observed between CO_2 and N_2, which the authors attributed to the configuration of each molecular target. More recently, Lahmam-Bennani *et al.* [32] published coplanar asymmetric data for the $1\pi_g$ orbital for intermediate impact energies between 500 eV and 700 eV, and ejected electron energies of 37 eV and 74 eV. The scattered electron angle was chosen to be -6° to ensure a large momentum transfer and as a result enhance the size of the recoil peak. It was noted that the cross sections exhibit narrow binary lobes centred about the momentum transfer direction, similar to their measured data for N_2.

A number of N_2O measurements were obtained by Cavanagh and Lohmann [36] using coplanar asymmetric geometry at a common incident electron energy of 900 eV and an ejected electron energy of 25 eV. Data was recorded for the valence 2π orbital at scattering angles of -2°, -5° and -10°, and for the inner valence 4σ orbital at a scattering angle of -5°. For the 2π state, the most significant feature was seen at a scattering angle of -10°, which corresponds to the Bethe ridge condition, where a double lobe structure is seen in the binary region. However, at a scattering angle of -5° the minimum of the binary double lobe is scarcely pronounced. For a scattered electron angle of -2° the magnitude of the recoil peak was larger than expected and the maxima of the binary and recoil lobes were shifted, similar to the observations of Doering and Yang [28] for N_2. The separation spectra of N_2O indicated that there are many satellite structures between 20 eV and 42 eV, and as a result ionization of the broad 4σ orbital, which lies within this region, could not be resolved completely. Observations of the 4σ orbital showed a smaller than expected binary to recoil ratio, possibly due to a localised interaction of the ejected electron with the molecular target [36].

Theoretical (e, 2e) studies focussed on water have been conducted by Champion *et al.*

[51], chiefly with a view to understanding radiation damage to biological media. The effects of target orientation on the fully differential cross sections of H_2O were investigated using a DWBA approach, and angular distributions were presented for scattering angles of 0° and -15° highlighting the contributions from each molecular orbital. Using the calculated cross sections as inputs for a Monte-Carlo type simulation [52], it was possible to predict the coordinates for electronic interactions with water vapour as well as the energy deposited at each event and the corresponding type of interaction. An experimental investigation on H_2O by Milne-Brownlie *et al.* [38] presented cross sections for the $1b_1$, $1b_2$, $2a_1$ and $3a_1$ molecular orbitals in the coplanar asymmetric geometry, at a common incident energy of 250 eV, ejected electron energy of 10 eV and scattered electron angle of -15°. The cross sections exhibited very large recoil structure, indicative of strong higher order interactions, which were not predicted by the DWBA calculation. In response to this, Champion *et al.* [53] considered more sophisticated models to better understand the ionisation process of water at the multiply differential level. Good agreement was observed between theory and experiment for the highly sophisticated Branner, Briggs and Klar (BBK) and dynamic screening (DS3C) approaches, with the magnitude of the recoil lobe being correctly predicted, but even they failed to reproduce the data correctly at low ejected electron angles. Kaiser *et al.* [39] published a series of experimental data for H_2O at incident electron energies between 15 eV and 95 eV above the ionisation threshold of the $1b_1$ molecular state in both the coplanar symmetric and asymmetric geometries. A DWBA calculation was also presented that incorporated the final state post collision interaction, finding only qualitative agreement with the experiment at low to intermediate energies, rather than in the high energy regime. Most recently, for the $3a_1$ molecular state of water, Nixon *et al.* [37] presented experimental and theoretical cross sections in symmetric coplanar and an out-of plane geometry termed intermediate plane, where the angle of the incident electron with respect to the plane of the final state electrons is varied. Incident energies were kept low, between 4 eV and 40 eV above the ionization threshold, while measurements were made with both equal and unequal energy sharing of the final state electrons. The authors note that the shape of the TDCS of the $3a_1$ molecular orbital has a similar structure to the $1b_1$ orbital measured in a previous study [39], with the absence of a second peak in the forward region that appears at higher incident energies. They report mixed agreement between the theoretical models, with the best results coming at low incident energies where one might expect the approximations to be least accurate. The two models are both M3DW type, one of which only includes PCI to first order. However it was this model that was found to be more successful, which suggested that the M3DW calculation with PCI included to all orders may actually be overestimating the effects

of PCI.

Cross sections for C_2H_2 were recently measured in a dynamical (e, 2e) study. Ionization of the innermost carbon 1σ orbital was investigated by Avaldi *et al.* [54] under coplanar asymmetric conditions, at a common scattering electron energy of 1500 eV and small scattering angles, while two values were selected for ejected electron energies, 9.6 eV and 41 eV. The authors observed a large recoil lobe, and a large deviation of the symmetry axis for both the binary and recoil lobe from the momentum transfer direction. Upon comparison with a FBA calculation, it was concluded that the theoretical model did not adequately include PCI and higher order scattering effects. The magnitude of the recoil peaks was underestimated and the severe shift in the position of the binary and recoil maxima was not accounted for.

Methane (CH_4) is, with the exception of those in the present study, the largest molecule studied in a dynamical (e, 2e) investigation. Conducted by Lahmam-Bennani *et al*. [40], the triple differential cross section was measured for the outer ($1t_2$) and inner ($2a_1$) valence orbitals of methane under coplanar asymmetric kinematics. Measurements were made for a fixed scattered electron energy and angle of 500 eV and -6°, and for three separate ejected electron energies of 12 eV, 37 eV and 74 eV. The experimental cross sections exhibited a large amount of recoil scattering, particularly for the $2a_1$ orbital, which the presented theoretical 1CW and BBK calculations failed to reproduce. The BBK is found to satisfactorily reproduce the experimental angular distributions in the binary region, however there is some deterioration of the cross section quality for the inner valence orbital at large momentum transfers. This study was followed by the theoretical predictions of Tóth and Nagy [55] who use both electron screening and total screening versions of the DWBA approach. The authors reported good agreement with the experimental data for both orbitals, particularly with the total screening treatment. The advantage that these two theories presented had over both the BBK and 1CW calculations published in [40] was that they were able to reproduce the double peaked structure of the binary peak.

1.3 Ionizing Radiation

Ionizing radiation is used widely in medicine as a probe in radio-diagnostic examinations, as a treatment method for many forms of cancer, in industrial production as a means of quantifying internal defects and even in smoke detectors. Traditionally, damage to biological systems by high energy incident radiation was thought to be caused by high-energy ballistic impacts of the incident radiation. As the radiation travels through the biological medium, its energy is redistributed via elastic and inelastic collisions, which results in the production of an

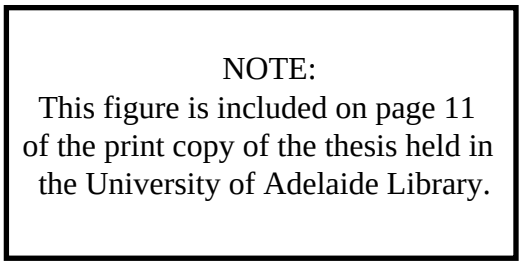

Figure 1.1: Measured quantum yields, per incident electron, for the induction of (a) DSB, (b) SSBs and (c) loss of the supercoiled DNA, in DNA solids by low energy electron irradiation as a function of incident electron energy. The curves are a β-spline fit to the data and serve to guide the eye only. Data obtained from Boudaïffa *et al.* [56]. The peaks in each of the yields at approximately 10 eV are a result of resonant scattering processes that result in the dissociation of the DNA subunits.

abundance of secondary species. In recent years, theoretical and experimental studies have indicated that secondary species generated by the primary ionizing particle can also play a significant role in radiation damage to biological media [57].

Upon entering the body, the high energy ionizing radiation quickly thermalises through various scattering processes, such as excitation and ionization, which liberate large numbers (approximately 2000 per MeV of incident radiation) of low energy (0-20 eV) secondary electrons with very small interaction lengths in the order of a few nanometres.

Figure 1.2. Example of an actual simulated α-particle track from Goodhead [58]. The path of the 4 MeV incident particle is clearly seen by the straight black line. Large red circles represent ionization events and small purple circles represent excitation events. The dashed grey lines indicate the paths of the secondary electrons that arise from ionization. The total number of ionization events due to secondary electrons is 25, greater than the 18 induced by the α-particle.

These electrons can then interact with constituents of biological systems such as water [59], sugars [60], organic acids [61] and the DNA bases [62-67]. In the seminal study of Boudaïffa *et al*. [56] it was observed that electrons in the energy range 3-20 eV, and observed later by Martin *et al*. [68] for electrons in the 0-4 eV energy range, can cause significant damage to DNA through the process of dissociative attachment, which can occur even at energies well below ionization thresholds via resonant scattering processes, as shown in figure 1.1 This can lead directly to single strand breaks (SSB) or double strand breaks (DSB) of the DNA chain, or can result in the formation of ionic products as well as free radicals, which may then chemically react with DNA to lead to strand breaking. It is now thought that this mechanism accounts for the majority of cellular damage initiated by high-energy radiation [63].

1.4 Charged Particle Track Structure Analysis

Since radiation damage is a result of the primary and secondary particles, it is therefore desirable to model their trajectories through a biological medium. In this way, the nature, location and intensity of cellular damage can be understood, predicted and controlled. This is done by calculating the path along which the primary and secondary species move as they pass through matter, known as their charged particle track structures (see figure 1.2 for an example. In particular, high concentrations of ionizations near the track ends of low energy

electrons can cause a clustering of damage, giving a higher probability of permanent cell damage [58]. These clusters, with dimensions of the order of the DNA helix and larger, are of importance when determining the resultant effect on the biological system. An excellent overview of track structures and their use in calculating radiation damage is given by Hill [69].

The study of the effect of radiation on matter goes back several decades [70]. Calculations of track structures involve Monte Carlo simulations to calculate individual events along a radiation track. The full history of interactions (elastic collisions, ionizations, excitations) of the primary and secondary electrons are accounted for on an individual atomic or molecular basis. The simulations incorporate experimental cross section data or theoretical calculations where the former is not available. As biological matter is usually greater than 50% water, and due to the lack of cross section data for other biomolecules, the simulations are usually based solely on water cross section data. It is assumed that the track interactions in water are a suitable representation to those in DNA. Such cross section measurements are usually undertaken on water in the gas phase, whereas biological systems contain water in the liquid phase, and as such some ambiguity exists over the ability of gas phase cross sections to accurately represent liquid phase situations [71-72].

Calculations performed by Nikjoo and Goodhead [70] were undertaken to determine the extent of the role of secondary electrons. They estimated that up to half of the energy of the primary radiation is transferred to secondary electrons, in the range 0.1-5 keV, which were particularly effective at producing highly localized clusters of damage. An attempt to characterise the spectrum of damage caused by secondary electrons was made by both Goodhead [58] and Nikjoo *et al.* [73]. Their methods involved superimposing a charged particle track structure over a segment of DNA. This was repeated several times for many different orientations and track structures until a statistically meaningful picture was created. The areas of concentrated radiation damage were then considered to be the most probable points of interaction for the given set of orientations. This type of simulation reveals details about the nature and frequency of strand breaks in DNA.

A large range of Monte Carlo track structure simulations have since been developed. The review of Nikjoo *et al.* [74] summarises and attempts to benchmark no less than 20 different codes. Codes are categorised according to their nature, such as 1D deterministic description, amorphous track codes, Condensed-history Monte Carlo, 3D and 4D (incorporating chemical track) codes. Details of these codes and their different applications are reviewed in Nikjoo *et al.* [72]. It is the 3D and 4D codes that contain individual physical events and incorporate scattering cross sections, and an example of the calculations of such a

code is given in the review. Total ionization and excitation cross sections provide information about the likelihood of an interaction event, and can describe interaction lengths. Multiply differential cross sections, usually the double differential or triple differential cross sections, elucidate spatial information about the interactions, such as the direction of particles after the collision.

As stated previously, the majority of track structure analyses for biological systems focus on water as the primary species in the system, but the inclusion of contributions from other targets present in the biological media is needed for a complete and accurate description of the process. Unfortunately, there still remain a vast number of important biological molecules for which there are no cross section measurements.

1.5 Summary of Thesis

In this thesis, a range of TDCS measurements are presented for the molecular targets formic acid, tetrahydrofuran (THF), and the DNA base thymine. Results are presented in the low to intermediate incident energy regime, as measured on a conventional coincidence spectrometer in the coplanar asymmetric geometry. Due to the difficulty in collecting (e, 2e) cross sections from the DNA bases, elastic differential cross sections are also presented for thymine and cytosine. Comparisons have been made to available theoretical calculations or extant experimental data.

The majority of electron impact ionization processes are single ionization, and chapter two discusses the techniques used to probe this process. Specifically, this chapter deals with the different types of cross section measurements and discusses the different kinematic arrangements available for measuring TDCSs, highlighting the key features of a typical measurement in each given geometry.

The third chapter will discuss the experimental and technical characteristics of the electron coincidence spectrometer utilised during the measurement of the cross sections presented within this thesis. A detailed description of the individual components of the spectrometer including the vacuum chamber, gas source, electron gun, hemispherical analysers, fast timing electronics and the computer control is provided. Chapter three also includes an overview of the coincidence technique with a focus on the coincidence energy resolution and coincidence timing and data collection. Finally, several steps have been undertaken to ensure the reliable operation of the experimental apparatus. These procedures will also be discussed here, and include the alignment of the spectrometer, energy and angular calibration of the spectrometer and spectrometer consistency checks.

Chapter four presents dynamical (e, 2e) results for the electron impact ionization of formic acid, as well as the structure and properties of formic acid and the motivations for considering it as a suitable target. The TDCSs have been measured at two discrete incident energies: a lower value of 100 eV and a higher value of 250 eV. TDCS are presented for three different scattered electron angles of 5°, 10° and 15°, whilst the ejected electron energy remains fixed at 10 eV. Due to the coincidence energy resolution of the experiment, a sum of the ionization of the outer valence orbitals (10a′ +2a″) is presented.

Chapter five presents dynamical (e, 2e) cross sections for the electron impact ionization of tetrahydrofuran, as well as its structure and use as a DNA analogue. The TDCSs have been measured solely for 250 eV incident electrons, with 10 eV ejected electrons and for three separate scattering angles of -5°, -10°, and -15°. Ionization of the outermost valence orbital (12a/9b) of tetrahydrofuran is measured.

Chapter six presents the first dynamical (e, 2e) results for the electron impact ionization of the DNA base thymine. The TDCSs presented here were measured for the sum of two inner valence orbitals (2a″+14a′) with 250 eV incident electrons, 20 eV ejected electrons, and for two different scattering angles of -10° and -15°. Elastic single differential cross sections for a range of energies from 60-500 eV are also presented for cytosine and thymine. The results are compared to recent theoretical calculations and existing experimental data for similar chemical structures, namely pyrimidine, where available.

The final chapter, chapter seven, will summarise the work presented within the thesis. Future directions to be undertaken experimentally will also be outlined in this section.

Appendix A contains the experimental data for the binding energy spectra and triple differential cross sections of formic acid, tetrahydrofuran and thymine. Appendix B contains the experimental data for the elastic differential cross sections of cytosine and thymine.

In keeping with the convention of experimental atomic and molecular physics, all electron energies are stated in electron volts (eV).

Fundamentals of Electron Collisions

2.1 Overview

In an electron collision experiment, an incident projectile electron collides with a target atom or molecule. During the event, there are several collision processes that may occur, which can be broadly defined into three categories: super elastic, elastic and inelastic processes. Super elastic scattering is a term that is used to describe processes where an excited target, generally achieved via a pump laser, is de-excited by the projectile electron, which then leaves the scattered electron with more energy than it was incident with [75]. Recently however, super elastic experiments where the excited target is produced by thermal heating of a molecular source have become more frequent [76-77]. Elastic collisions are defined as collision events where there is no change in the energy or internal structure of the target or the incident electron. These are the most likely type of collision to occur, and elastic scattering measurements are plentiful in the literature for all but the most exotic targets (see [78-79] for example). This thesis will consider some elastic interactions, but the DNA bases are the sole targets of interest in that regard. During an inelastic process however, the incident projectile transfers energy to the target particle, which as a result undergoes a change in its internal structure. There are a number of inelastic collision processes, such as rotational, vibrational and electronic excitation and dissociative electron attachment (DEA). The primary focus of the present study is the electron impact ionization process.

2.2 Elastic Collisions

Elastic scattering can be classified into two distinct groups based on the mechanism by which they interact: direct scattering and exchange scattering. Direct scattering refers to events where the incident electron is scattered by the target, whereas exchange scattering implies that

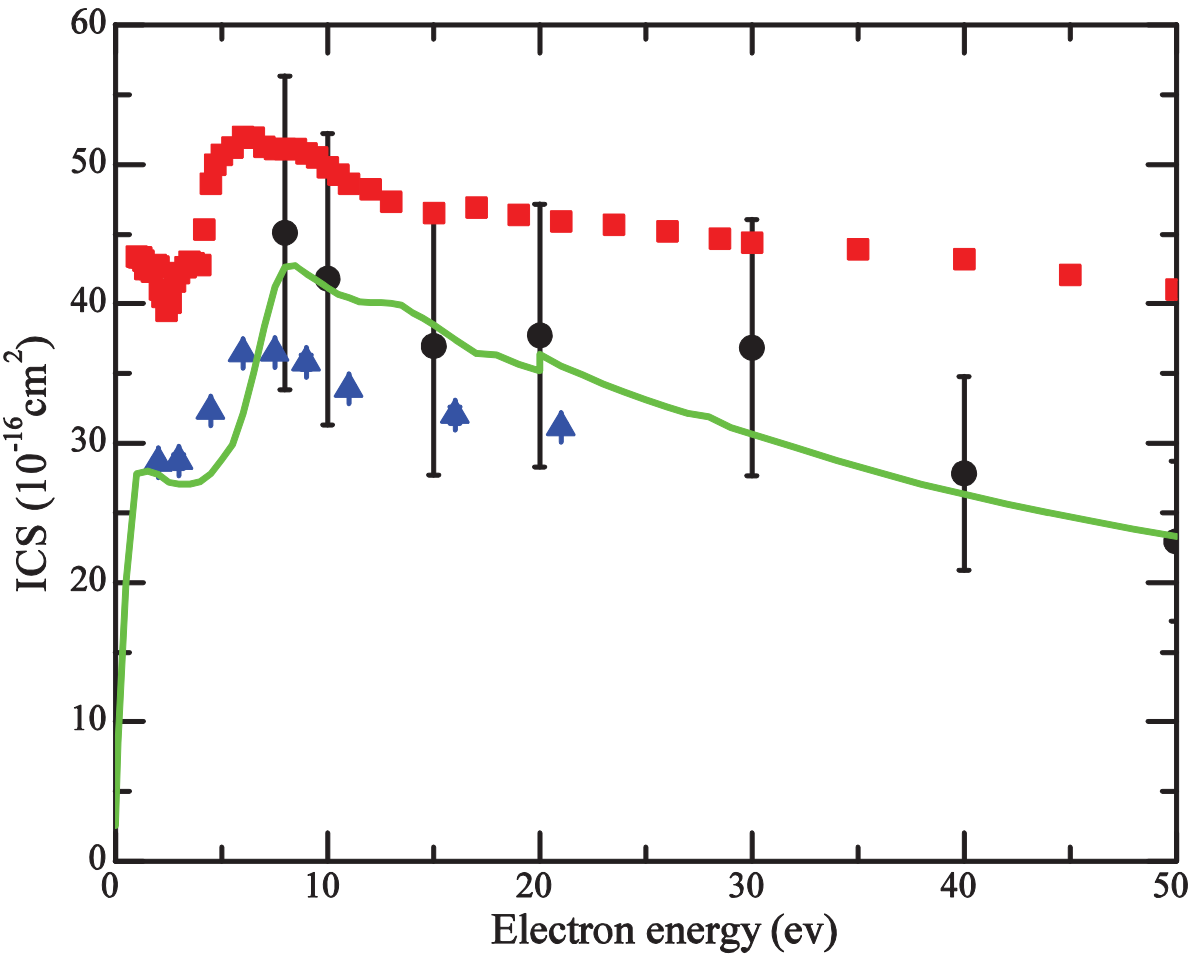

Figure 2.1: An example of an elastic integral cross section (solid black circles) for tetrahydrofuran as measured by Colyer *et al.* [80]. It is compared to the theoretical calculation for the elastic ICS (solid green line) of Winstead and McKoy [81], as well as two independent measurements of the grand total cross section by Możejko *et al.* [82] (solid red squares) and Zecca *et al.* [83] (solid blue triangles).

the incident electron is interchanged with an electron from the target during the collision process. Exchange scattering arises from the indistinguishability of the projectile and target electrons, which also makes it difficult to measure. Exchange scattering effects for electrons [84], and indeed for other particles [85], have been observed to be responsible for a fair proportion of the intensity in elastic cross sections at backward angles. The effects of the exchange mechanism are usually masked by the use of unpolarised electron sources [86]. The use of spin-polarised sources, as well as spin analysis of the scattered electron beam, can provide information about the role of exchange in collisions by measuring the spin-flip cross sections of open-shell targets [86].

Scattering mechanisms can be classified further as dipole scattering, impact scattering and resonance scattering. The motivation of the different mechanisms can be illustrated using wave-particle duality. In dipole scattering, the oscillating electric field associated with the charge of a moving electron interacts with the target molecule, thus having a long range

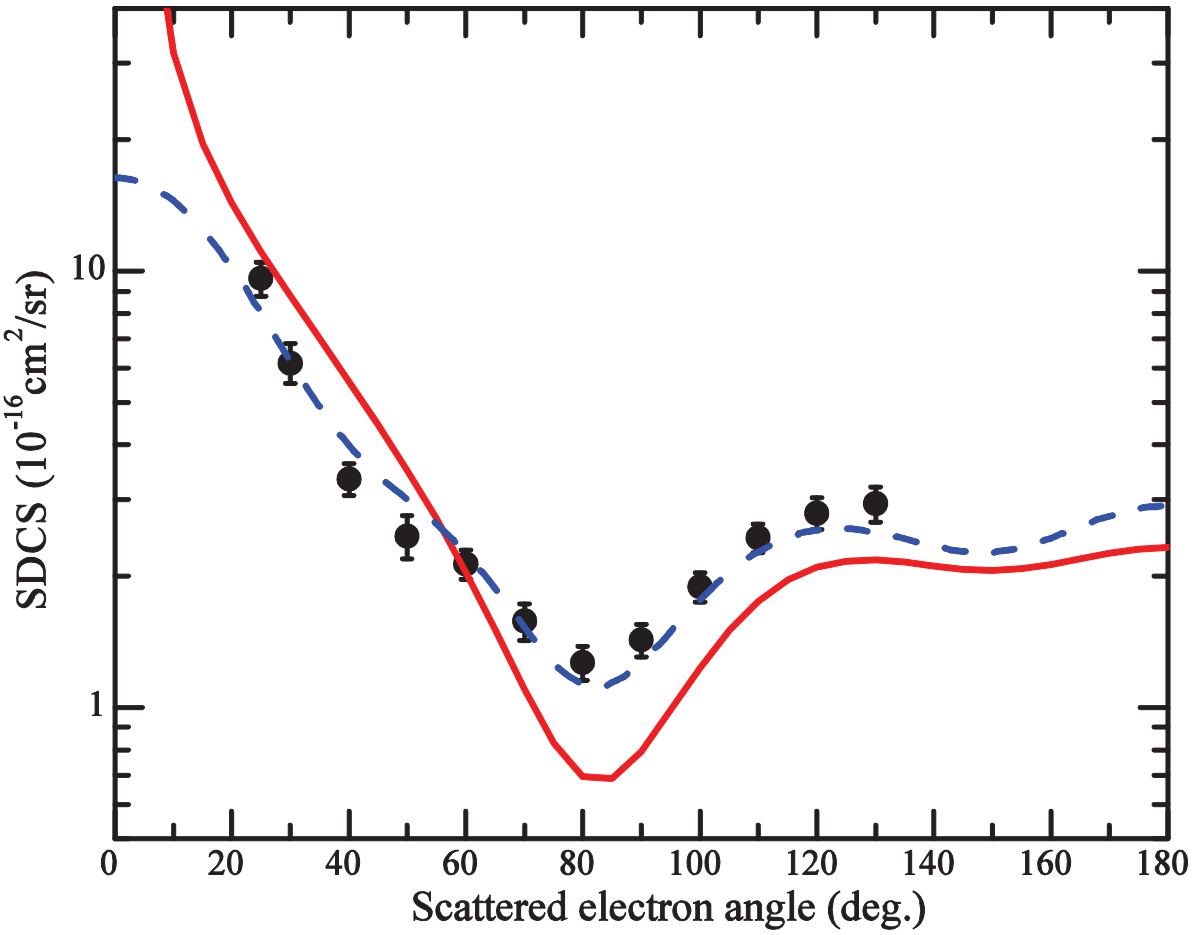

Figure 2.2: An example of an absolute single differential cross section for elastic electron scattering from tetrahydrofuran at an incident energy of 6.5 eV. The experimental results of Colyer *et al.* [80] (solid black circles) are compared to two independent theoretical calculations: that of Trevisan *et al.* [87] (solid red line) and Winstead and McKoy [81] (dashed blue line).

interaction via its electric field [88]. This mechanism is strongly correlated with the magnitude of the target molecule's dipole moment and is responsible for the bulk of collision events at forward electron angles. On the other hand, in impact scattering the electron undergoes a ballistic collision with the target molecule, experiencing a short range interaction and exchanging momentum [88]. Conversely, this scattering mechanism is responsible for the bulk of intensity in the elastic collision cross section at backward angles.

Resonance scattering is distinctly different to the other two direct scattering mechanisms, in that upon interaction with the target molecule the electron can become trapped in a bound or quasi-bound electronic state [88]. The trapping state can be a real excited state of the molecule, commonly the lowest unoccupied molecular orbital (LUMO), resulting in a state known as a Feshbach resonance. Alternatively, a centrifugal barrier arising from the angular momentum associated with the target rotating during the scattering event can trap an electron. This is termed as a shape resonance, and it is a state with a very short

lifetime, in the order of 10^{-15} seconds, whereas a Feshbach resonance can have a comparatively longer lifetime, up to 10^{-10} seconds [88]. Resonance scattering is very sensitive to the incident electron energy, requiring specific quantities of energy to penetrate the charge cloud of the molecule, and as such occurs at specific energies in the target cross sections. These resonances also have characteristic angular dependencies, and as such the angular distribution of the electrons scattered via a resonance can provide information about the symmetry of the resonant state [88]. As elastic scattering involves only a single particle it is only possible to define two types of cross section: the integral cross section (ICS) and the single differential cross section (SDCS). An example of each of these is given in figure 2.1 for the ICS and in figure 2.2 for the SDCS.

2.3 Ionization

Electron impact ionization strictly refers to the removal of single or multiple electrons from a target particle as a result of a collision between an incident electron and the target. Many different terms can be used to describe the ionization process. Direct ionization refers to a clean removal of an electron from the target with little nuclear interaction. In contrast, resonant ionization occurs via a resonant process some time after the initial collision has taken place. Autoionization is an example of this, whereby an incident electron excites two valence electrons in the target, which then lose energy via the emission of an electron. Single or multiple ionization indicates the number of electrons that are ionized from the target, and thus the magnitude of positive charge on the final state ion. The shell from which the ejected electrons originate can also be used to describe the ionization process, such as an inner shell ionization event where a large amount of energy is required to liberate an electron, or outer shell ionization where electrons are liberated more freely.

The direct single ionization of a ground state target particle *A* by electron impact can be described by:

$$e^- + A \rightarrow A^+ + e^- + e^- \tag{2.1}$$

where A^+ is the ion produced by the collision. The most likely process is the ejection of an electron from the valence shell while the ion remains in the ground state. The motion of the remaining ion can be neglected due to the much greater mass of the ion. Equation (2.1) can then be written more explicitly as:

$$e^-(E_0, \boldsymbol{k}_0) + A \rightarrow A^+ + e^-(E_a, \boldsymbol{k}_a) + e^-(E_b, \boldsymbol{k}_b) \tag{2.2}$$

where E_0, E_a, E_b and $\boldsymbol{k}_0$, $\boldsymbol{k}_a$, $\boldsymbol{k}_b$ are the kinetic energies and momenta of the incident, scattered (fast) and ejected (slow) electrons respectively. During the collision, energy and momentum

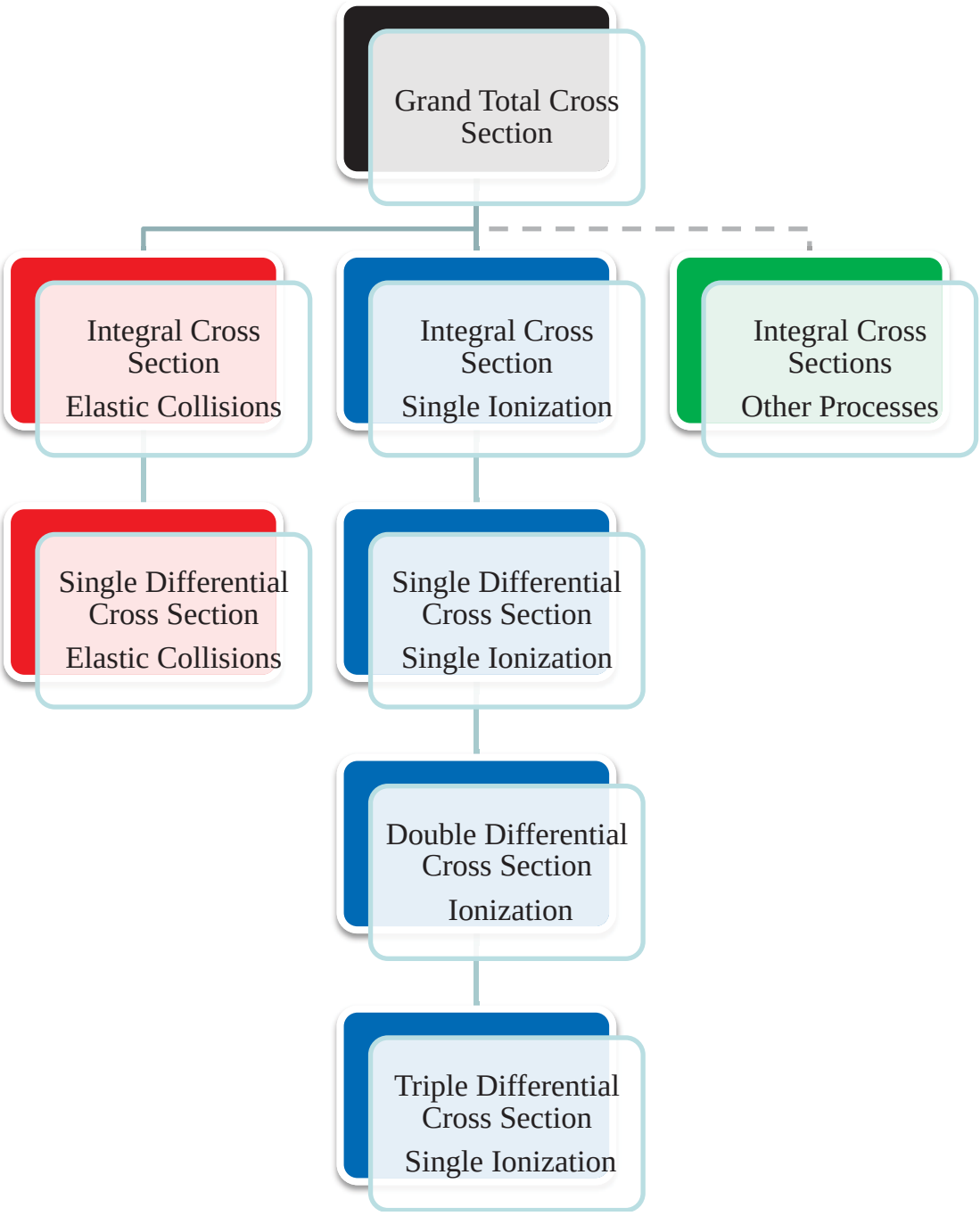

Figure 2.3: The hierarchy of cross sections. Each cross section can be obtained by integrating the cross section of the type below it. For example, one can obtain a single point of a double differential cross section by integrating across the entire angular range (of one of the final state electrons) of a triple differential cross section. Cross sections toward the top yield more information about total scattering events, whereas cross sections toward the bottom contain more information about individual processes.

must be conserved such that:

$$E_0 = E_a + E_b + \varepsilon_i \tag{2.3}$$

$$\boldsymbol{q} = \boldsymbol{k}_0 - \boldsymbol{k}_a - \boldsymbol{k}_b \tag{2.4}$$

where ε_i is the ionization potential of an electronic orbital in the target species. The recoil energy of the ion is small compared to the energy of the other particles and is neglected. The momentum transferred to the target, $\boldsymbol{\kappa}$, can then be defined as:

$$\boldsymbol{\kappa} = \boldsymbol{k}_0 - \boldsymbol{k}_a \tag{2.5}$$

The existence of three freely moving particles allows four types of cross sections to be defined: the integral cross section and the single, double and triple differential cross sections.

2.4 Defining Cross Sections

The results obtained from the measurement of collision events between two particles are reported as a cross section. For a particular collision, the cross section may be defined as the ratio of scattered particles per unit of time, per unit of target number density, per unit of incident flux. It represents a normalised measure of the time-independent probability for a particular type of collision under a given set of kinematical conditions.

The cross section which yields the least information with regards to both elastic and ionizing collisions is the integral cross section (ICS), often represented as $\sigma(E_0)$ [89]. An example of an ICS for elastic scattering is presented in figure 2.1. The ICS is a function solely of the incident electron energy E_0 and is a measure of the total number of scattering events for a specific collision process, which in the case of ionization is also the total ions produced, and is independent of the scattering solid angles Ω_a and Ω_b, or the outgoing electron energies E_a and E_b. The ICS can be obtained by integrating the single differential cross section with respect to all scattering angles or all energies [90]. The grand total cross section is the sum of the integral cross sections for all scattering processes, and represents the probability of any scattering event occurring. Figure 2.3 shows the relationship between each of the cross sections, with those towards the top containing more information about total scattering events, whereas those towards the bottom yield more information about individual processes.

2.4.1 Single Differential Cross Section

Differential cross sections yield more information than the ICS as they are dependent on the energies of the collision particles and/or the direction in which the particles are detected. The single differential cross section (SDCS) can be represented by:

$$\frac{d\sigma}{dE} \text{ or } \frac{d\sigma}{d\Omega} \tag{2.6}$$

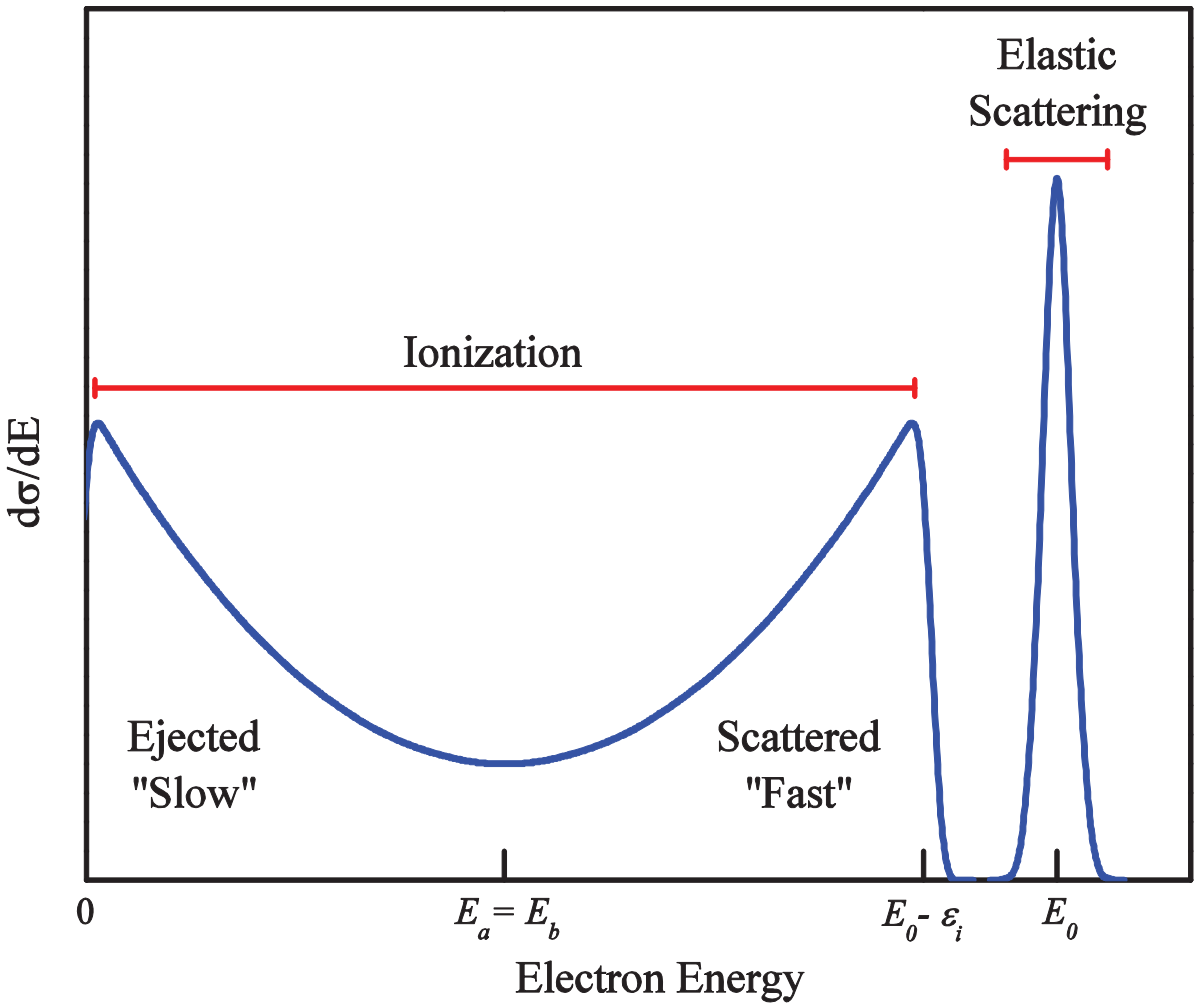

Figure 2.4: A diagrammatic representation of a typical single differential cross section. E_0, E_a and E_b are the energies of the incident, scattered and ejected electrons respectively, and ε_i is the binding energy of an orbital in the target particle.

which is differential either in the energy of one of the particles, or in the solid angle of one of the particles. For elastic single differential cross sections, which are cylindrically symmetric about the incident electron beam, this translates to the energy distribution of elastically scattered electrons to a specific in-plane angle θ (commonly known as an excitation function) or the angular profile of elastically scattered electrons of a specific energy (commonly known as an angular distribution). An example of an elastic angular distribution is given in figure 2.2. Elastic SDCSs can be measured using a crossed beam experiment beam, where a beam of energy selected electrons crosses a beam of target particles at 90°. The outgoing electron is then detected according to its energy or angle.

In ionization, the presence of two particles complicates matters as a SDCS that is differential in the angle of one of the particles for the full range of energies is of little physical importance [91]. A SDCS which is differential with respect to energy is a measure of the

energy distribution of the two outgoing electrons. Quantum mechanically the two outgoing electrons are indistinguishable, however under asymmetric kinematics the slower electron is normally referred to as the ejected electron and the faster electron is referred to as the scattered electron. The scattered electron has an electron energy close to the excess energy (E_0-ε_i), while the ejected electron has a energy close to zero. An illustration of a typical ionization SDCS is given in figure 2.4 as a function of electron energy.

It is clear that a minimum in the cross section occurs when E_a=E_b, which indicates that equal energy sharing between the scattered and ejected electrons is the least probable process. One cannot measure the energy differential SDCS for ionization directly. To obtain this cross section, the double differential cross section must be integrated with respect to all angles of emission of the outgoing electrons [92].

2.4.2 Double Differential Cross Section

The double differential cross section (DDCS) is represented by:

$$\frac{d^2\sigma}{d\Omega dE} \tag{2.7}$$

and is a measure of the energy and angular distribution of the scattered or ejected electron after an electron impact ionization event. The DDCS can be measured using the crossed beam method similar to the process for obtaining an elastic SDCS. An example of a DDCS for single ionization is presented in figure 2.5. At high and intermediate incident electron energies, the faster electron is preferentially emitted in the forward direction and are scattered in a narrow angular range about the unscattered incident beam of electrons. The slower electrons are ejected in all directions. Electrons that are ejected with comparatively higher energies produce some structure in the cross section due to a direct binary collision between the incident electron and an electron from the target species [92].

The primary issue with measurements of the DDCS is the large uncertainty with regard to which processes are being observed, and which orbital is ionized for a given excess energy. Theoretical models used to describe the DDCS must therefore include all possible processes and states that could contribute to the cross section. To overcome this problem, the energy and momentum of the scattered and ejected electrons must be determined so that the information obtained is specific to the ionization of a particular state. The (e, 2e) technique provides such information via measurement of the triple differential cross section (TDCS).

2.4.3 Triple Differential Cross Section

The triple differential cross section (TDCS) is represented by:

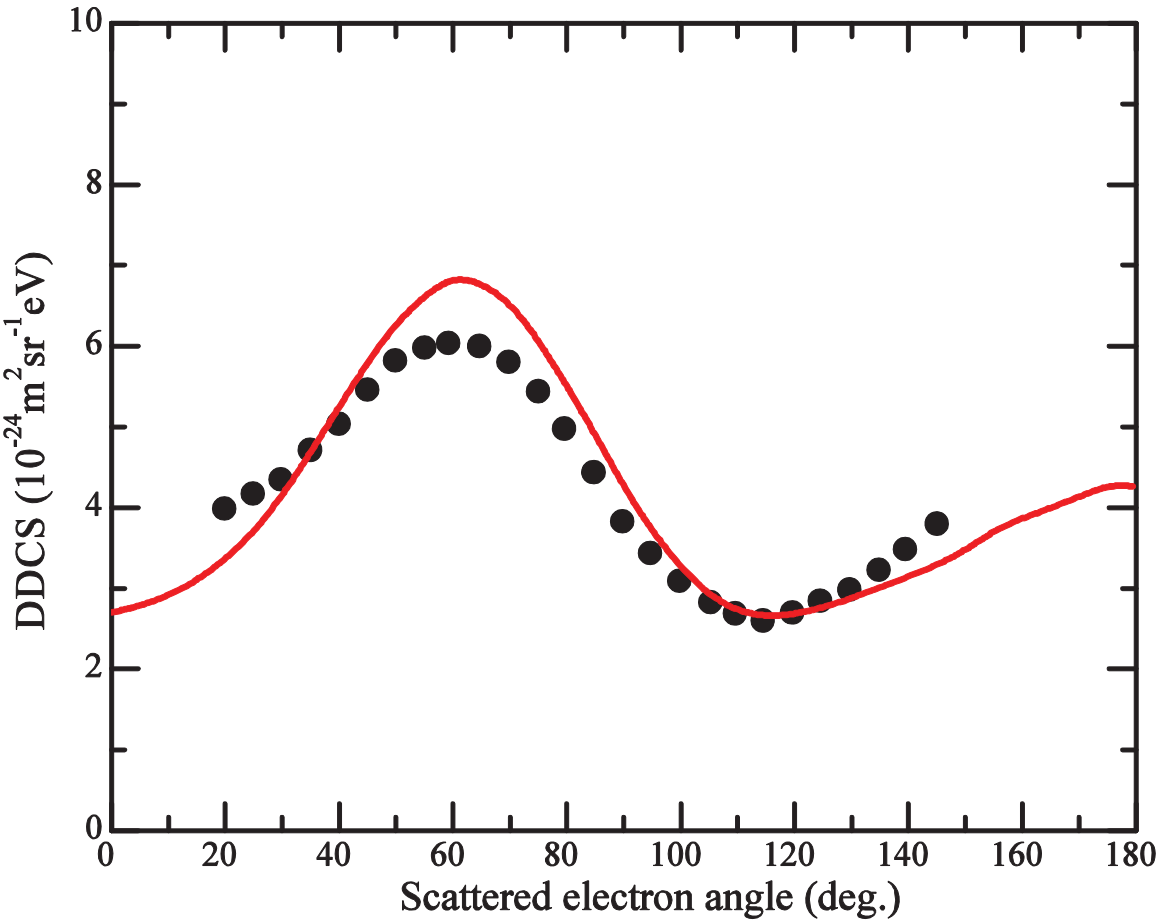

Figure 2.5: An example of an absolute double differential cross section for ionization of helium at an incident energy of 200 eV and an ejected energy of 20 eV. The experimental results (solid black circles) are compared to the CCC calculations (solid red line) as published in Röder *et al.* [93].

$$\frac{d^5\sigma}{d\Omega_a d\Omega_b dE} \tag{2.8}$$

and is a measure of the probability that after the ionization of a target particle by a projectile with specific energy E_0 and momentum $\boldsymbol{k}_0$, two electrons will be produced with discrete energies, E_a and E_b, and discrete momenta, $\boldsymbol{k}_a$ and $\boldsymbol{k}_b$, into the solid angles Ω_a and Ω_b. Ionizing collision experiments in which all the kinematics of the particles are determined assist in understanding the dynamics of the ionization mechanism, as well as the momentum distribution of the orbital from which the target electron was ionized [94].

The electron-electron (e, 2e) coincidence technique is used to determine all the kinematics (with the exception of spin) of the electrons via the measurement of the TDCS. The scattered and ejected electrons are detected in coincidence, allowing them to be correlated to the same ionization event. Since the ionization process is fully determined with respect to all kinematics of the scattered and ejected electrons, the theoretical models that

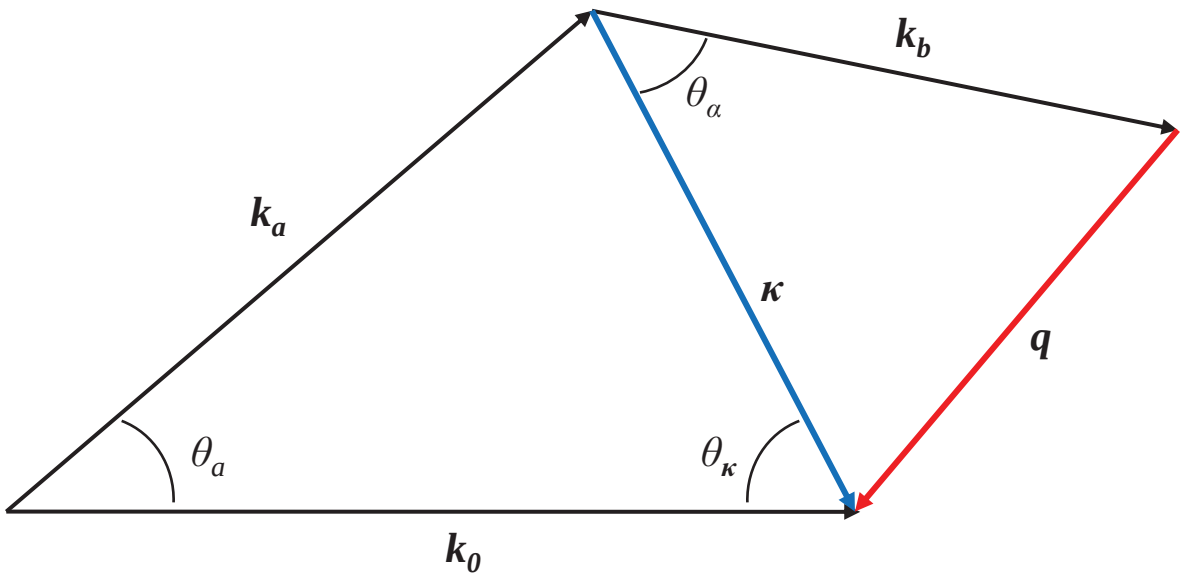

Figure 2.6: A vector diagram illustrating the transfer of momentum from the incident electron to the target. θ_a is the angle of the scattered electron relative to the incident electron, θ_κ is the angle at which the momentum is transferred and θ_α is the angle of the ejected electron relative to the momentum transfer direction.

describe the process are no longer convoluted by unobservable parameters, thus TDCS measurements are of considerable importance for the development of theoretical calculations.

When attempting to understand the ionizing collision process, the two key kinetic parameters are: the momentum imparted to the ion, $\boldsymbol{q}$, and the momentum transfer vector, $\boldsymbol{\kappa}$. The momentum imparted to the ion can be obtained through conservation of momentum (equation (2.4)) while the momentum transfer is defined as the momentum change between the initial and final state of the incident electron (equation (2.5)). Figure 2.6 is a vector diagram illustrating the transfer of momentum during an ionizing collision event.

The magnitude of the momentum transferred to the target ion during a collision process is important. Small to medium momentum transfer magnitudes (less than 1 a.u.) yield information relating to the structure of the target particle, whereas a medium to large momentum transfer magnitude (greater than 1 a.u.) yields information relating to the dynamics of the collision event [92]. Structural studies are useful in determining orbital ionization potentials, orbital momentum distributions and the target-ion correlations of the target particle. Structural cross section measurements also measure orbital specific momentum densities, which allow the determination of the electron momentum distribution around the target's nucleus [18]. When determining structural information, the ionization process is merely a probe and little information about the dynamics of the collision is obtained [92, 19]. TDCS measurements of dynamical collision events differ from structural

measurements by providing detailed information relating to the ionization processes, such as distortion effects and post-collisional interactions between the particles.

Given the large set of kinematic parameters (including E_0, E_a, E_b, Ω_a and Ω_b) that can be varied when obtaining a TDCS, one can utilise different kinematic variations of the TDCS to obtain information concerning different physical properties of the electron impact ionization process. There are five kinematic geometries normally employed to measure the TDCS: coplanar symmetric, non-coplanar symmetric (intermediate plane), non-coplanar symmetric, coplanar asymmetric and coplanar constant mutual angle. The three symmetric geometries are illustrated in figure 2.7 whilst the two asymmetric kinematic geometries, which includes constant mutual angle, are illustrated in figure 2.8.

For a kinematic geometry to be classified as symmetric, the energy and angle of the final state electrons are required to be equal (E_a=E_b, Ω_a=Ω_b). In contrast, asymmetric kinematic geometries depict an arrangement where the faster electron is detected at a fixed forward angle (generally less than 20°), while the slower electron angle detection angle is free to move within the scattering plane [95]. A coplanar kinematic geometry implies that the arrangement, coplanar mutual constant angle, is an in-plane asymmetric geometry which simply requires that the angle between the two final state electrons remains constant.

A requirement of symmetric kinematics is that there is an equal sharing of energy between the two final state electrons (E_a=E_b). As is evident from figure 2.4, equal energy sharing is the least probable process and thus under symmetric kinematics the cross section is difficult to measure. However, these kinematics do provide unique information about the incident, scattered and ejected electrons are all detected in a single plane, commonly referred to as the scattering plane. Non-coplanar geometries refer to kinematic arrangements in which one of the electrons is at an angle ϕ to the scattering plane. The information obtained by a non-coplanar TDCS measurement differs greatly from a coplanar measurement as the direction of the momentum transfer vector is out of the scattering plane. The final kinematic dynamics of the collision process. An example of a TDCS measured in the commonly used coplanar symmetric geometry is given in figure 2.9. As the energies of the two outgoing electrons are equal, almost half of the incident electron's momentum is transferred to the target ion. The amount of momentum transferred to the ejected electron is not constant since both Ω_a and Ω_b are varied through the scattering plane. Using figure 2.6, one can define the momentum transfer vector as:

$$\boldsymbol{\kappa}^2 = \boldsymbol{k}_0^2 + \boldsymbol{k}_a^2 - 2|\boldsymbol{k}_0||\boldsymbol{k}_a|\cos(\theta_a) \tag{2.9}$$

The structure seen in the TDCS for symmetric kinematics is caused by three main factors: the

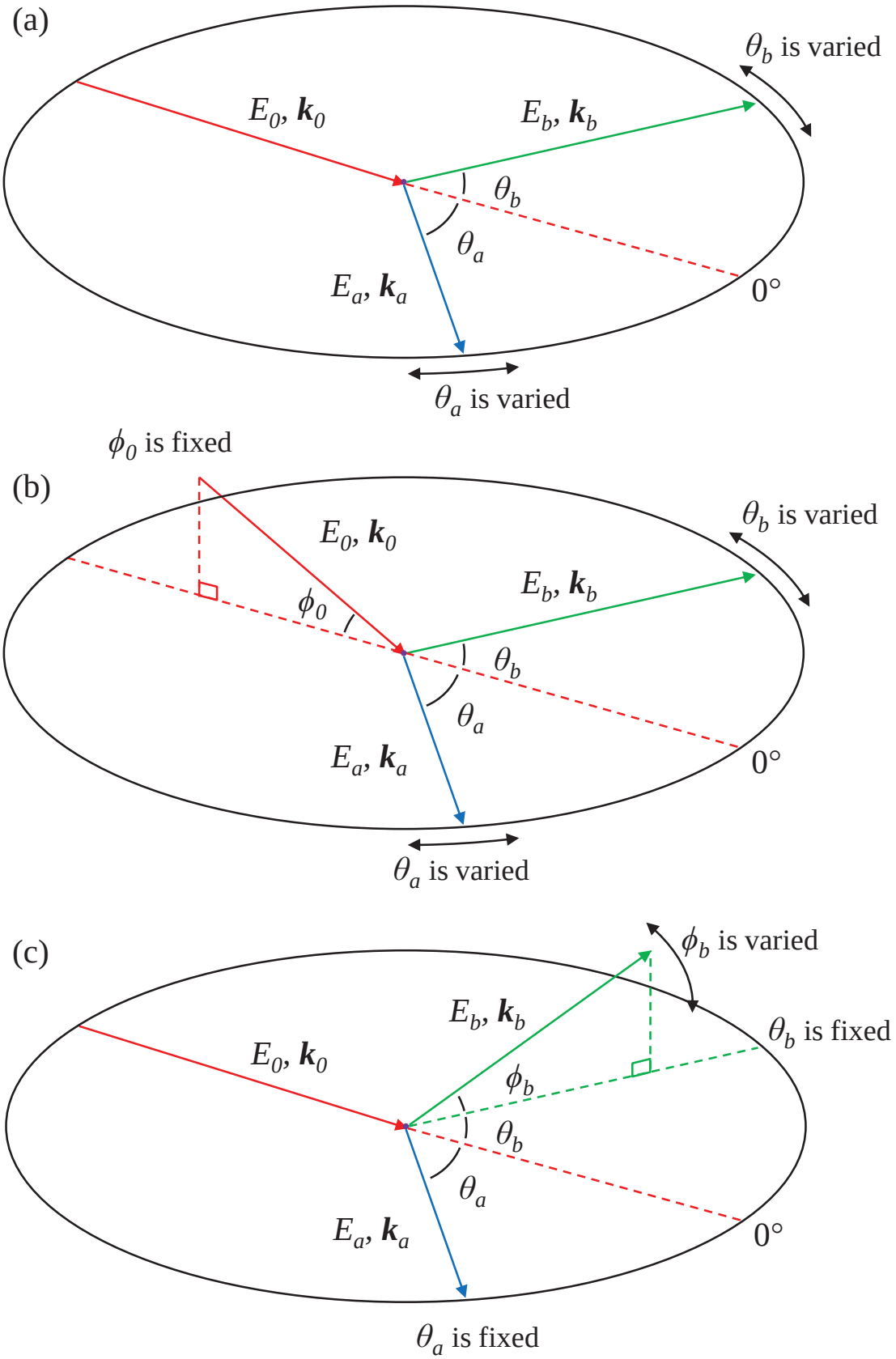

Figure 2.7: Symmetric kinematics, where E_a=E_b and θ_a=θ_b. Depending on which angles are fixed and which are variable it is possible to define the following geometries: (a) coplanar symmetric, (b) non-coplanar symmetric (intermediate plane) and (c) non-coplanar symmetric.

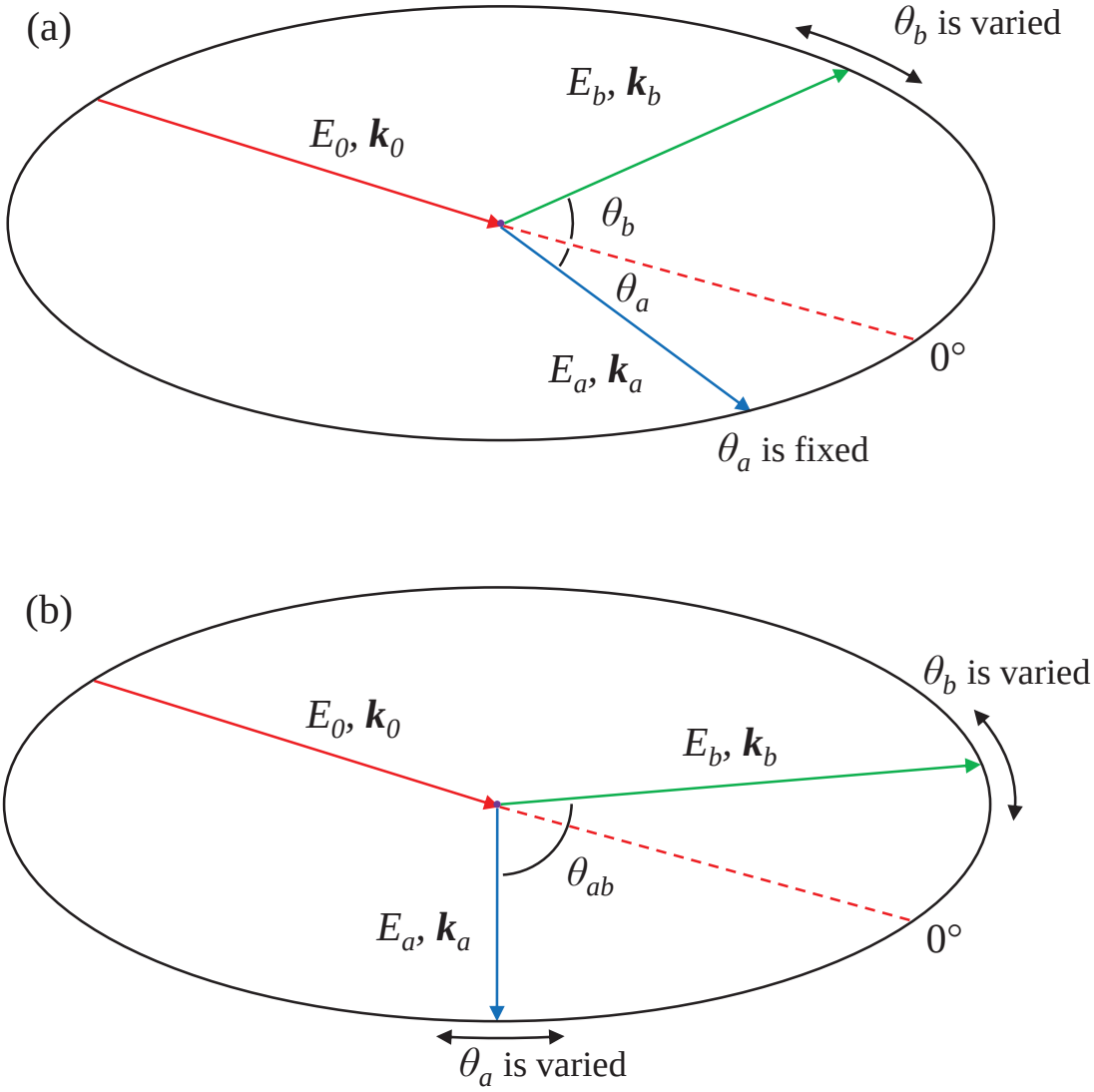

Figure 2.8: Asymmetric kinematics where at least either $E_a \neq E_b$ or $\theta_a \neq \theta_b$. Depending on which angles are fixed and which are variable it is possible to define the following geometries: (a) coplanar asymmetric and (b) mutual constant angle.

Coulomb density-of-state factors, binary collisions, and quantum interference between different contributions to the total transition amplitude [96].

High energy (e, 2e) experiments in the non-coplanar symmetric kinematic geometry are commonly known as Electron Momentum Spectroscopy (EMS) experiments and are conducted in an energy regime where the plane wave impulse approximation is valid and the recoil ion momentum is varied to obtain momentum profiles of each electronic state in the target. Figure 2.10 is an example of an EMS experiment, where varying the out-of-plane angle of the ejected electron is analogous to varying the recoil ion momentum.

Experiments in the intermediate plane geometry differ from the conventional non-coplanar symmetric geometry by varying the incident electron azimuthal angle as opposed to

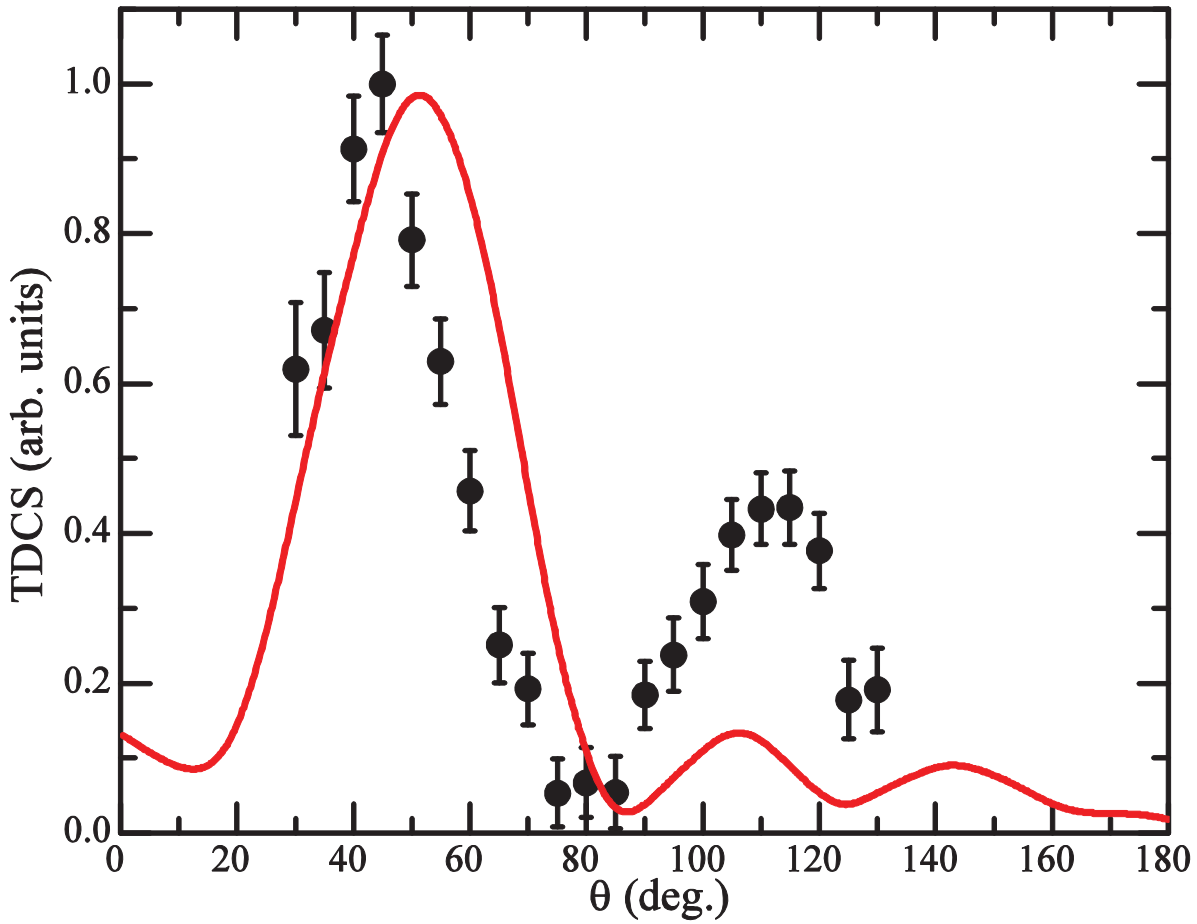

Figure 2.9: An example of a TDCS measured in the coplanar symmetric geometry, for the 3s orbital of argon. The experimental data was taken from Haynes and Lohmann [97] and the theoretical curve was calculated using the DWBA code of McCarthy [91].

the ejected electron out-of-plane angle [98]. Non-coplanar intermediate plane experiments are performed by fixing the detection plane and varying the azimuthal angle of the incident electron with respect to this, where ψ=0° corresponds to the coplanar geometry and ψ=90° corresponds to a geometry referred to as the perpendicular plane. Varying the azimuthal angle allows the evolution of the TDCS from the common plane to the perpendicular plane to be studied and vice versa. By measuring a wide range of scattered and ejected electron angles, stringent tests of theory can be provided [99]. For large azimuthal angles of the incident electron, the final state electrons will have undergone multiple scattering events, including from the target nucleus, and as such are generally quite small in magnitude and difficult to measure and accurately predict [100]. Figure 2.11 is an example of the TDCS for two intermediate plane angles.

Cross sections measured under asymmetric kinematics differ from symmetric TDCSs in that structural and dynamical information can be obtained simultaneously, depending on the energy and momenta of the interacting particles. The physical properties of the collision

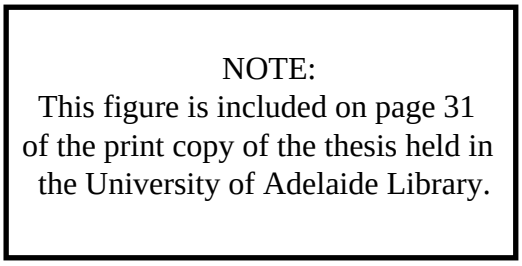

Figure 2.10: An example of a TDCS measured in the non-coplanar symmetric geometry, for the argon 3s orbital. The experimental and theoretical results were taken from McCarthy and Weigold [101].

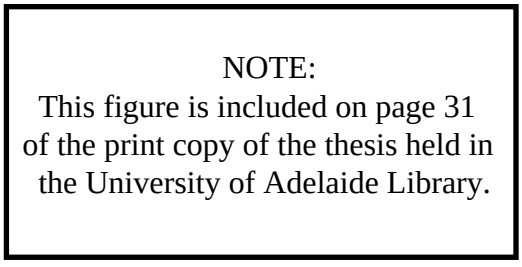

Figure 2.11: An example of a TDCS measured in the non-coplanar symmetric (intermediate plane) geometry, for the 1s orbital of helium. The experimental data was taken from Murray and Read [99].

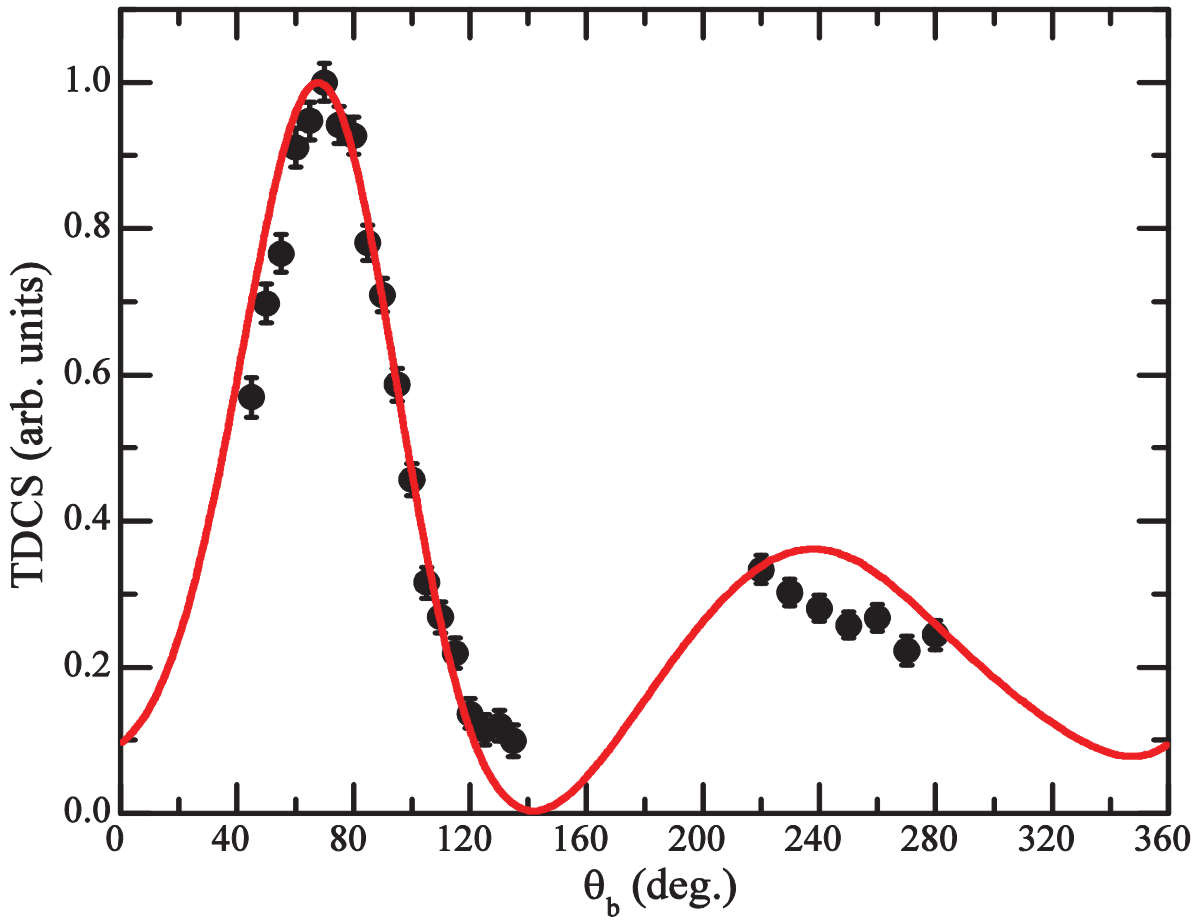

Figure 2.12: An example of a TDCS measured in the coplanar asymmetric geometry, for the 1s orbital of helium. The experimental data was taken from Milne-Brownlie *et al.* [25] and the theoretical curve was calculated using the DWBA code of McCarthy [91].

process are described by the characteristics of the forward and backward lobes in the TDCS, while the shape of the TDCS can be indicative of the orbital type the ionization occurred from (see figure 2.12 for an example). The forward lobe, referred to as the binary lobe or peak, is due to a binary collision that involves the clean knock out of a bound electron: the backward lobe, commonly known as the recoil lobe or peak, arises from the ejection of a bound electron due to a binary collision which undergoes a subsequent recoiling collision with the target nucleus.

At low and intermediate electron impact ionization energies (approximately 20 times the binding energy or less), the magnitude of the momentum transferred can be quite large [92]. In these interaction energy regimes, information relating to the dynamics of the collision process is obtained. At high incident energies (greater than 20 times the orbitals binding energy), the interaction between the target particle and the incident electron is negligible and the amount of momentum transferred is small. In this regime the incident electron can be treated as a photon, as the charge becomes irrelevant if the particles do not have a chance to

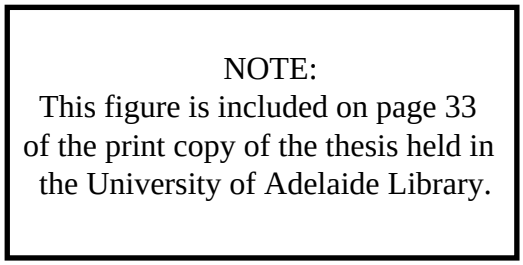

Figure 2.13: An example of the momentum probability distributions for s-type and p-type orbitals. Shown here are the distributions for the atomic 1s orbital of helium (solid red line) and the atomic 3p orbital of argon (dashed blue line), both measured at approximately 800 eV incident electron energy as published in Ugbabe *et al.* [102].

interact [92]. Measurements of the TDCS in asymmetric kinematics can yield information relating to the structure of the target particle, such as determining ionization potentials [103], akin to some of the measurements made in EMS experiments, as well as dynamic information. The shape of the TDCS for an asymmetric kinematic is determined by the structural or dynamical conditions of the collision process. An example of the TDCS for an electron ionized from an s-type orbital is given in figure 2.12. The ionization of an s-type electron produces a single peak in the binary region (between 0° and 180°) and a second peak in the recoil region (between 180° and 360°). An electron ionized from a p-type orbital would produce a double peak in the binary region and a second peak in the recoil region. The peak in the recoil region is usually only a single peak as it is insensitive to the shape of the orbital the electron was ionized from. The relative size of the recoil peak when compared to the binary peak gives an indication of the strength of the interaction between the electrons ionized from the specific state and the target nucleus, and is generally much smaller in magnitude

Figure 2.14: Example of a TDCS measured in coplanar constant mutual angle geometry, for hydrogen. The experimental data and the DWBA calculation were taken from Röder *et al.* [104].

compared to the binary peak, regardless of the orbital ionized. In the high energy case, the binary and recoil peaks are expected to be symmetrical about the momentum transfer direction. However, at lower incident energies post-collisional interaction PCI effects are present and are observable as shifts in the position of the binary and recoil lobes, which may no longer be symmetric. The shape of the TDCS in the binary region is determined by the momentum distribution of the bound electron before it is ejected. Orbitals that have s-type characteristics have a probability distribution which is at a maximum when the recoil ion momentum p tends to zero, whilst p-type orbitals tend to zero as the recoil ion momentum approaches zero [92]. For kinematic arrangements where the magnitude of the ejected electron momentum corresponds to the magnitude of the momentum transferred to the target, bound Bethe ridge kinematics are said to be satisfied, and the momentum transfer direction will correspond to zero recoil ion momentum [90]. The probability of finding an s-type or p-type electron for a range of electron recoil momenta is illustrated in figure 2.13.

The final kinematic arrangement that needs to be considered is the mutual constant angle geometry. In this asymmetric case there is equal energy sharing between the two

outgoing electrons (E_a=E_b) and the angle between the two outgoing electrons θ_{ab} remains constant. Figure 2.14 is an example of a TDCS measured in this geometry. Due to equal energy sharing, the physical properties measured in this geometry are similar to symmetric kinematic properties. This geometry has been proposed as an ideal arrangement for studying incident channel effects at low energies and distortion effects at relativistic energies [105-106]. When the angle θ_{ab} is chosen so that $\boldsymbol{k}_0 \bullet \boldsymbol{k}_b = 0$, the contributions of the single and triplet two electron states to the TDCS are enhanced. When this condition is satisfied the Coulomb density of state factors are not dependent on the angle of the outgoing electrons, and thus this geometry is used to highlight single and double collision effects [96].

Experimental Techniques and Apparatus

3.1 Overview

Experimental measurements of electron impact ionization, as well as the elastic differential cross section measurements, were undertaken using a conventional coincidence spectrometer, located at the University of Adelaide (Adelaide, Australia). The coincidence spectrometer has been described in detail previously [107-108], and as a consequence the following sections will briefly describe the design and operation of the apparatus as well as any upgrades made over the duration of this project.

3.2 Experimental Apparatus

Housed in an evacuated stainless steel chamber, the (e, 2e) spectrometer consists of an electron source that produces a monochromatic beam of electrons crossed perpendicularly with a collimated beam of molecules formed from a single capillary. The ionizing collision takes place in a well defined volume known as the interaction region, shielded from stray electric fields via a grounded Faraday cage, while the post-collision electrons are detected in the plane perpendicular to the molecular beam by two electrostatic hemispherical analysers. Both analysers are mounted on separate concentric and individually rotatable turntables and are configured to accept electrons of energy corresponding to either the scattered or ejected electron. Scattered electrons are detected using a channel electron multiplier (CEM) while ejected electrons are measured with either a CEM or a position sensitive detector (PSD), which utilises the linear energy dispersion of the hemispherical analysers to collect a range of energies simultaneously. Using fast timing electronics, a complete understanding of the ionization process is attained by correlating the ejected electron with the final state angle and energy of the incident electron, a process known more formally as the (e, 2e) coincidence

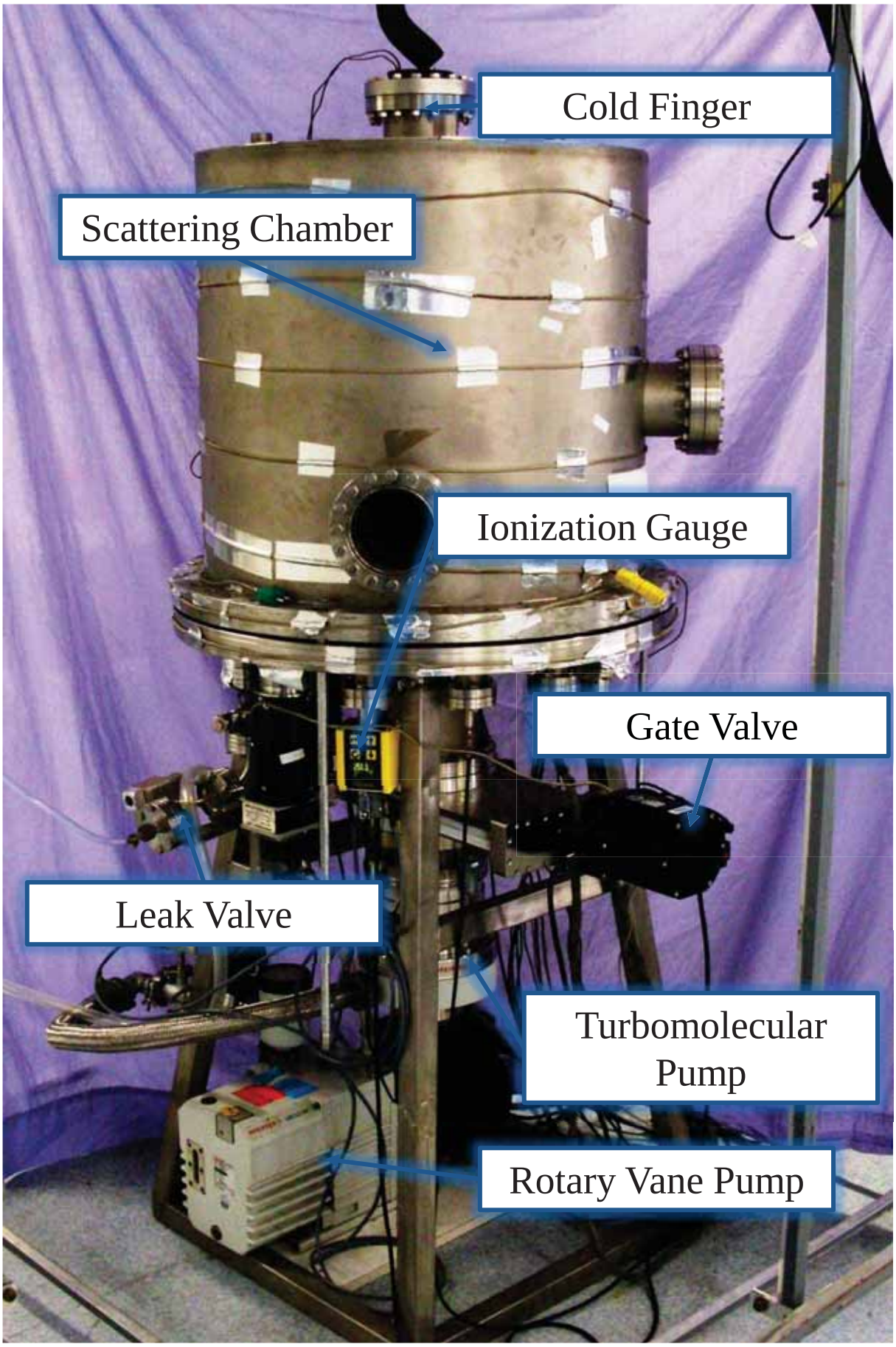

Figure 3.1: A photograph of the vacuum chamber and the associated operating gear that contains the (e, 2e) spectrometer.

technique. Photographs of the vacuum chamber and the electronics are shown in figures 3.1 and respectively. The following sections describe the vital components of the electron spectrometer in more detail.

3.2.1 The Vacuum Chamber

The baseplate of the vacuum chamber on which the coincidence spectrometer sits has a diameter of 704 mm and is 35 mm thick. A cylindrical lid protects the spectrometer internals, having a diameter of 614 mm and measured as 600 mm high. The chamber is sealed via a single Viton o-ring between the base plate and cylinder. The chamber was constructed using 310-stainless steel, a material chosen for its ideal non-magnetic properties. A 3 mm thick cylinder of μ-metal lines the inside of the vacuum chamber to reduce the penetration of external magnetic fields and a further reduction in external magnetic fields is facilitated by using three pairs of 2.2 m orthogonal Helmholtz coils. Only non-magnetic materials are used for the spectrometer internals.

The chamber also includes a 6 inch Conflat flange at its top, to which the liquid nitrogen cold finger is attached, and two 6 inch Conflat portholes spaced 90° apart on the side of the chamber for visual inspection of the spectrometer whilst under vacuum. Twelve 2.75 inch Conflat flanges are positioned in a ring on the inner edge of the chamber baseplate. These flanges contain the feedthroughs for the electronics that control and monitor the coincidence spectrometer. Positioned in the centre of the baseplate is an 8 inch Conflat flange that attaches to an externally housed Varian V550 turbomolecular pump, backed by a Pfeiffer DUO20M rotary vane pump. Separating the turbomolecular pump and the backing pump is an Edwards FL20k foreline trap whose sole purpose is to prevent the back flow of rotary vane pump oil. Mounted between the vacuum chamber and the turbo pump is an electropneumatic gate valve (MDC GV-6000), which is configured to automatically close when it is interlocked by the ionization gauge controller to isolate the vacuum. The interlock also shuts down the spectrometer electronics, and is triggered by an interruption to mains power that lasts longer than one second or if the pressure in the chamber rises above 8×10^{-5} Torr. Ideally, automatic closure of the gate valve will prevent the chamber pressure rising above 1×10^{-4} Torr for a minimum of two days.

The vacuum chamber can be pumped down to a base pressure of approximately 1×10^{-8} Torr, but normal operating pressure during experimental measurements is in the region of 2×10^{-5} Torr. The chamber pressure is monitored by an Instrutech Hornet ionization gauge, for pressures below 2×10^{-4} Torr, and an Instrutech Working Bee convectron gauge, for pressures

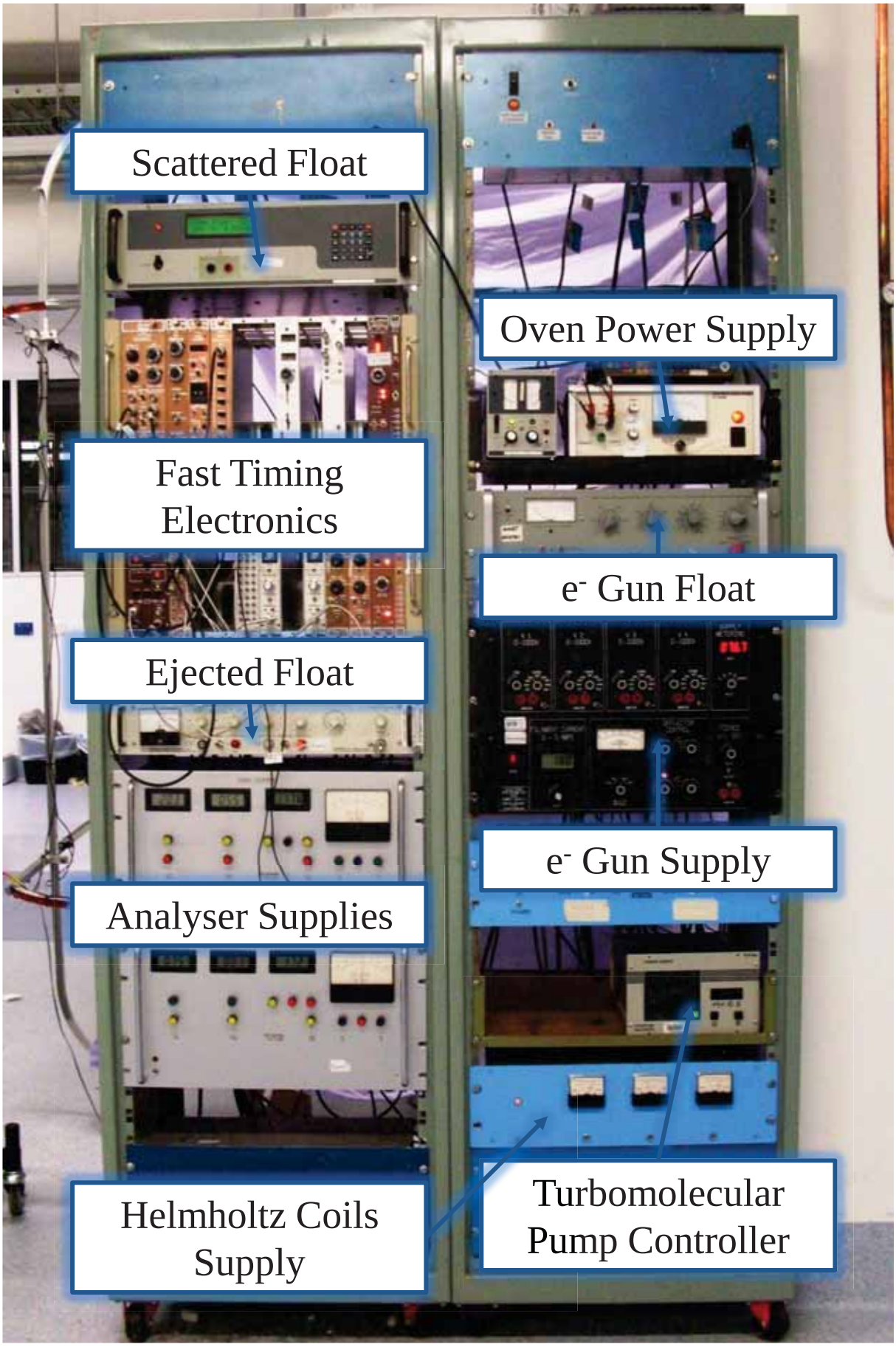

Figure 3.2: A photograph of the electronics racks which are used to control and monitor the coincidence spectrometer.

from atmosphere to 1×10^{-4} Torr. The gauge heads are mounted within a 2.75 inch Conflat flange beneath the chamber baseplate, especially important for the ionization gauge so that it is not directly visible within the chamber. This prevents stray electrons from the gauge filament reaching the interaction region without a significant reduction in conductance of gas to the gauge head. The backing pressure of the rotary vane pump is also monitored by an Instrutech Working Bee convectron gauge, mounted on the backing line directly after the rotary vane pump. Typical operating pressures for the rotary pump are of the order of 1×10^{-3} Torr.

Mounted on the baseplate of the chamber, elevated approximately 10 cm above, is a smaller plate of 440 mm diameter and 10 mm thickness. Sitting on the plate are two concentric, independently rotatable turntables. The lower turntable is allowed to rotate smoothly on the plate because of a v-shaped channel filled with 4 mm ceramic balls, spaced evenly by a stainless-steel ring. The upper and lower turntables are able to move independently of each other via the same method. Each turntable, through a rotary motion feedthrough, is connected to a stepper motor (Slo Syn M061 series). The stepper motors use a 9:1 gear box that allows for the precise computer control of the turntable motion. The scattered and ejected electron energy analysers are mounted on the lower and upper turntables respectively.

3.2.2 Molecular Beam Source

The target gas enters the interaction region orthogonally to the scattering plane via a single capillary, a 316-stainless steel hypodermic needle which is 20 mm in length and has an inner diameter of 0.69 mm. Under normal operation, the needle is mounted in a holder located at the chambers centre and connected to a feedthrough via Teflon tubing. An externally mounted T-piece connection, which has two 2.75 inch Conflat connections and a stainless-steel Swagelok fitting, connects the hypodermic needle to a Granville Phillips leak valve via the Conflat flanges. A 1000 mbar gas reservoir, positioned before the leak valve, provides constant driving pressure to the chamber. The gas reservoir usually contains ultra high purity helium or argon for calibration purposes, but can contain other gases such as nitrogen or krypton. On the third connection of the T-piece is a Nupro SS-8BK leak valve that is connected to a glass reservoir of liquid target. This reservoir supplies the target vapour to the chamber for substances that are liquid at room temperature, requiring that the gas lines and the capillary be heated to approximately 75°C and 130°C respectively to prevent condensation, and in the case of some molecules, dimer or trimer formation. In the event of system failure, a solenoid valve (Process Systems S55 2-way NC) is mounted between the

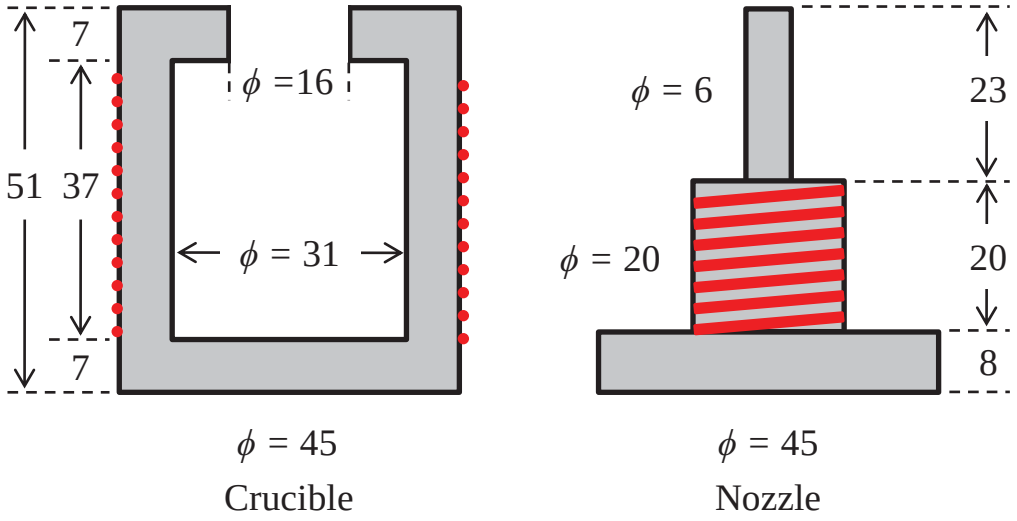

Figure 3.3: A 1:1 scale diagram of the molecular beam oven's crucible and nozzle. All dimensions are given in mm. The wrapping of the Thermocoax heating elements around the crucible and nozzle is displayed in red.

leak valve and the chamber to ensure the liquid target vapour, which in some cases can be quite reactive or corrosive, does not slowly fill the chamber when the system is not operational. The valve seat is made from PTFE so that the reactive samples do not adversely affect the vacuum seal.

The above arrangement works well for gases and liquids, but not for targets that are in the solid state at room temperature. Some solid targets, such as cytosine, require heating to temperatures in the order of 200°C to attain a workable vapour pressure. Given the difficulty in maintaining gas lines to temperatures of this magnitude, the alternative is to mount the target solid inside the vacuum chamber in a specially designed oven. With dimensions as shown in figure 3.3 and manufactured from non-magnetic 310-stainless steel, the crucible is capable of holding up to 27 cm^3 of sample. The oven is sealed from the chamber by an in-house manufactured Conflat style flange, with the only remaining opening being via a single capillary. The sample can be heated to the desired temperature which then effuses to the interaction region via the needle. It is important that the needle be heated to a temperature higher than the sample crucible to avoid clogging of the needle entrance. A needle has been specially designed with an inner diameter of 0.7 mm and length of 23 mm to ensure a high intensity, well-collimated molecular beam in the effusive flow regime [109]. Circular grooves have been machined into the exterior of the oven to accommodate the 1.5 mm diameter Thermocoax twin core heating elements. Comprising of two parallel conductors housed in a sheath of stainless steel, the main advantage of this heating method is the negligible magnetic field contributions as the field from each conductor is negated by the field of the other

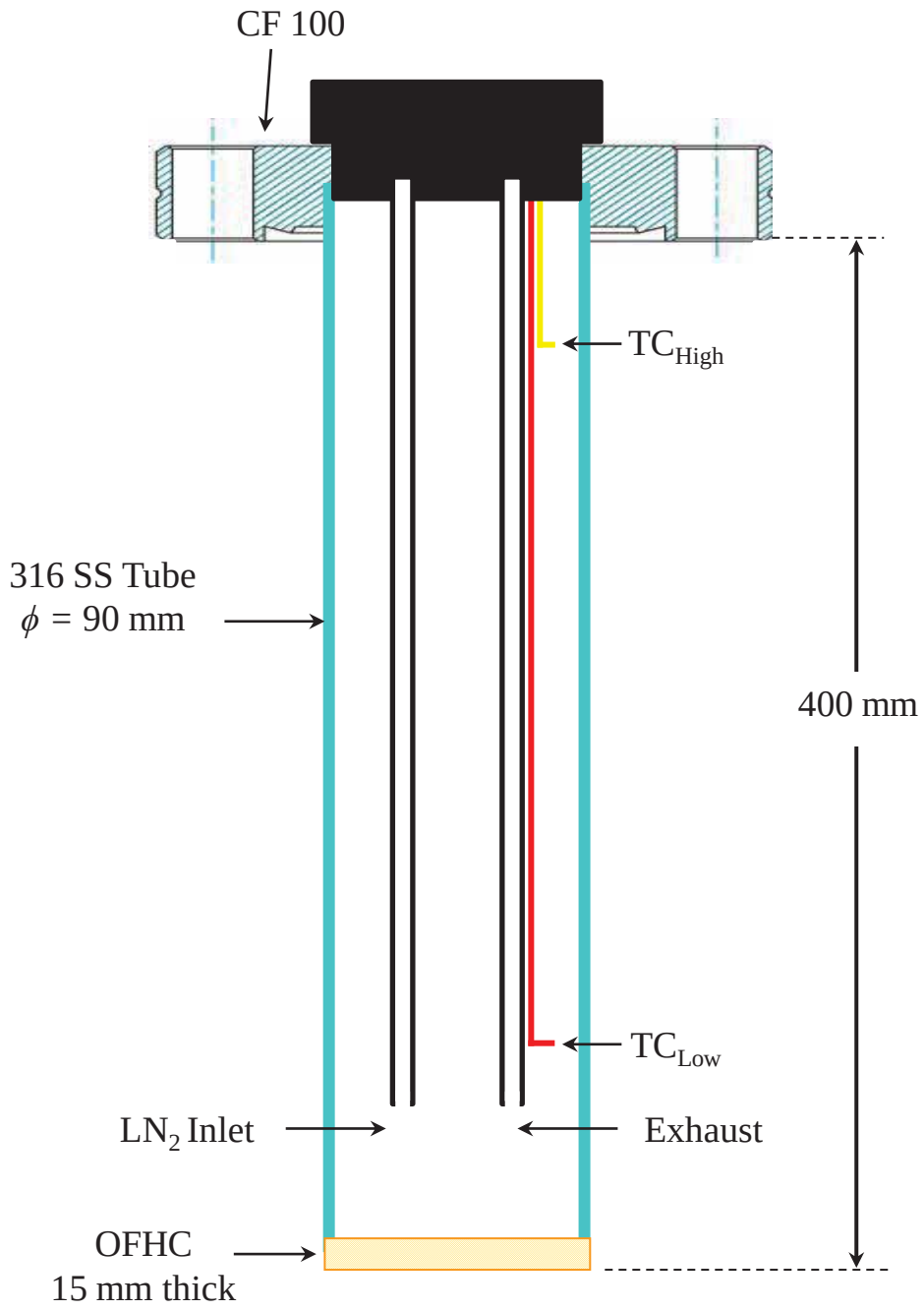

Figure 3.4: Schematic diagram of the cold finger with the vital components labelled. TC refers to the thermocouples, CF specifies a Conflat-type flange and the materials designated SS and OFHC refers to stainless steel and oxygen-free high conductivity copper respectively.

conductor. Power is supplied to the heating elements by a dual 40 V 2 A power supply, manufactured by the mechanical workshop at Griffith University (Nathan, Australia). The temperature of the oven and the needle can be measured and recorded separately via two independent K-type thermocouples, connected to a LabJack data acquisition card (LabJack U3-HV). Using the current setup, temperatures in excess of 300°C are achievable with a recorded temperature variation of less than 1°C.

In order to facilitate the location of the oven below the interaction region, the gas needle and associated holder have to be removed from the chambers centre. Since the use of calibration gases are essential for ensuring the correct operation of the coincidence spectrometer, an alternative mounting position is achieved in the scattering plane at approximately 90° to the incident electron beam. Check measurements with helium and argon have been performed at a variety of different energies and under several different operation modes, with no significant deviation from the expected results.

The trapping of target gases released from the oven, such as the DNA bases, is essential as these targets will readily return to the solid state via collisions with the apparatus and the vacuum chamber walls. Once solidified, it is difficult to remove these substances from the chamber via pumping alone. The coating of parts of the apparatus may also be detrimental to their operation. Indeed, even for measurements on certain reactive room-temperature liquid targets (namely THF) it is essential to protect the fragile components of the apparatus such as the electron gun filament and the CEMs from damage. As such, a cold finger has been installed in the chamber, concentrically mounted approximately 50 mm above the interaction region (see figure 3.4). Manufactured at the Universität Münster (Münster, Germany), from 316-stainless steel with an oxygen free, high thermal conductivity (OFHC) copper disk at the collection end, the cold finger is able to be filled externally with liquid nitrogen. Requiring approximately 2.5 L of liquid nitrogen to fill the cold finger (when it has already been cooled to liquid nitrogen temperatures), it is possible to achieve operation periods of approximately five hours before the cold finger needs to be refilled. Liquid nitrogen is provided by a Taylor Wharton LD25 dewar and is fed into the cold finger by the use of the liquid nitrogen vapour pressure. The dewar has a pressure relief valve that maintains the pressure inside the dewar to a maximum of 10 psi. A solenoid valve (ASCO Red-Hat NC) provides flow control of liquid nitrogen to the cold finger, automatically operated by computer control and the LabJack data acquisition card, and powered by a Kepco ATE 100-0.5M power supply.

3.2.3 The Electron Source

The electrons in this (e, 2e) spectrometer are provided by an electron gun. In general, an electron gun utilises a cathode, an electrostatic lens system, collimation apertures and deflectors to produce a well focused and reasonably monochromatic beam of electrons at a predetermined energy. Since a single experimental measurement can last in excess of a week, the electron source must produce a well focused, parallel beam of electrons which can maintain a constant intensity over a long period of time. Since the electron gun in this spectrometer has been described in great detail previously [108], this section shall provide a

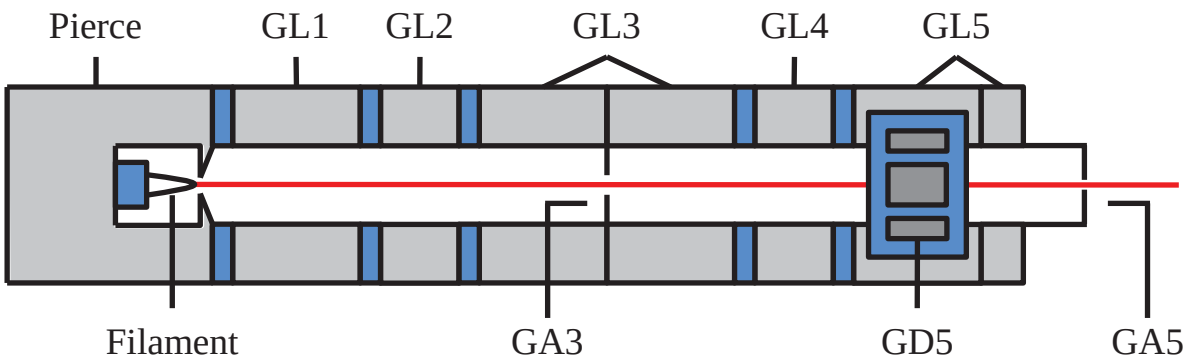

Figure 3.5: Schematic diagram of the electron gun, with the important components labelled. GL refers to gun lenses, GA refers to gun apertures and GD denotes gun deflectors. By convention the horizontal deflector pair is labelled the x-deflectors while the vertical deflector pair is referred to as the y-deflectors.

brief overview of the of the electron gun's components.

A schematic diagram of the electron gun is shown in figure 3.5. The source of the electrons is the cathode, which in this case is formed by a hairpin filament housed in a grid element. The filament is a needle nose tungsten wire mounted on a ceramic base, positioned in the centre of the grid element as close to the exit aperture as possible. The use of a hairpin filament reduces the emitting area of the filament wire to a well defined point, which emits electrons when a current above 1.5 A is applied. The electron energy is defined by the voltage at which the filament and the pierce element are floated, via a Power Designs model 3K40 high voltage power supply. The electron flux produced by the cathode can be increased by applying a negative potential to the Pierce element, since electrons repelled by the Pierce have a greater chance of exiting through the aperture.

The electron beam that leaves the cathode does so with a large angular spread. Electrostatic lenses are used to focus the diverging electrons and produce a parallel beam at the interaction region. Electrostatic lenses work by similar principles to optical systems, with the boundary defined by different electrostatic potentials. This electron gun uses a cylindrical lens system, consisting of five cylinders, each at a set potential. The gap between two cylinders of different potentials produces an electrostatic field which influences the motion of the electrons, allowing the electron beam to be controlled. A five element configuration operates as two three element systems, with one cylinder as a common element. Figure 3.6 presents an example of electron focusing using the spectrometer's lens system, generated using the charged-particle optics code SIMION [108]. The corresponding electron equivalent of Snell's law is [110]:

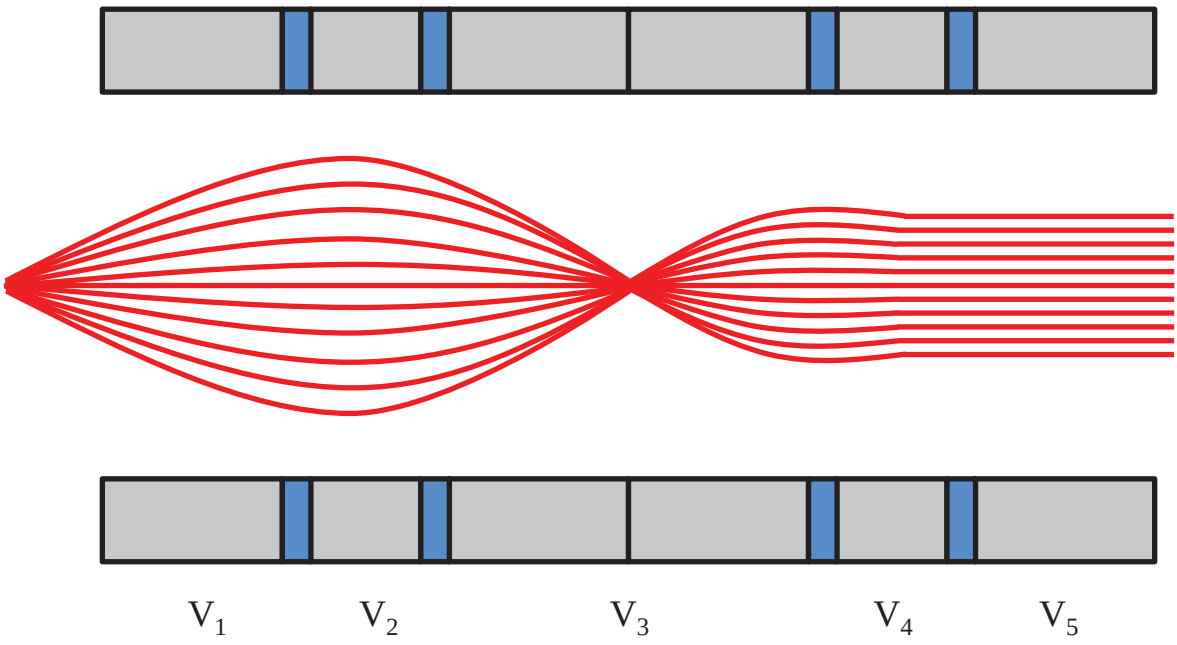

Figure 3.6: A cylindrical lens system where the first three lenses are used to focus the electron beam to a point and the second set of three lenses (where one lens is common to both sets) is used to produce a parallel electron beam. The example presented was generated using the charged-particle optics code SIMION [108].

$$\sqrt{V_1}\sin\alpha_1 = \sqrt{V_2}\sin\alpha_2 \qquad (3.1)$$

where α_1 and α_2 are the angles between the normal to the boundary and the path of the charge particle in the two regions of different electrostatic potential.

The first triple element system focuses the electron beam to a point at the centre of the common lens element, while the second system produces a parallel beam of electrons. The cylindrical lenses are floated to the electron beam energy except GL5 which is maintained at ground. The individual lens voltages are applied on top of this beam energy float voltage via a separate power supply unit, which was manufactured in house at the Griffith University mechanical workshop. The unit has four separate power supplies capable of up to 1000 V for the lenses, a lower voltage power supply capable of ±50 V with 10 mV precision to control the Pierce element, and four ±15 V supplies for four pairs of deflectors (in the event that an extra set were desired).

Good collimation of the electron beam results in a well defined interaction region yielding greater coincidence counts, and ultimately better statistics. Electrons with a large angular deviation are removed at three separate positions along the electron gun using 1 mm apertures, normally placed at the exit of the grid element, the focal point in the middle of GL3 (GA3) and at the exit of the electron gun (GA5). Electrostatic deflectors housed in the final

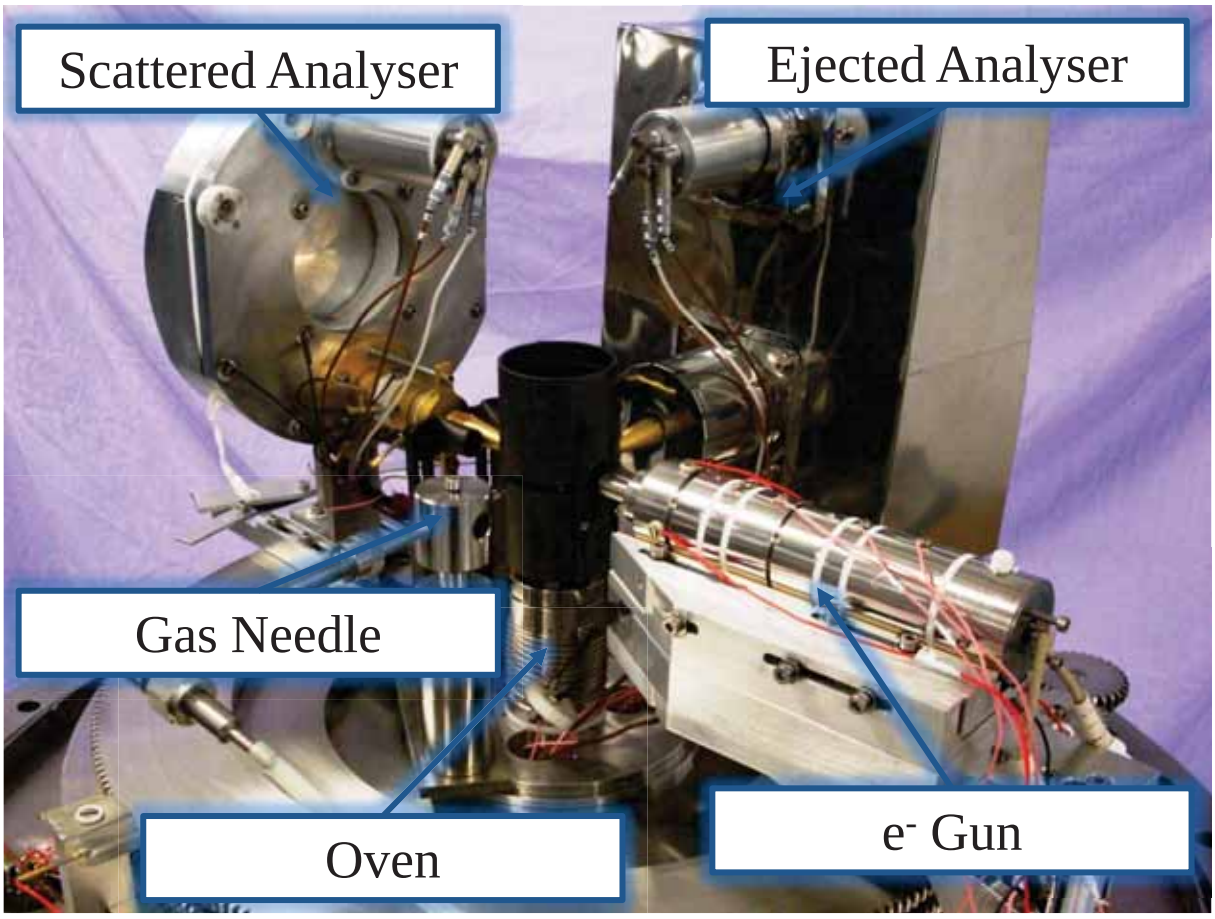

Figure 3.7 A photograph of the (e, 2e) spectrometers internals showing the two electrostatic hemispherical energy analysers mounted on separate turntables (scattered analysers shielding cover is removed), the electron gun (with shielding removed), the oven and the gas needle.

lens (GD5) are also used to the correct position of the electron beam in the plane perpendicular to the direction of travel. This ensures that the electron beam always passes through the centre of the interaction region. The electron source and optics were shielded from stray electric fields as well as charging effects by a non-magnetic metallic cover.

3.2.4 Analysers and Detectors

Mounted upon the turntables, in plane with the electron gun, are two hemispherical electrostatic energy analysers. A photograph of the internals of the (e, 2e) spectrometer is presented in figure 3.7. Both hemispherical analysers are independently rotatable within the scattering plane and have a geometric angular acceptance of approximately 1°. The role of the analysers is to separate out electrons of a specific energy. Each analyser operates in three sections: the input optics, the 180° electrostatic hemispherical analyser and the detector (see figure 3.8 for a schematic diagram of the energy analysers). The target electrons are accelerated or decelerated to the pass energy of the hemispherical analyser and focused to the

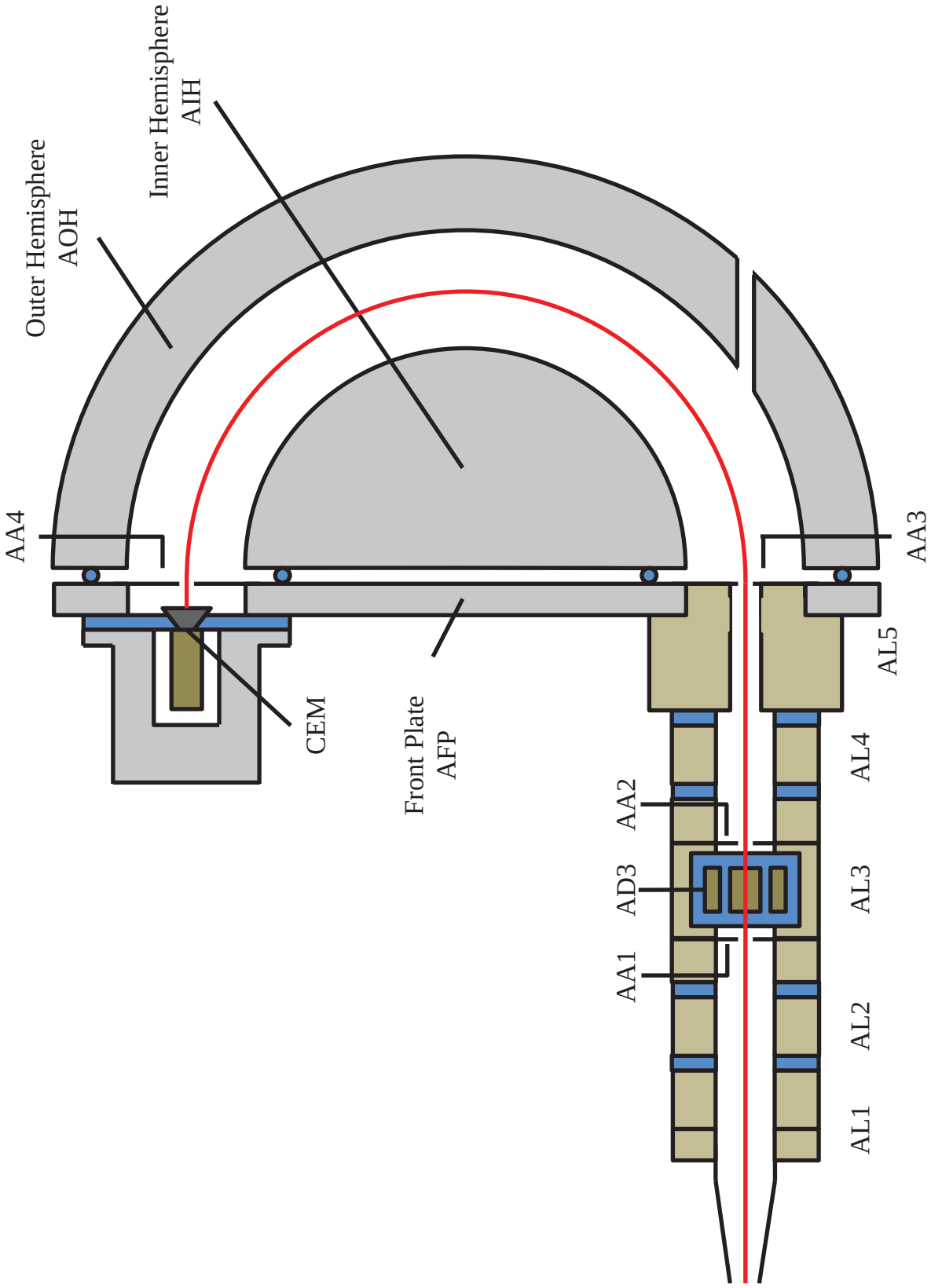

Figure 3.8: Schematic diagram of the hemispherical electrostatic energy analysers. AL refers to the analyser lenses, AA refers to the analyser apertures and AD refers to the analyser deflectors.

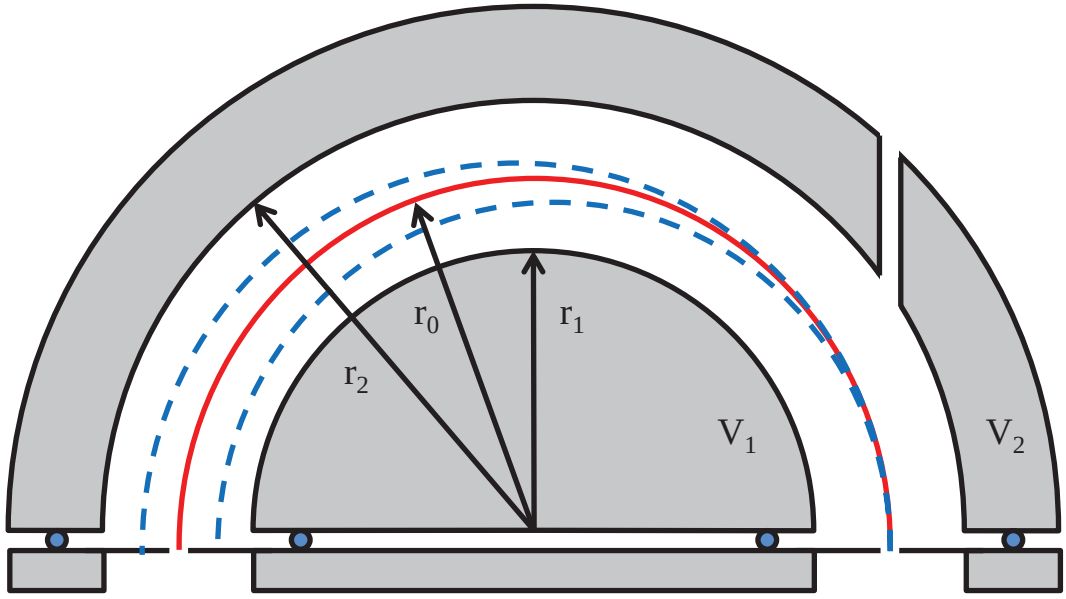

Figure 3.9: A schematic diagram of the trajectories of an electron through a hemispherical electron energy analyser. Electrons enter the hemisphere through the aperture on the right side and exit the hemisphere through the aperture on the left side. The solid red curve is the trajectory of an electron with an energy equal to the analyser's pass energy. The dashed blue curves are the trajectories of electrons that are not at the pass energy, the more energetic electrons are deflected by a smaller angle while less energetic electrons are deflected by a greater angle.

entrance of the hemisphere by the input optics. The input optics are a five element electrostatic lens system, similar to that used in the electron gun, constructed from oxygen-free high conductivity (OFHC) copper and plated with a 1 μm thick layer of gold to further improve conductivity and corrosion resistance. All lenses are floated at the pass energy of the analyser, with the exception of the first lens which is grounded with respect to the interaction region. Electrostatic deflectors (AD3), which are located in the common lens (AL3) and floated upon the lens voltage, are included to compensate for space and surface charging as well as minor misalignment of the input lenses. Two 1 mm apertures are placed either side of the deflectors to ensure a small angular resolution.

The hemispheres and the front plate are constructed from UHV compatible aluminium, with the internal surfaces of the inner and outer hemispheres coated with a 1 μm thick layer of gold to reduce patch fields and surface charging. The hemispheres are separated from the front plate using 4 mm diameter sapphire balls and 2 mm apertures are placed at the hemisphere entrance and exit. A 1 mm alignment hole is machined through the outer hemisphere in line with the central axis of the input optics to allow for easy alignment of the analyser with the interaction region without sacrificing the operation of the hemisphere. The

inner and outer hemispheres produce a central potential that deflects the electrons through a circular path, the radius of which is directly proportional to the electron energy. As a result, the analyser can select electrons of a specific energy, termed the pass energy, as they will follow a trajectory with the mean radius of the inner and outer hemispheres (see figure 3.9 for an example). Electrons of greater or lesser energy will be deflected by smaller or larger angles respectively. In this apparatus, the hemispheres have an inner radius of 50 mm, with an outer radius of 75 mm. The potential applied to the inner (V_1) and outer (V_2) hemispheres are given by the usual expressions:

$$V_1 = V_0[2\frac{r_0}{r_1} - 1] \tag{3.2}$$

$$V_2 = V_0[2\frac{r_0}{r_2} - 1] \tag{3.3}$$

In general, the energy resolution of a spherical analyser is given by [111]:

$$\frac{\Delta E}{E} = \frac{\omega}{r_0(1-\cos\phi) + l\sin\phi} \tag{3.4}$$

where ω is the width of the entrance and exit apertures and r_0 is the mean radius. Since ϕ is the spherical deflection of the analyser, which for a hemisphere equates to 180°, the above equation reduces to:

$$\Delta E = \frac{E\omega}{2r_0} \tag{3.5}$$

Consequently, varying the pass energy will determine the energy resolution of the analyser.

Upon exiting the hemisphere the electrons are detected by one of two different methods, the scattered electron is detected using a channel electron multiplier while the ejected electron can be detected either by a CEM or by using a position sensitive detector. The channel electron multiplier used for both the scattered and ejected analysers are Sjuts KBL5RS CEMs, positioned behind the 2 mm exit aperture of the hemispherical analyser. The CEM is isolated within an aluminium casing with Lemo connectors for the high voltage supply, grounding the front cone and for the extraction of the signal pulse. The CEM responds to the input of a single scattered electron by producing a negative signal pulse of microsecond width. When an electron strikes the CEM surface, secondary electrons are produced (1×10^8 gain) resulting in a cascade that produces a negative output pulse upon reaching the anode. Figure 3.10 presents a schematic of the Sjuts CEM showing the cascade of secondary electrons, as well as the electrical connections needed to extract the signal pulse. The specially designed shape of the Sjuts CEM increases the production of secondary electrons while reducing ion feedback. The CEM operates with the back plate at a high voltage between

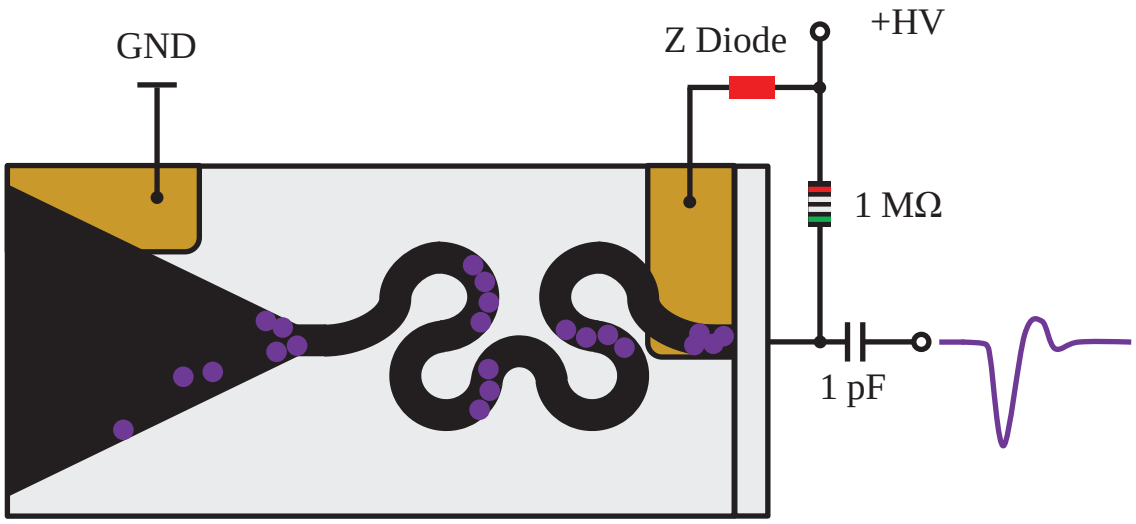

Figure 3.10: Cross section of a Sjuts channel electron multiplier, where a single incident electron produces a cascade of secondary electrons, eventually resulting in enough electrons to register a pulse collected in the anode. Also shown are the electrical connections of the pick off circuit which produce a CEM output pulse.

1.5 keV and 3.5 keV, depending on the age and efficiency of the unit.

The dispersion of the electrons at the exit of the hemispherical analyser is linearly related to the energy and as a result a position sensitive detector can be used to detect ejected electrons across an energy range of a few eV. This is advantageous for molecular measurements where there may be many molecular orbitals in a narrow energy range. However, given the expensive and delicate nature of PSDs and the destructive effects that some of the chosen molecular targets can have on the detection electronics, it was decided that a PSD would not be used to detect the ejected electron in this study and has instead been replaced by the more robust Sjuts CEM.

3.2.5 Fast Timing Electronics and Computer Control

The electrons detected by the scattered and ejected analysers can originate from a vast number of events which may not necessarily be from the same ionizing collision, such as other interaction processes as well as background scattering from interior surfaces of the vacuum chamber. The number of correlated scattering events can be small when compared to the number of uncorrelated events. The use of fast timing electronics allows for these events to be distinguished. An overview of how the CEM signals are processed is given in figure 3.11. The

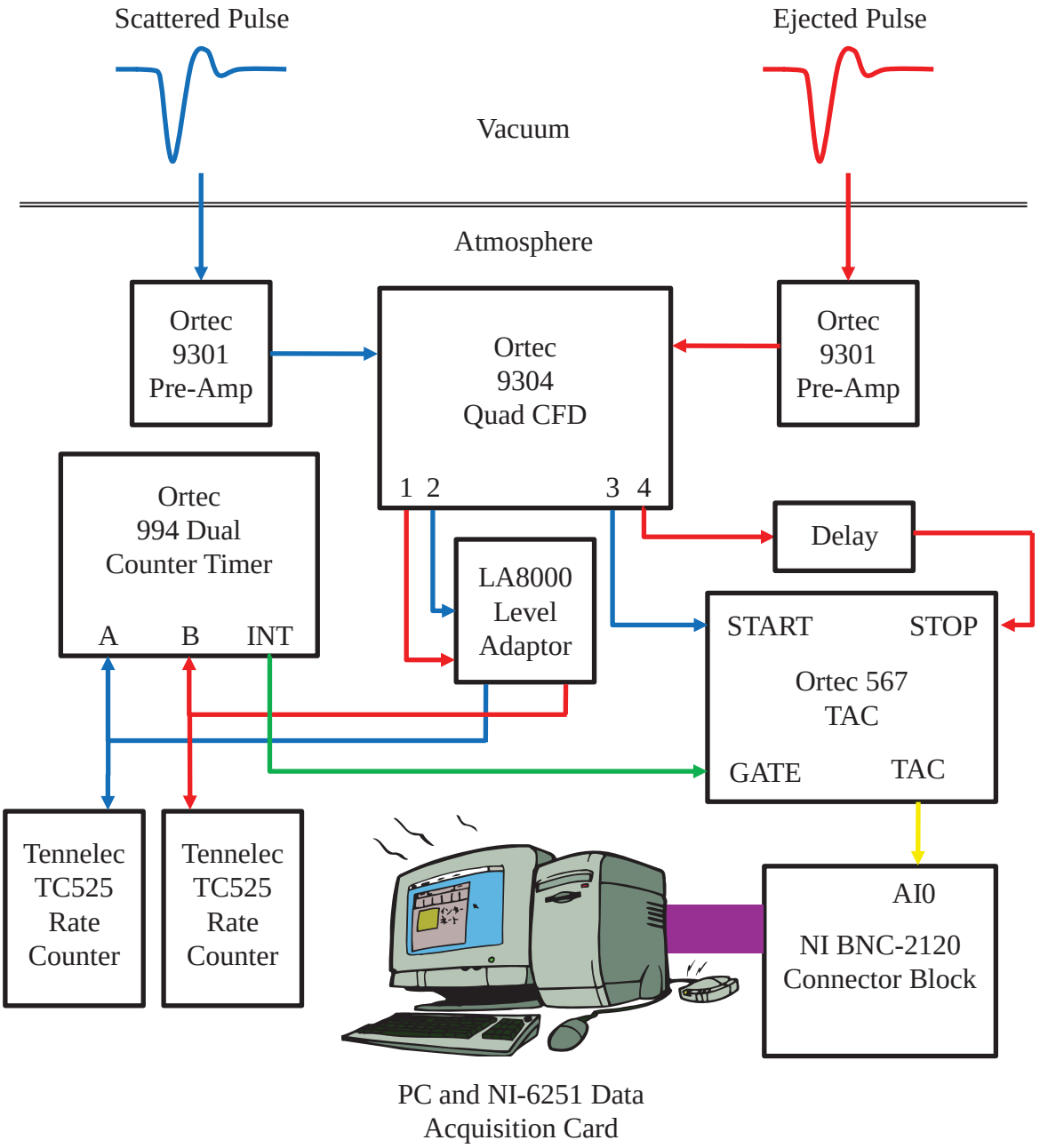

Figure 3.11: The fast timing electronics used to measure and correlate the CEM pulses into coincidence counts.

electrons detected by the scattered CEM produce a negative pulse signal at the anode which is collected directly after the anode through a 1 nF capacitor. Mounted directly outside the vacuum chamber is an Ortec 9301 pre-amplifier, which amplifies the magnitude of the CEM pulse by a factor of 10. Electrons detected by the ejected CEM produce a negative signal pulse and are collected and amplified in the same manner as the scattered signal. Each pulse is then sent to a constant fraction discriminator (CFD). The Ortec 934 Quad CFD is a nuclear instrumentation module (NIM) that contains four independent CFDs, two of which are

utilised to accept a negative input pulse from a pre-amplifier and generate two simultaneous fast negative logic pulses with constant rise times and amplitudes. At this time the remaining two CFDs are unused. A separate NIM known as a time-to-amplitude convertor (TAC) is used to measure the time interval between the arrival of the two pulses.

The scattered pulse is sent into the TAC (Ortec 567) as the start pulse while the ejected pulse is sent through a 63 ns delay (plus the difference in path length) then into the TAC as the stop pulse. The delay ensures that the stop pulse arrives well after the start pulse. Upon receiving both pulses the TAC generates an output pulse proportional to the measured time difference. This is processed using National Instruments LabView 8.5 installed on a Dell Inspiron 530 series computer; signals are measured by a high speed multifunction data acquisition card (National Instruments PCI-6251) which is coupled to the card via a shielded connector block (National Instruments BNC-2120). The fast logic pulses from both analysers also pass through a LA8000 level adaptor that converts the signals to a TTL pulse for use with the Tennelec rate meters and the Ortec 994 counter-timer. The rate meters monitor the instantaneous count rates in each of the channels and are used primarily to tune the experiment. The pulses sent to the counter timer serve to count the number of electrons detected in the scattered channel up to a desired preset level, as well as the number of ejected electrons collected for the corresponding scattered count preset. The counter timer is also used to gate the TAC, and as such TAC pulses are only sent to the data acquisition card when the counter timer is monitoring the scattered electron counts. This function allows the coincidence counts at each angle to be normalised for fluctuations in gas pressure and electron beam intensity, as well as normalisation between binary and recoil regions of the TDCSs.

Collection of an experimental TDCS requires lengthy data collection times. Typical data collection runs can last a week or more, consequently automated computer programmes are required to control and monitor the coincidence spectrometer. LabView 8.5 and the associated high speed data acquisition card connected to a shielded connector block are used to control the movement of both analysers, acquire and analyse the experimental data, as well as monitor apparatus specifics such as temperature and pressure.

3.3 Experimental Techniques

3.3.1 The Coincidence Technique

The electron-electron (e, 2e) coincidence technique is used to detect pairs of outgoing electrons after an ionization event, and it is essential that both electrons originate from a

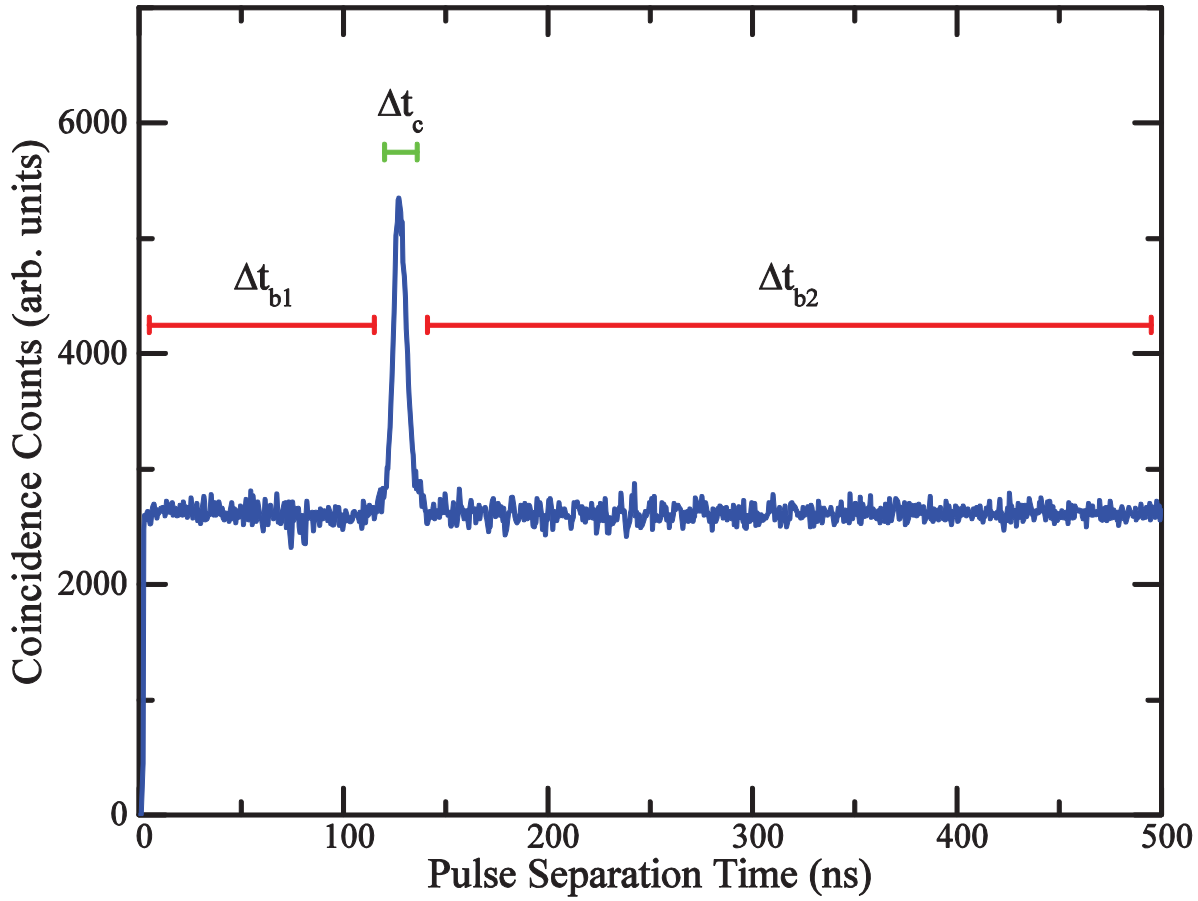

Figure 3.12: An example of a coincidence timing spectrum, in this case for helium. The coincidence window of width Δt_c=16 ns contains the coincidence peak. The number of random counts within the coincidence window are estimated by the number of random counts in the background windows, of widths Δt_{b1}=111 ns and Δt_{b2}=355 ns.

single ionization event. The use of timing correlation allows coincident pairs to be distinguished from random background counts.

As discussed previously (section 3.2.5), the TAC generates an analogue output pulse proportional to the measured time difference, which is sent through to the data acquisition card. The LabView software collects the data and displays a timing spectrum, which is simply the distribution of counts across a specified time window. Detected electrons that have originated from the same ionization event will always arrive with the same time difference, and thus produces a narrow coincidence peak in the timing spectrum. Random background counts should have a random time distribution and will eventually, in principle, form an even background signal. In the present experimental configuration, a typical timing spectrum has a timing window of 500 nanoseconds, and can be divided into three separate windows, as shown in figure 3.12. The coincidence window encompasses the coincidence peak, and the remaining two windows contain the uncorrelated electron pairs either side of the signal window. Depending on the energy difference between the scattered and ejected electrons, the

coincidence window may be quite close to the zero timing position. This is generally inconvenient so the timing position can be changed via an external delay to extend the arrival time of the slower electron.

The number of true coincidence counts N_t is the total counts in the coincidence window N_c of width Δt_c minus the random counts N_r. The exact number of random counts within the coincidence window is unable to be determined directly but is instead inferred from the average number of counts in one or more background windows of total width Δt_b. Thus the number of true coincidence counts is:

$$r = \frac{\Delta t_c}{\Delta t_b} \tag{3.6}$$

$$N_t = N_c - N_b \mathrm{r} \tag{3.7}$$

The standard deviation of the number of true coincidence counts is given by [103]:

$$\sigma_t = \sqrt{N_c + N_b r^2} \tag{3.8}$$

$$\sigma_t = \sqrt{N_t + \frac{N_b(r+1)}{r^2}} \tag{3.9}$$

and it can be seen that improvements in the spread of true coincident counts can be made by ensuring that the width of the signal window is as small as possible and that the width of the background window is as large as possible.

To determine the limitations and advantages of the coincidence technique one may define the true coincidence counts and statistical uncertainty in terms of the experimental parameters and the relevant cross section. One can begin with an expression for the true coincidence count rate R_t, which is dependent on the TDCS for electron impact ionization σ_5, the incident electron current I, the target density n, as well as the angular and energy resolution of the individual analysers, $\Delta E_a \Delta E_b \Delta\Omega_a \Delta\Omega_b$. R_t is therefore given by:

$$R_t = nI\sigma_5 \Delta E_a \Delta E_b \Delta\Omega_a \Delta\Omega_b \tag{3.10}$$

The number of random coincidence counts R_r within the signal window is given by the product of the random count rates into each detector and the window width.

$$R_r = R_a R_b \Delta t_c \tag{3.11}$$

The count rates in each detector are defined as:

$$R_a = nI \frac{\sigma_{2a}}{dE_a d\Omega_a} \Delta E_a \Delta\Omega_a \tag{3.12}$$

$$R_b = nI\frac{\sigma_{2_b}}{dE_b d\Omega_b}\Delta E_b \Delta\Omega_b \tag{3.13}$$

where σ_2 is the double differential cross section of either analyser *a* or *b*. By combining these two equations it becomes evident that the random coincidence counts can be reduced by minimising the number of background counts into each analyser. There have been attempts to achieve this via a variety of methods including the use of high conductivity materials like gold plated OFHC copper, shielding the entrance to the analyser with a molybdenum sheath and positioning the analyser entrance as close as possible to the interaction region. This is especially important for the ejected analyser which generally operates at very low energies and commonly has a large percentage of background counts. It is also noted that random coincidence counts can be reduced via improvements to the timing resolution.

Variations in flight times introduce an unavoidable dispersion in the arrival times of correlated electrons, whose finite width arises from three different sources [18]. Most obvious is the finite size of the interaction region, where different locations of collision events within the region result in slight variations in path length and thus arrival time. By the same logic, a timing variation is present for electrons of varying kinetic energies arising from collision events at the same location. The third source of dispersion occurs as a result of the electronics. The discriminator NIM unit which triggers when the input pulse exceeds a set threshold value can have small time differences in triggering due to variations in pulse amplitude.

The quality of the experimental statistics can be quantified by two parameters: the signal-to-background ratio (SBR) and the relative error [103]. The SBR is simply a ratio of the true coincidence counts and the random coincidence counts. Using the previously defined equations this becomes:

$$\frac{R_t}{R_r} = \frac{nI\sigma_5 \Delta E_a \Delta E_b \Delta\Omega_a \Delta\Omega_b}{R_a R_b \Delta t_c} \tag{3.14}$$

$$\frac{R_t}{R_r} = \frac{nI\sigma_5 \Delta E_a \Delta E_b \Delta\Omega_a \Delta\Omega_b \delta(E_0 - E_a - E_b - \varepsilon_i)}{(nI)^2 \frac{\sigma_{2_a}}{dE_a d\Omega_a}\frac{\sigma_{2_b}}{dE_b d\Omega_b}\Delta E_a \Delta\Omega_a \Delta E_b \Delta\Omega_b \Delta t_c} \tag{3.15}$$

Since the numerator in the SBR is a convolution of $\Delta E_a \Delta E_b \delta(E_0\text{-}E_a\text{-}E_b\text{-}\varepsilon_i)$ and the denominator is only $\Delta E_a \Delta E_b$ then the above equation can be simplified to:

$$\frac{R_t}{R_r} = \frac{\sigma_5}{nI\sigma_{2_a}\sigma_{2_b}\Delta t_c} \times \frac{\Delta E_s}{\Delta E_l} \tag{3.16}$$

where ΔE_s is the smaller value of ΔE_a and ΔE_b , while ΔE_l is the larger of the two values. As a result, improvements can be made to the SBR simply by reducing nI or Δt_c, or by setting

$\Delta E_a=\Delta E_b$. Of these options, reducing nI is the easiest way to increase the SBR, however this will adversely affect the relative error by reducing the number of true coincidence counts.

If experimental data is collected for a time t then the true counts as a function of the experimental parameters becomes:

$$N_t = R_t T \tag{3.17}$$

$$N_t = nI\sigma_5 \Delta E_a \Delta E_b \Delta\Omega_a \Delta\Omega_b \delta(E_0 - E_a - E_b - \varepsilon_i)T \tag{3.18}$$

$$N_t = nI A_t T \tag{3.19}$$

where the equation has been simplified by setting $A_t=\sigma_5 \Delta E_a \Delta E_b \Delta\Omega_a \Delta\Omega_b \delta(E_0-E_a-E_b-\varepsilon_i)$. The number of random counts in the background window, in terms of experimental parameters is given by:

$$N_b = rR_r T \tag{3.20}$$

$$N_b = rR_a R_b \Delta t_b T \tag{3.21}$$

$$N_b = r(nI)^2 \sigma_{2_a} \sigma_{2_b} \Delta E_a \Delta E_b \Delta\Omega_a \Delta\Omega_b \Delta t_b T \tag{3.22}$$

$$N_b = r(nI)^2 A_b \Delta t_b T \tag{3.23}$$

where the equation has been simplified by setting $A_b=\sigma_{2_a}\sigma_{2_b}\Delta E_a \Delta E_b \Delta\Omega_a \Delta\Omega_b$. The relative error in terms of experimental parameters is given by:

$$\frac{\sigma_t}{N_t} = \pm \frac{\sqrt{N_t + \frac{N_b(r+1)}{r^2}}}{nI A_t T} \tag{3.24}$$

$$\frac{\sigma_t}{N_t} = \pm \frac{1}{A_t}\frac{1}{\sqrt{t}}\sqrt{\frac{A_t}{nI} + \frac{A_b \Delta t_c (r+1)}{r}} \tag{3.25}$$

Substituting the terms A_t and A_b back into equation (3.20), the relative error becomes:

$$\frac{\sigma_t}{N_t} = \pm \frac{1}{\sqrt{\Delta\Omega_a \Delta\Omega_b}}\frac{1}{\Delta E_s}\frac{1}{\sqrt{T}}\sqrt{\frac{1}{nI\sigma_5} + \frac{(\sigma_2)_a(\sigma_2)_b}{(\sigma_5)^2}\frac{\Delta E_a \Delta E_b}{(\Delta E_s)^2}\frac{(r+1)}{r}\Delta t_c} \tag{3.26}$$

Then letting $\Delta E_a=\Delta E_b=\Delta E$, the above equation reduces further to:

$$\frac{\sigma_t}{N_t} = \pm \frac{1}{\sqrt{\Delta\Omega_a \Delta\Omega_b}}\frac{1}{\Delta E}\frac{1}{\sqrt{T}}\sqrt{\frac{1}{nI\sigma_5} + \frac{(\sigma_2)_a(\sigma_2)_b}{(\sigma_5)}\frac{(r+1)}{r}\Delta t_c} \tag{3.27}$$

It can be seen from equation (3.27) that improvements to the relative error can be

made by increasing T, nI, $\Delta\Omega_a\Delta\Omega_b$ and ΔE. However, doubling the experimental counting time T will only achieve a reduction in the relative error by a factor of 1.4. If nI is increased the relative error can only tend to a constant value, however the SBR will decrease linearly. Therefore, relative error is dependent on $\Delta\Omega_a$, $\Delta\Omega_b$ and ΔE, indicating that improvements to the relative error can be made via the angular and energy resolution of the spectrometer, or most simply by increasing the counting time.

3.3.2 Coincidence Energy Resolution

The overall coincidence energy resolution of the (e, 2e) spectrometer, (ΔE_c), comes from the combined energy resolution of the electron gun and both electron energy analysers. If one assumes that the energy width of all electrons to have a Gaussian profile, then the overall coincidence energy resolution can be expressed as [95]:

$$\Delta E_c^2 = \Delta E_0^2 + \sqrt{\frac{1}{\Delta E_a^2} + \frac{1}{\Delta E_b^2}} \tag{3.28}$$

Experimentally, one can obtain an indication of the energy resolution through a binding energy spectrum. The energy resolution of the binding energy spectrum is given by:

$$\Delta E_{BE}^2 = \Delta E_0^2 + \Delta E_a^2 + \Delta E_b^2 \tag{3.29}$$

However, the binding energy spectrum is only an indication of the coincidence energy resolution. It has been shown both theoretically [112] and experimentally [113], that the effective coincidence energy resolution is not the same as the resolution obtained from a binding energy spectrum. While it is not possible to experimentally obtain ΔE_c, since scanning any of the energies E_0, E_a or E_b will produce a binding energy spectrum, it is an important quantity for calculating cross sections from count rates or deconvolving data [113]. ΔE_{BE} is also a quantity of importance, as it represents the ability of the experiment to resolve close lying states.

3.3.3 Alignment of Spectrometer

The interaction region is considered be an infinitely well resolved point in space. In reality the interaction region is finite due to the overlap of the target gas beam, the incident electron beam and the viewing volume of the scattered and ejected analysers, normally referred to as the scattering volume (see figure 3.13 for an illustration of this). If the size of the effective overlap was to change as the analysers rotated through the scattering plane, space volume effects would cause the number of true coincidence counts detected to be inaccurate. To

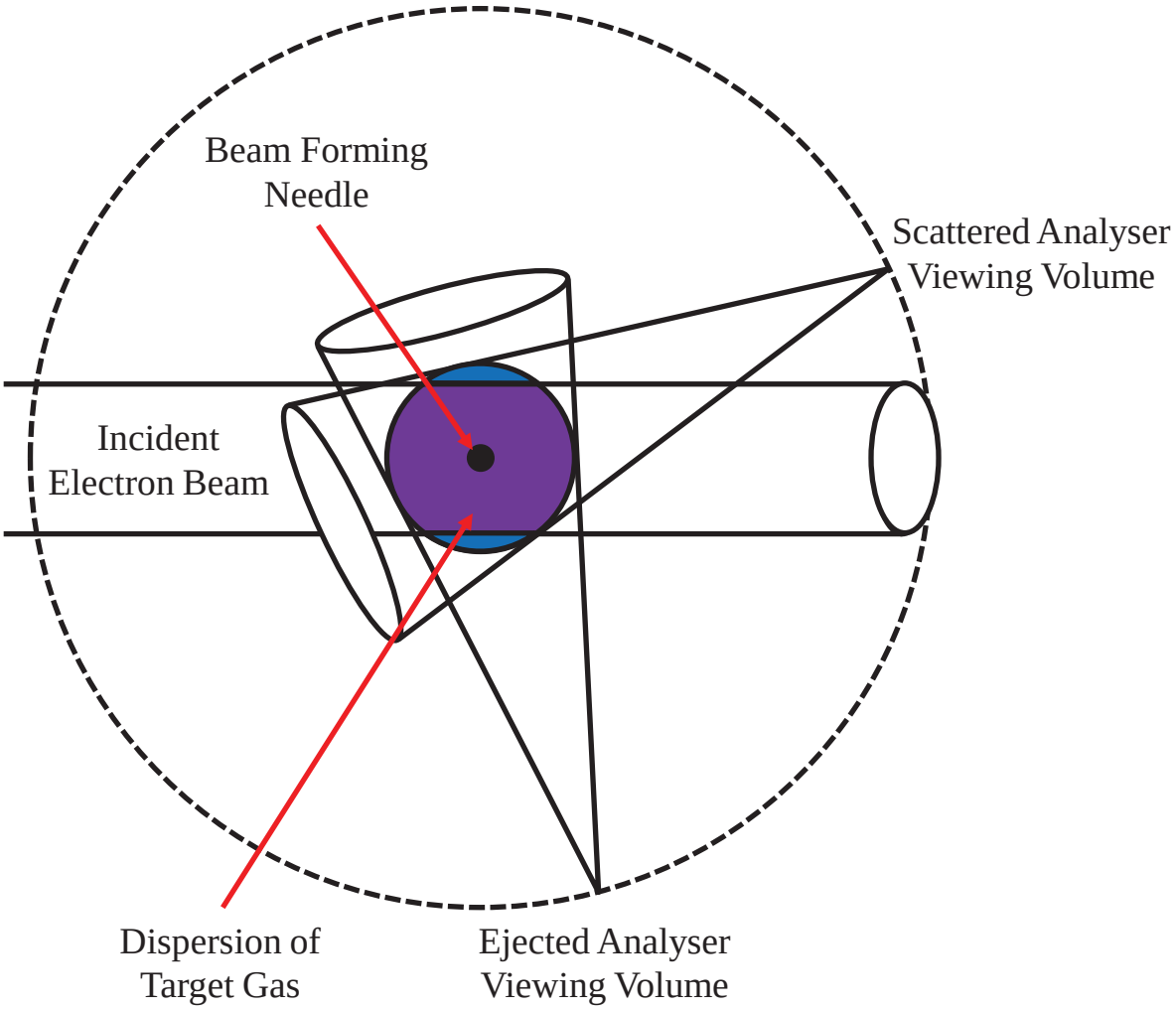

Figure 3.13: A schematic diagram of the scattering volume viewed from above. The dispersion of the target gas by the time it reaches the plane of the spectrometer is shown by the shaded blue circle. The purple portion of this circle represents the scattering volume: the overlap of the molecular beam, the incident electron beam and the viewing volume of the two analysers.

eliminate these effects, it is important the scattering volume remain a constant size so that the coincidence count rate is dependent only on the physical properties of the collision process. The accurate alignment of the spectrometer will ensure that distortion of the TDCS due to space charge volume effects are minimised.

In the present experimental setup, the interaction region is defined as the centre point of the small plate which supports the spectrometer. The beam forming needle which supplies the target gas, or the nozzle of the molecular beam oven, is positioned at this point and the height of the interaction region is set to be 3 mm above the gas source. The remaining elements of the spectrometer are then aligned with respect to this point. A visible reference point is made by marking a glass capillary tube. This fits firmly over the beam forming needle ensuring the correct height for the interaction region. Visual alignment is achieved by using a

surveyor's telescope to focus through the many apertures of the electrostatic lens systems to the reference point at the interaction region.

The electron gun is aligned to the visible reference by focusing through three, 1 mm apertures at the grid element, lens three and the gun exit. This also verifies that the lens elements are correctly aligned as misalignment manifests itself as the circular apertures appearing to be elliptical. The electron gun is mounted to the spectrometer support plate to allow the vertical height to be adjusted (particularly important for incorporating the molecular beam oven) with the capability for small horizontal adjustments to be made to account for any misalignment.

For each analyser to be aligned, a 1 mm aperture collinear to the central axis of the input optics has been drilled through the outer hemisphere. This alignment hole has a negligible effect on the performance of the analyser [114]. Alignment is then achieved by focusing through this aperture, the 2 mm aperture at the hemisphere entrance and the two 1 mm apertures positioned either side of the deflectors housed in the middle lens. The design of the analyser mounts also allow for vertical and horizontal adjustments to compensate for misalignment. The alignment of each analyser is performed at several angles in the scattering plane to eliminate any space volume effects.

3.4 Experimental Calibration

It is important to perform experimental calibrations of the spectrometer to ensure reliable operation. An energy calibration of the incident electron beam and of the hemispherical electron analysers is needed to ensure the proper energy assignment of the process. Angular calibrations of the electron analysers are also required to correctly assign momentum transfer and the range of the angular distribution. It is possible to perform further checks to ensure correct operation of the (e, 2e) spectrometer including the measurement of a series of well-known cross sections.

3.4.1 Energy Calibration

Because the (e, 2e) technique is dependent on the conservation of energy (equation 2.3), an accurate knowledge of the incident electron energy and the detection energies of both outgoing electrons is necessary. By determining the energy offsets accurately, the number of coincidence counts can be maximised. Calibration of the electron energies is important as the experimental apparatus can suffer from an energy offset due to patch fields and contact potentials.

The energy offset of the scattered electron analyser has been determined using the

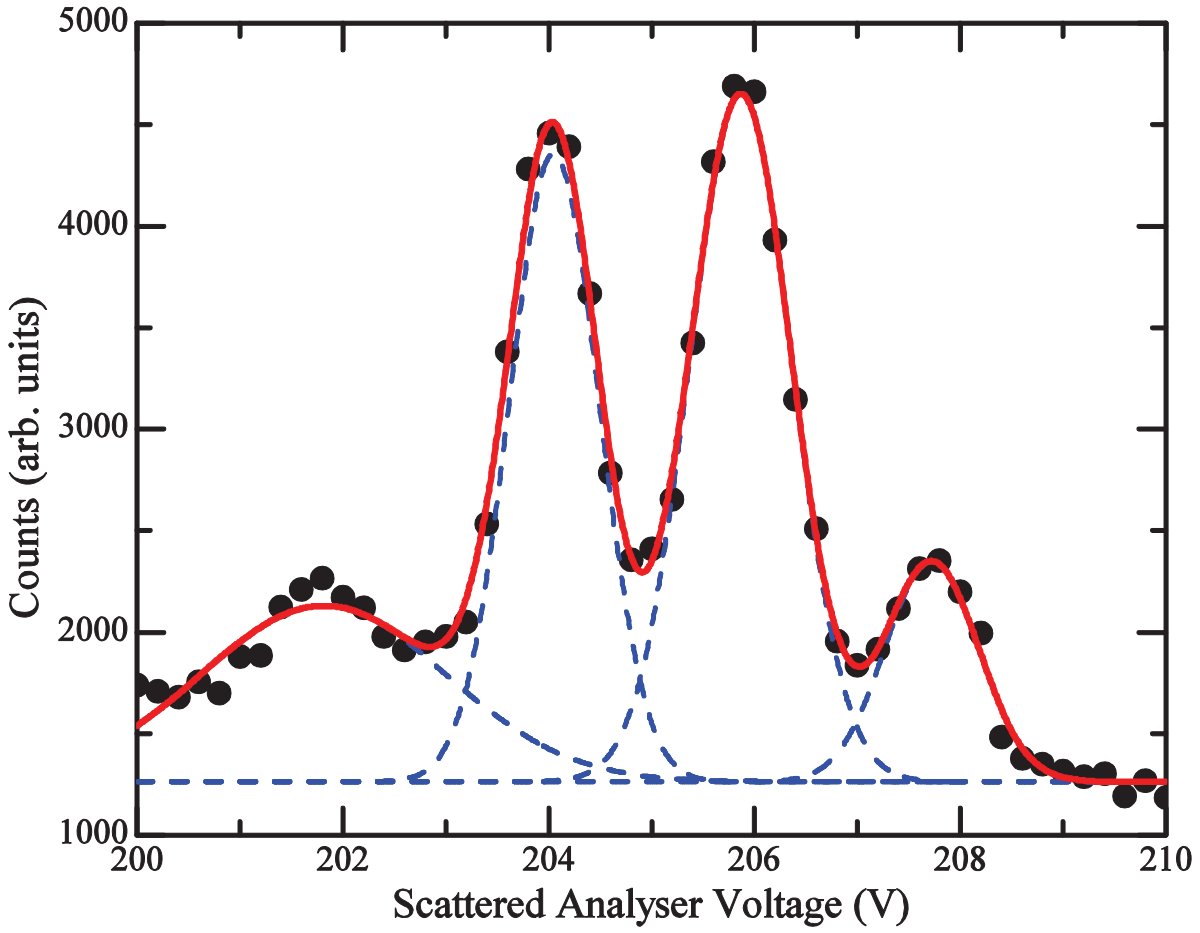

Figure 3.14: The primary argon Auger lines as measured using the scattered electron analyser, fitted with a sum of Gaussian peaks. By calculating the energy difference between the scattered float voltage and the known energy values of the lines [115], an energy offset can be determined for the scattered analyser.

Assignment	Line	Energy (eV)
$L_3M_{2,3}M_{2,3}$	$^1S_0$	201.09
	$^1D_2$	203.47
	$^3P_{0,1,2}$	205.21
$L_2M_{2,3}M_{2,3}$	$^1S_0$	203.23
	$^1D_2$	205.62
	$^3P_{0,1,2}$	207.23

Table 3.1: Assignment and corresponding energies of the main Auger lines of Argon, in the energy range 200-208 eV, as published by Werme *et al.* [115].

Auger process of argon. The Auger process is the most appropriate method for determining the energy offset of the analyser, as it is independent of the energy of the incident electron and the Auger decay spectrum is unique for each atom. The argon Auger process is initiated by ionizing an electron from the inner 2p shell using an incident electron energy of approximately 600 eV. The ionized atom will then decay to a lower energy state by Auger emission. For argon the principal Auger lines are the $L_{2,3}$-$M_{2,3}M_{2,3}$ lines whose energies lie between 200 eV to 208 eV [115]. The energy of each line is given in table 3.1.

The energy offset of the scattered electron analyser was determined using the main Auger lines of argon (see figure 3.14). The scattered analyser energy is scanned over the expected region of the lines. Due to the combined energy resolution of the electron gun and the scattered analyser, not all lines are able to be resolved. From the position of the peaks the energy offset of the analyser can be calculated. This method can also be applied to the ejected electron analyser, however simpler methods are available once the energy offset of one element is determined and the scattered electron analyser is generally chosen as it normally operates in this energy range.

The energy offset of the incident electron can be determined simply once the energy offset of the scattered electron has been established. Utilising the elastic differential cross section, the scattered electron is set to a fixed energy while the incident electron energy is scanned across the expected energy range until the count rate of the scattered electrons achieves a maximum. This same process may also be applied to simply determine the energy offset of the ejected analyser once the incident electron energy has been established.

It is also possible to utilise the coincidence technique to precisely determine the incident electron energy, and thus maximise the coincidence counts during data collection. With the energy offset of both analysers known, a binding energy spectrum is measured on a target with a very well known orbital energy, most commonly the helium 1s whose binding energy is 24.6 eV. The offset of the incident electron energy is then known via conservation of energy. Figure 3.15 is an example of a helium binding energy spectrum where the energy offset has already been accounted for. It is also worth noting that the binding energy resolution ΔE_{BE} is calculated from this binding energy spectrum as 1.5 eV full width at half maximum (FWHM).

3.4.2 Angular Calibration

It is important to ensure that there is no mechanical angular offset in the measured experimental cross sections as the angular shift of the features within a TDCS, when compared to theory or the momentum transfer direction, can be indicative of one or more

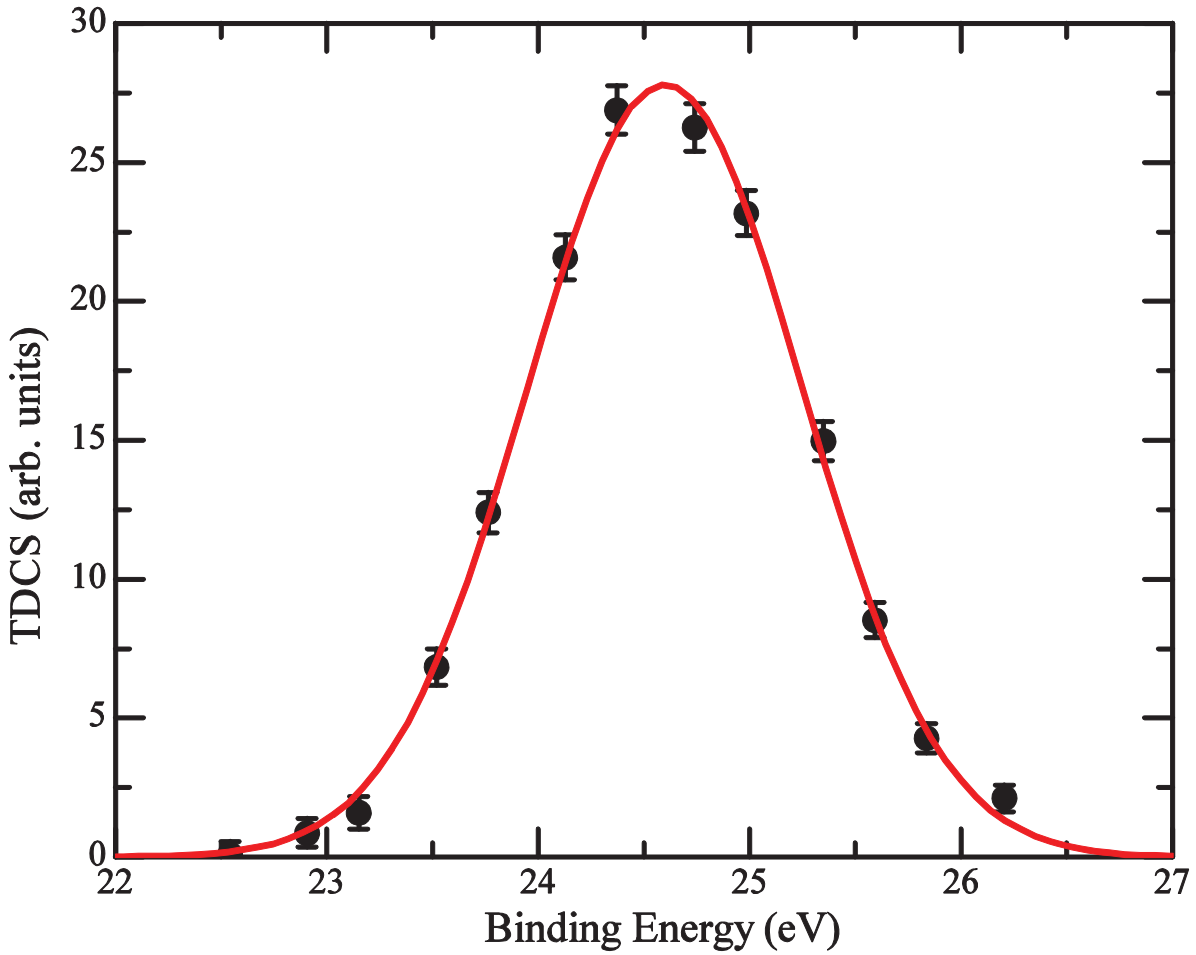

Figure 3.15: An example of a measured binding energy spectrum of the helium 1s orbital. The width of this peak is useful in defining the binding energy resolution ΔE_{BE} of the (e, 2e) spectrometer, which in this case is 1.5 eV FWHM.

physical effects present during the collision process that distort the measured cross section. Knowledge of these physical effects are important for a complete understanding of the collision process, and inaccurately reporting the TDCSs can make it difficult to correctly validate theoretical cross sections. The angular calibration is performed using known physical processes, rather than relying on mechanical methods. Since performing the same experimental cross section measurements to calibrate each analyser was impractical, given the limited angular range of the scattered electron analyser when the apparatus is configured for solid targets, a different method of angular calibration was used for each analyser.

Angular calibration of the ejected electron energy analyser can be performed by measuring the elastic DCSs of argon at 60, 100 and 200 eV. The elastic DCSs of argon were chosen due to the two deep minima in the 60 eV cross section at 64° and 134°, the two minima in the 100 eV cross section at 58° and 123° [116], and the single minimum in the 200 eV cross section at 110° [117]. The 60 eV cross section corresponds closest with the regular

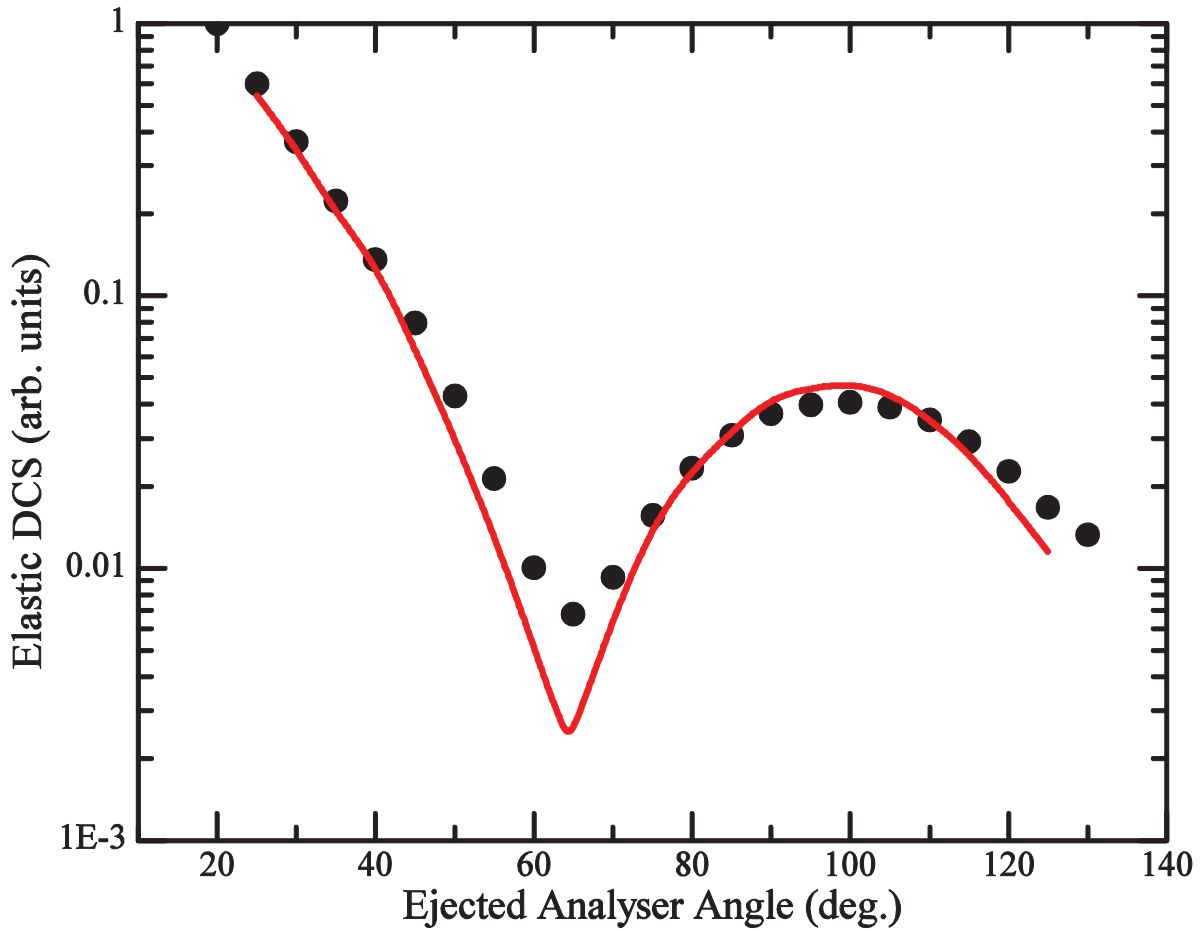

Figure 3.16: The experimentally measured elastic DCS for argon at an energy of 60 eV (solid black circles) compared to the spline interpolated data of the well known cross section (solid red line) as published by Panajotovic *et al.* [116].

operating energy of the ejected electron analyser, and although the minimum at 134° is right on the cusp of the angular range the minimum at 64° is very well defined and it is generally sufficient to calibrate to this minimum alone (see figure 3.16 for an example). Using these elastic DCSs, the accuracy of the angular calibration shows a variation less than 1°. As the scattered electron energy analyser operates in an angular range of ±20°, and the scattered analysers angular range is restricted to below ±60° by the ejected analyser and the in-plane needle mount, the angular calibration of the scattered analyser was calculated using the symmetry of the DDCS about 0°, as shown in figure 3.17. This method is very sensitive due to the rapidly changing DDCS at angles quite close to zero, and as such an angular calibration accuracy with variation of less than 0.5° can be achieved in this manner.

3.4.3 Spectrometer Consistency

Consistency checks of the (e, 2e) spectrometer are performed to ensure the reliability of the measured experimental cross sections. Two types of consistency checks can be performed:

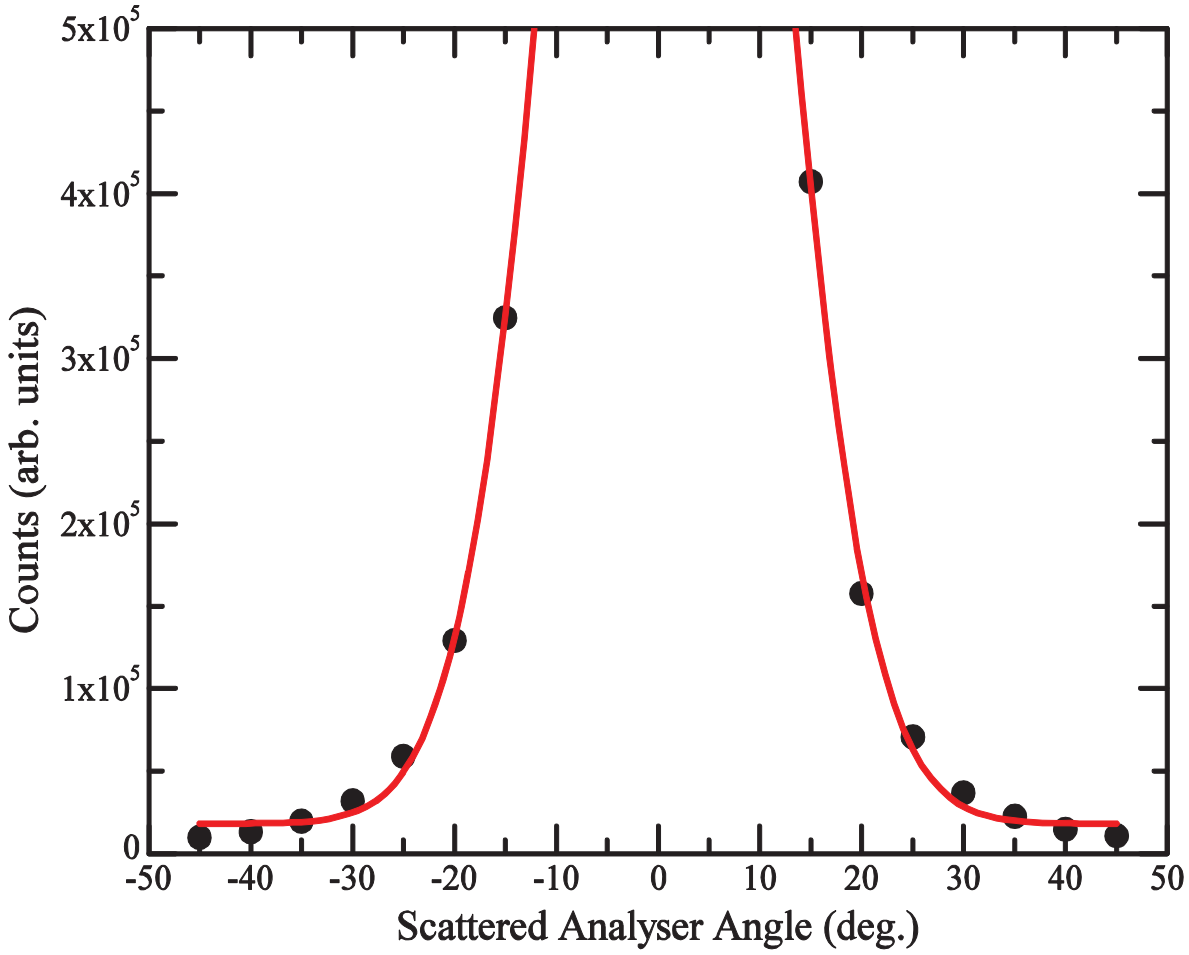

Figure 3.17: The experimentally measured DDCS of the scattered electron analyser, performed symmetrically about 0° using a helium target.

DDCS and TDCS measurements of well known cross sections. The first check can be used to determine if there is a volume overlap of the incident electron beam and target gas beam with the acceptance profiles of the individual outgoing electrons, achieved by varying the angular position of each analyser. Variations of the volume overlap should manifest itself as fluctuations in the measured cross sections, which would indicate some misalignment of the spectrometer. To determine any variation in the volume overlap, the DDCS of helium at an incident electron energy of 200 eV for ejected electron energies of 50 eV is measured. The DDCS is used as it is very sensitive to volume overlap [95], as a result of fewer degrees of freedom by comparison to the TDCS. Figure 3.18 is a plot of the helium DDCS for an ejected electron energy of 50 eV. The measured cross section shows good agreement with the available experimental data of Shyn and Sharp [118] which was used for comparison. However, there is evidence to suggest that there are issues with the measurements of Shyn and Sharp (see [93] for example), particularly at small scattering angles. The present data is also compared with the CCC calculation of Röder *et al.* [93], at the same incident energy but

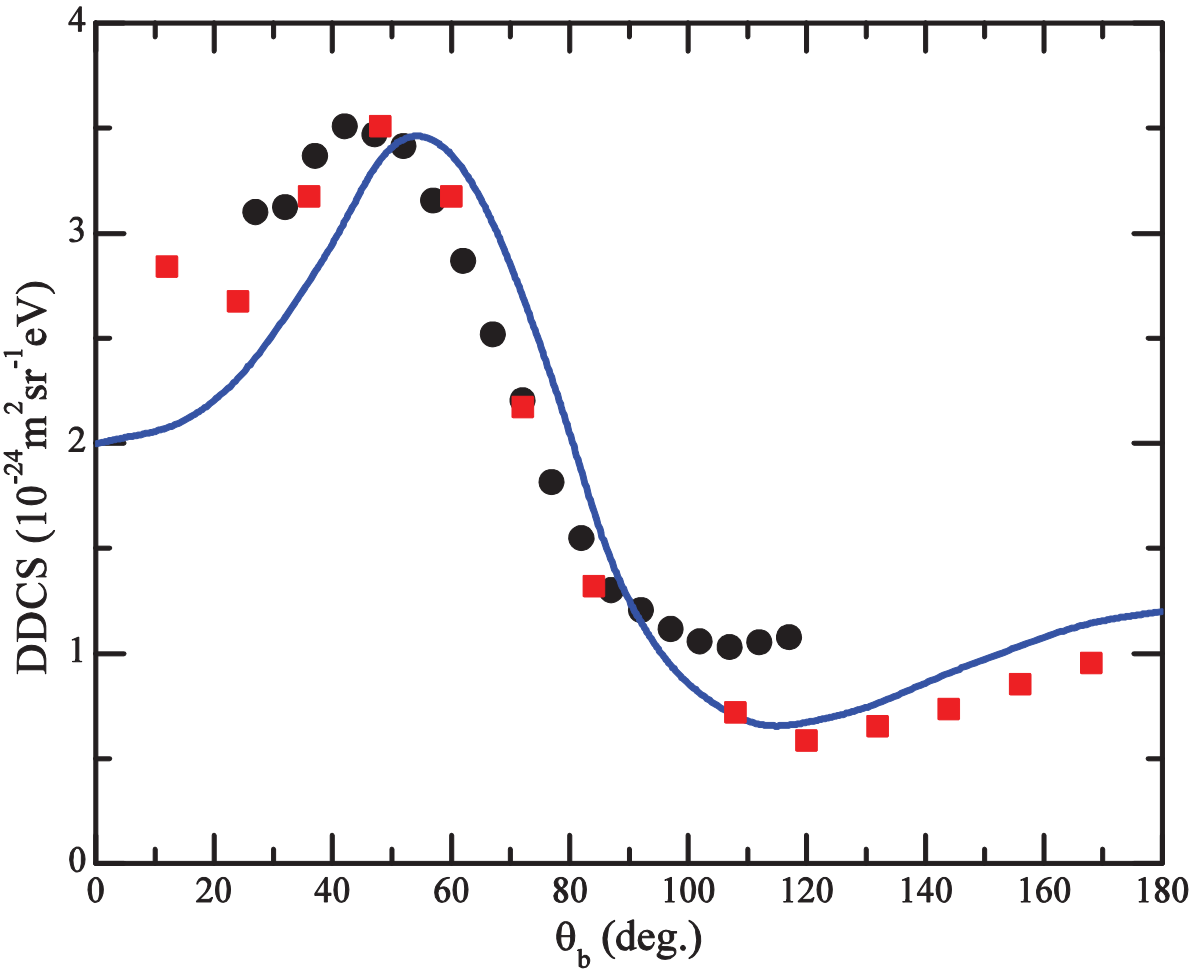

Figure 3.18: The DDCS for the ionization of helium by 200 eV electrons resulting in 50 eV ejected electrons (solid black circles) compared to the published experimental data of Shyn and Sharp [118] (solid red squares) and to the CCC calculation of Röder *et al*. [93] for a lower ejected electron energy of 40 eV.

with a slightly lower ejected electron energy of 40 eV. The present DDCS deviates from the theoretical calculation at backward angles and very forward scattering angles, indicating that there may be some misalignment in these regions.

The final consistency check is performed by measuring a TDCS under the same kinematic conditions of a known TDCS, which is sensitive to the overlap of all the elements of the spectrometer. The TDCS measurement is typically performed for helium, whose cross sections are well known experimentally and theoretically. Figure 3.19 shows the experimental TDCS of helium for 250 eV incident electrons, 10 eV ejected electrons, with the scattered electron detected at -15°. The present data is compared to the experimental data of Milne-Brownlie *et al.* [25] under the same kinematic conditions. These conditions were selected for this consistency check as the experimental results presented within this thesis are performed under similar kinematics. Comparison is also made to a convergent close-coupling (CCC)

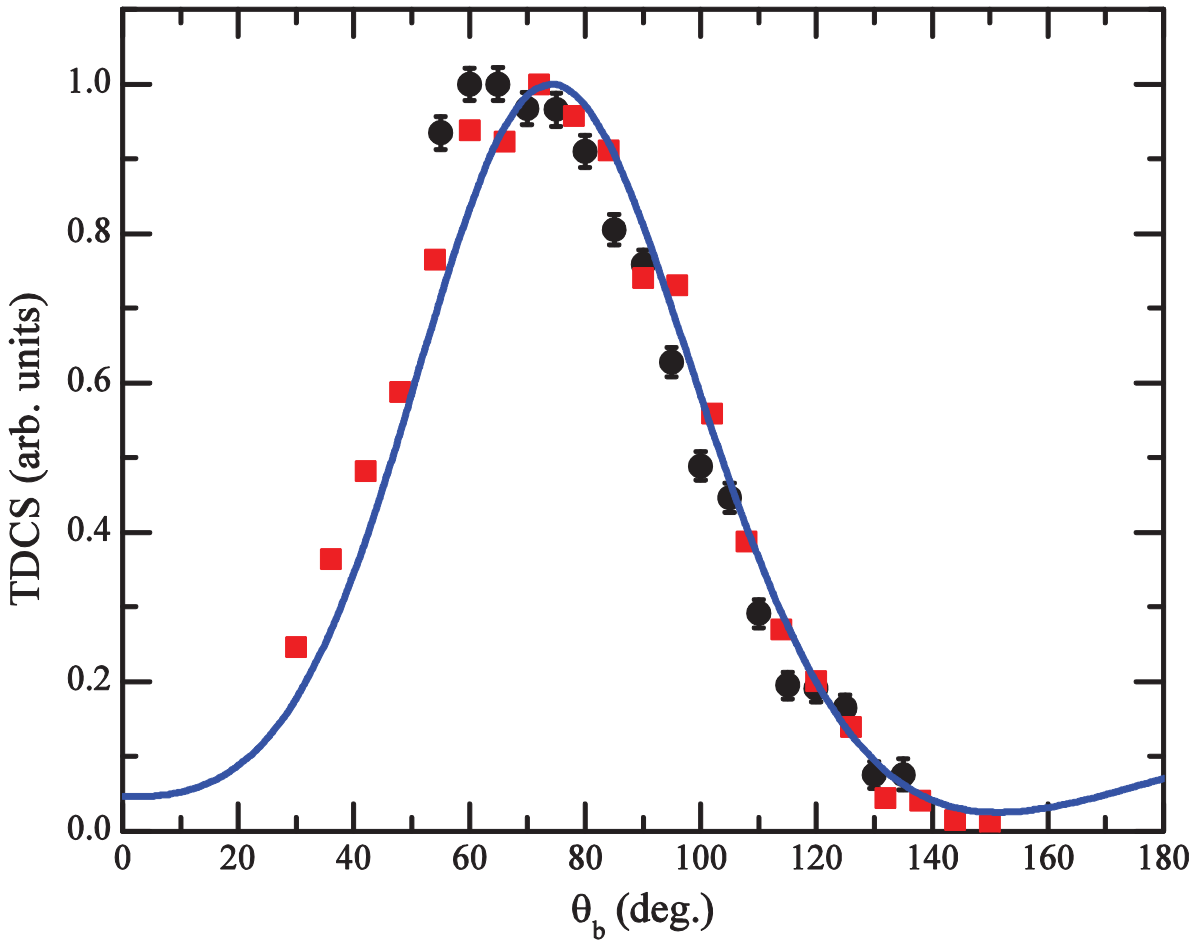

Figure 3.19: The measured helium TDCS for an incident electron energy of 250 eV, an ejected electron energy of 10 eV and a scattering angle of -15° (solid black circles). The data is compared to the published experimental TDCS of Milne-Brownlie *et al.* [25] (solid red squares) under the same conditions. Comparison is also made with the CCC calculation of Bray for the same kinematics [119] (solid blue line).

calculation for the same conditions computer by Bray [119]. The CCC method has been very successful at reproducing triple differential cross sections for atomic s-states, particularly helium (see [120] for a review of helium CCC). In short, the CCC method solves the Schrödinger equation via the close-coupling formalism by solving the Lippmann-Schwinger equation [121]. For a full description of the CCC method please see Bray and Stelbovics [122] or Fursa and Bray [12]. The present data matches the shape of the previous experimental data and the CCC calculation very well. The good shape agreement between the experimental and theoretical cross sections suggests that the spectrometer is operating in a consistent manner.

Formic Acid

4.1 Introduction

Most famously known for its role in the venom of ants and bees, formic acid is the simplest organic acid and is thought to play a key role in the formation of larger biologically relevant molecules such as acetic acid and the amino acids, the simplest of which is glycine. It was detected in the interstellar medium and has therefore been suggested as one of the earliest prototypes of a catalytic centre for enzymatic activity [123] once its anionic moiety is bound to a water molecule. Furthermore, formic acid constitutes, together with glycine, one of the simplest building blocks of more complicated biological systems [124] (see figure 4.1). Formic acid, systematically known methanoic acid, is the simplest of the carboxylic acids (HCOOH). It is a colourless, miscible liquid, with a vapour pressure of 31.8 Torr at 20°C. The melting point of formic acid is 8.4°C and its boiling point is 100.8°C. Formic acid has a significant dipole moment of 1.41 Debye, and a large dipole polarisability approximately of 22.5 $Å^3$, while its molar mass is 46.03 $gmol^{-1}$ [125].

To date, the majority of experimental studies of this molecule involving electron impact have been of dissociative electron attachment (DEA) [102-104]. These studies reveal different resonances leading to the decomposition of formic acid into $HCOO^-$, OH^-, O^{2-} and H^+. The main resonance is found between 1.25 and 1.4 eV and is correlated with the formation of the formate anion ($HCOO^-$). Electron transmission spectroscopy experiments [126-127] and total scattering cross section measurements [128] reveal a resonant state at approximately 1.7-1.8 eV due to electron attachment into the π^* orbital of the molecule. According to the energy range, this negative ion π^* resonance is likely responsible for the decomposition of the molecule into the formate ion. Energy loss spectra for both the formic acid monomer and dimer are also present in the literature [127, 129]. Absolute differential scattering measurements for formic acid have appeared in the literature recently. Vizcaino *et*

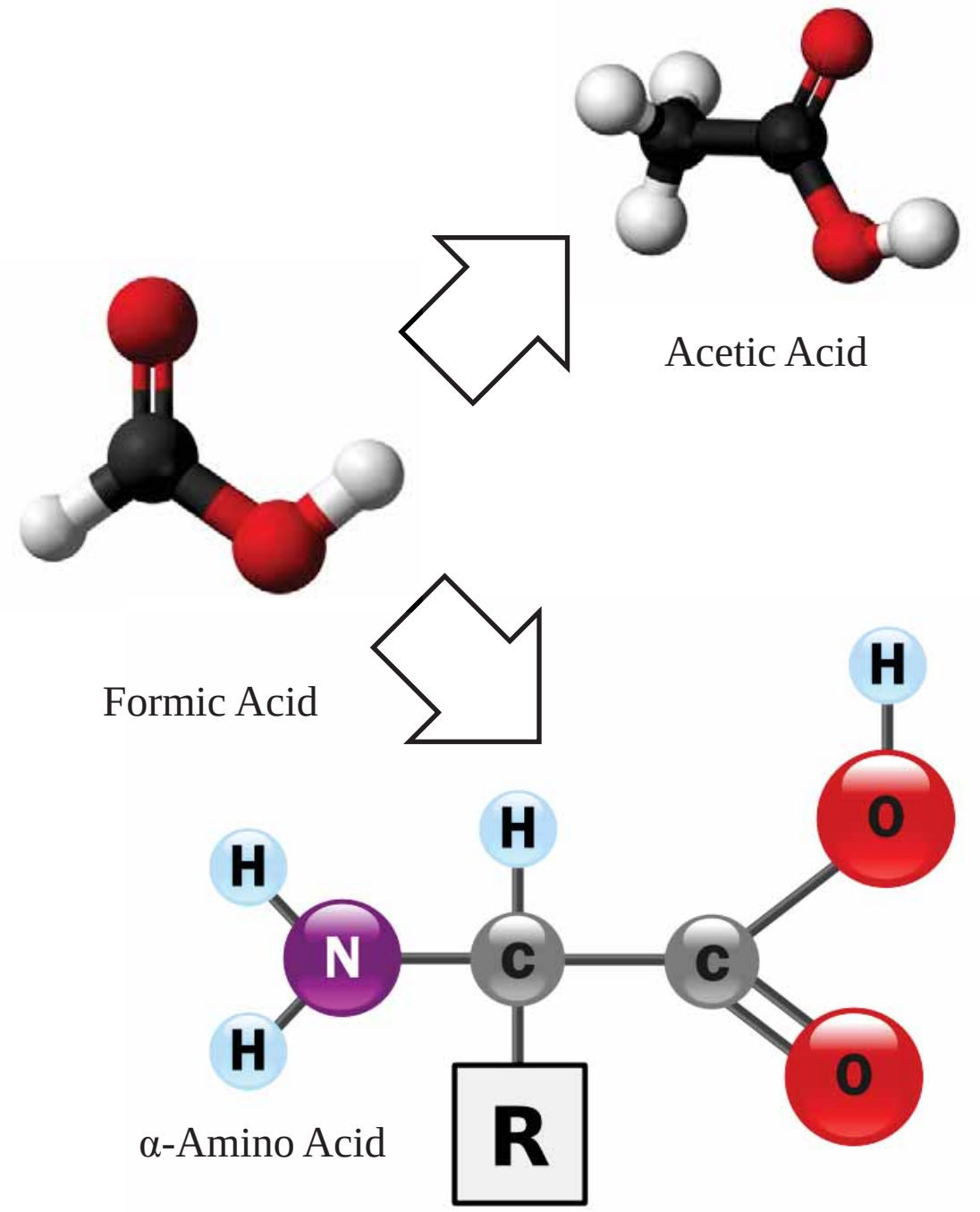

Figure 4.1: The molecular structure of formic acid [130], as well as the role of formic acid in forming much larger biological molecules including acetic acid [131] and the α-amino acids [132], the simplest of which is glycine whereby the R group is replaced with a single hydrogen atom.

al. [61] published normalized elastic SDCS for incident electron energies between 1.8 eV and 50 eV and electron detection angles between 10° and 130°, as well as ICS and MTCS data inferred from these results. Although the π* resonance is not observed, important measurements were made concerning the effects of dimer formation and the relative effects of the -*cis* and -*trans* conformers. Allan [133] reported formic acid differential cross sections for vibrational excitation at 135°, from threshold up to 5 eV, with strong observation of the π*

resonance reported in this case around 2 eV. The structure of formic acid has been rigorously probed by three EMS studies [134-136] where the latter study constituted the first EMS study of the formic acid monomer without contributions from the dimer. To the authors' best knowledge, no dynamical studies exist for formic acid.

On the theoretical side, Gianturco and Lucchese [137] carried out calculations to locate resonant states for formic acid in the low-energy region and found two distinct resonances, a π^* at around 3 eV and another resonance at approximately 12 eV. They believe that this π^* resonance leads indirectly to the dissociation of the molecule via vibrational energy redistribution from the C=O bond to the dissociative O-H stretching mode. Utilising a different theoretical approach, Rescigno *et al.* [87], localized this negative ion π^* resonance at 1.9 eV with a FWHM of 0.2 eV at equilibrium geometries and in the elastic SDCS. They noted that the direct dissociation of the π^* anion in a planar geometry to produce the formate anion is a symmetry forbidden process and that a second anion state, connected to the π^* state through a conical intersection at non-planar geometries, is involved in the dissociation mechanism.

4.2 Sample Preparation

The formic acid vapour target enters the interaction region via a 0.69mm stainless steel capillary. The vapour is obtained from a liquid sample held in a glass vial, of 98% stated purity (Sigma-Aldrich, Australia), and further purified via several freeze-pump-thaw cycles. The vapour is a mixture of monomers and dimers whose ratio is a function of temperature and driving pressure. At higher operating temperatures, the extra kinetic energy serves to break up most of the dimers into monomers. It was demonstrated in Nixon *et al.* [135] that at temperatures in excess of 120°C, the target is composed of greater than 99% monomers. As a result, the beam-forming needle is held at approximately 135°C, while the associated gas handling system and vacuum chamber are heated to approximately 75°C and 50°C respectively to prevent condensation in the gas lines and on the chamber walls.

4.3 Binding Energy Spectrum

Before angular distributions of formic acid can be measured, it is necessary to collect a coincidence binding energy spectrum to select the molecular state that is to be investigated. Figure 4.2 shows a coincidence binding energy spectrum of the outer valence region of formic acid, where the incident and ejected electron energies are fixed at 250 eV and 10 eV respectively, while the scattered electron energy is scanned across a range of energies. The

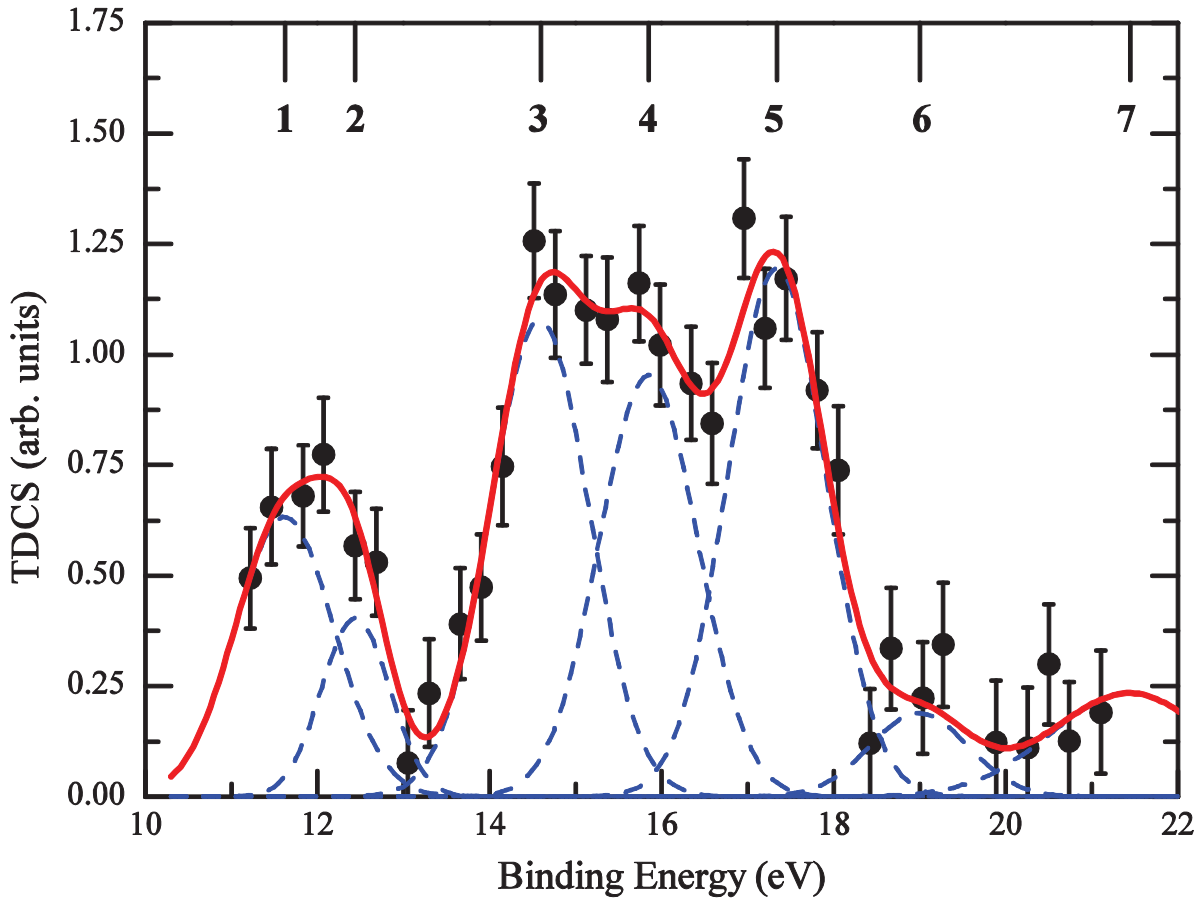

Figure 4.2: Measured coincidence binding energy spectrum for the outer valence region of the formic acid monomer, fitted with a sum of Gaussian functions for which the width parameter had been fixed as the binding energy resolution of the spectrometer (1.5eV FWHM).

	Molecular Orbital	Present Results	EMS [135]	PES [138]
1	10a′	11.6 (6)	11.5	11.5
2	2a″	12.5 (4)	12.65	12.6
3	9a′	14.6 (6)	14.7	14.8
4	1a″	15.8 (6)	15.8	15.8
5	8a′	17.3 (6)	17.15	17.1
6	7a′	19.0 (6)	17.9	17.8
7	6a′	21.5 (9)	22	22

Table 4.1: Formic acid binding energies (in eV), with the error in Gaussian peak position quoted in parentheses. EMS data is reported from Nixon *et al.* [135] and PES data is reported from Von Niessen [138].

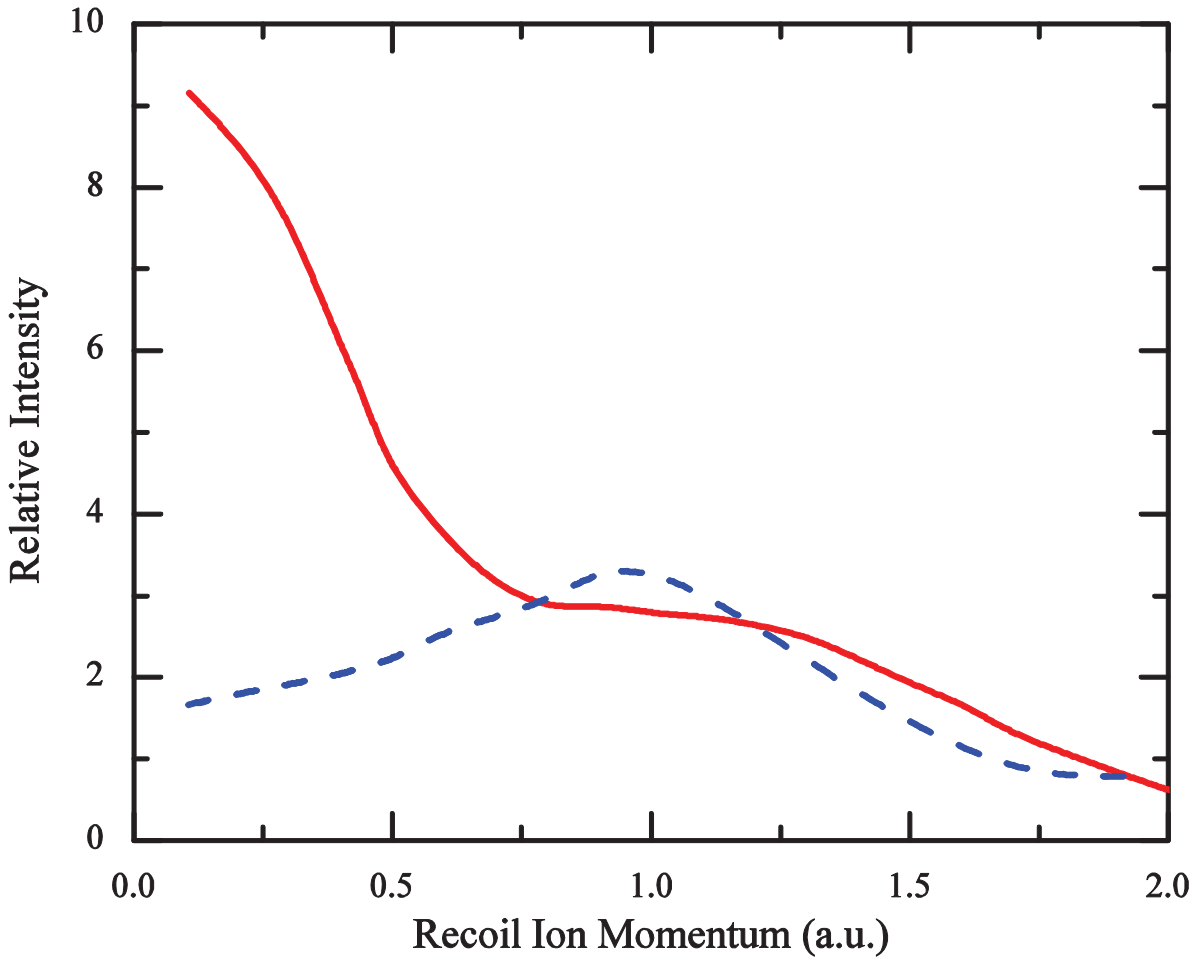

Figure 4.3: The momentum density profiles for the 10a′ (solid red line) and 2a″ (dashed blue line) molecular orbitals of formic acid, as published by Bharathi *et al.* [134]

detection angles for the scattered and ejected electrons were chosen to be -5° and 90° respectively. This sets the ejected electron detection angle 30° greater than the momentum transfer direction to ensure that contributions from both s-type and p-type orbitals would be evident.

The outer valence region of formic acid consists of seven molecular orbitals: five in the molecular plane (a′) and two out of the molecular plane (a″) [134]. All seven of the orbitals can be resolved partially, however due to the limited binding energy resolution of the apparatus and the intensity of each molecular orbital under the chosen conditions, not all orbitals can be completely separated. The binding energy spectrum has been fitted with a sum of Gaussian functions for which the width parameter has been fixed as the binding energy resolution of the spectrometer. The fitting of binding energy spectra usually requires the Gaussian widths to be a convolution of the instrumental energy resolution and the natural widths, obtained from photoelectron spectroscopy (PES) data, of the orbitals in question. However, given the narrow widths of the orbitals of formic acid [138] compared to the

binding energy resolution, it is valid in this instance to ignore the natural widths of the molecular orbitals. Table 4.1 shows the binding energy of each orbital, as well as the assignments and energies as determined via EMS [135] and PES [138].

In this chapter, I present angular distributions for the summed outermost valence orbitals (10a′+2a″). Examination of the momentum density probability distributions for the 10a′ and 2a″ orbitals (presented in Bharathi *et al.* [134]) indicates that, for all scattering angles considered here, one may expect the contribution of the 10a′ orbital to be considerably larger than that of the 2a″ orbital at ejected electron angles around 60°, and the contributions to be approximately equal at angles around 120° (see figure 4.3. for a comparison).

4.4 Angular Distributions

Figures 4.4 and 4.5 show the measured triple differential cross sections for the summed 10a′ and 2a″ orbitals of the formic acid monomer at an incident energy of 100 eV and an ejected electron energy of 10 eV, for scattered electron angles of -10° and -15° respectively. Comparison is made with a molecular three body distorted wave (M3DW) calculation with and without correlation, polarization and exchange terms included (CPE), for the 10a′ orbital only [41]. The M3DW calculation implements the orientation-averaged molecular orbital (OAMO) approximation to make molecular cross sections of randomly oriented molecules computationally viable. Unfortunately the OAMO is not valid for the 2a″ molecular orbital since the average is zero for this symmetry, and as such only calculations for the 10a′ orbital are available. As the experimental data are not on an absolute scale, they have been normalized to the M3DW-CPE calculation so as to give the best visual fit in the recoil region. I have used the recoil region for the normalisation since, from the work of Bharathi *et al.* [134], it is known that the shape and width of the binary peak will be strongly affected by the 2a′ state, which cannot be accounted for in the theory.

It is clearly evident from the relative size of the peaks in the binary and recoil regions that a large amount of interaction between the ejected electron and the target nucleus is present at these energies. The M3DW and M3DW-CPE calculations achieve reasonable qualitative agreement with the experimental results in figures 4.4 and 4.5, but tend to predict a larger and sharper binary peak than is observed in the experiment. The simpler M3DW agrees well with the shape of the recoil peak and while the addition of the CPE terms improves the binary peak to recoil peak ratio, it appears to worsen the shape agreement in the recoil region. However, since the theoretical calculation is for the 10a′ orbital only while the experiment is summed 10a′+2a″, it is difficult to evaluate the accuracy of the theory. For example, the fact that the M3DW gives the best agreement with the shape of the recoil peak may be fortuitous

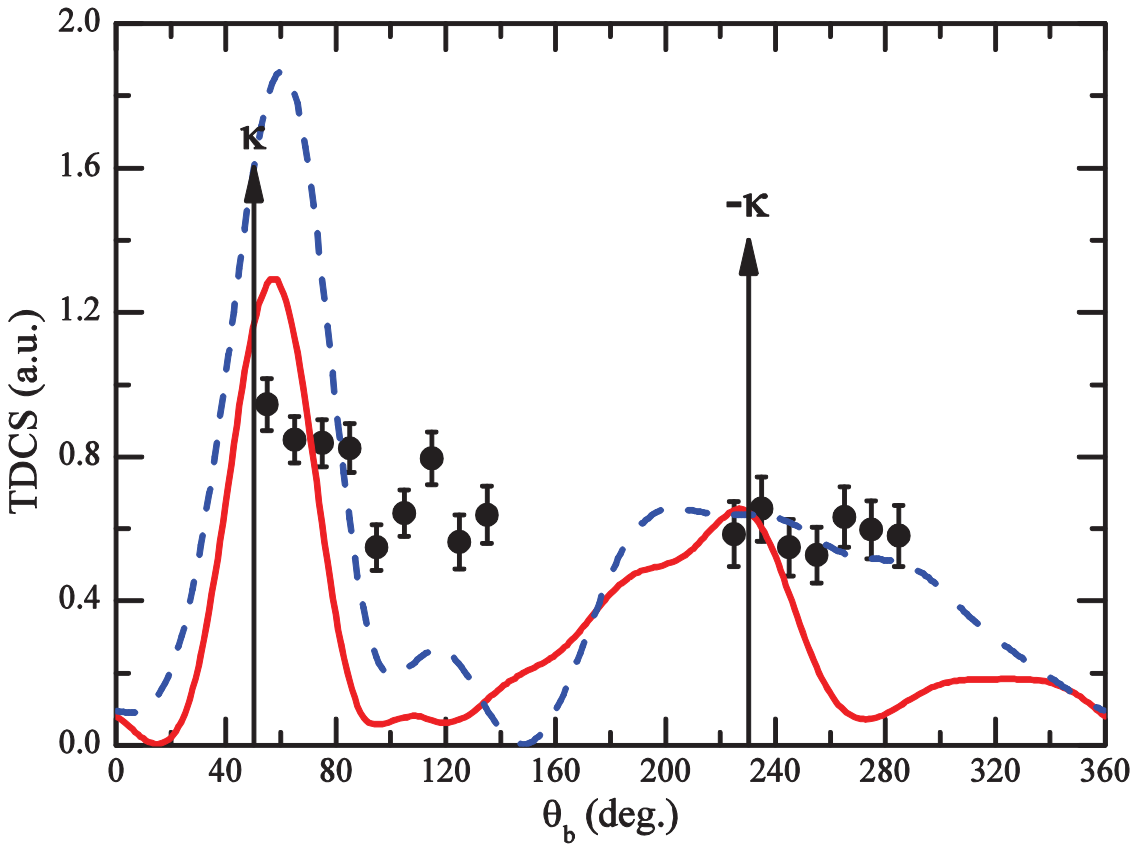

Figure 4.4: Experimental triple differential cross sections for the 10a′+ 2a″ valence orbitals of formic acid (solid black circles), with E_0=100 eV, E_b=10 eV, θ_a=-10° and $|\boldsymbol{\kappa}|$=0.54 au, compared with M3DW-CPE (solid red line) and M3DW (dashed blue line) calculations for the 10a′ orbital only.

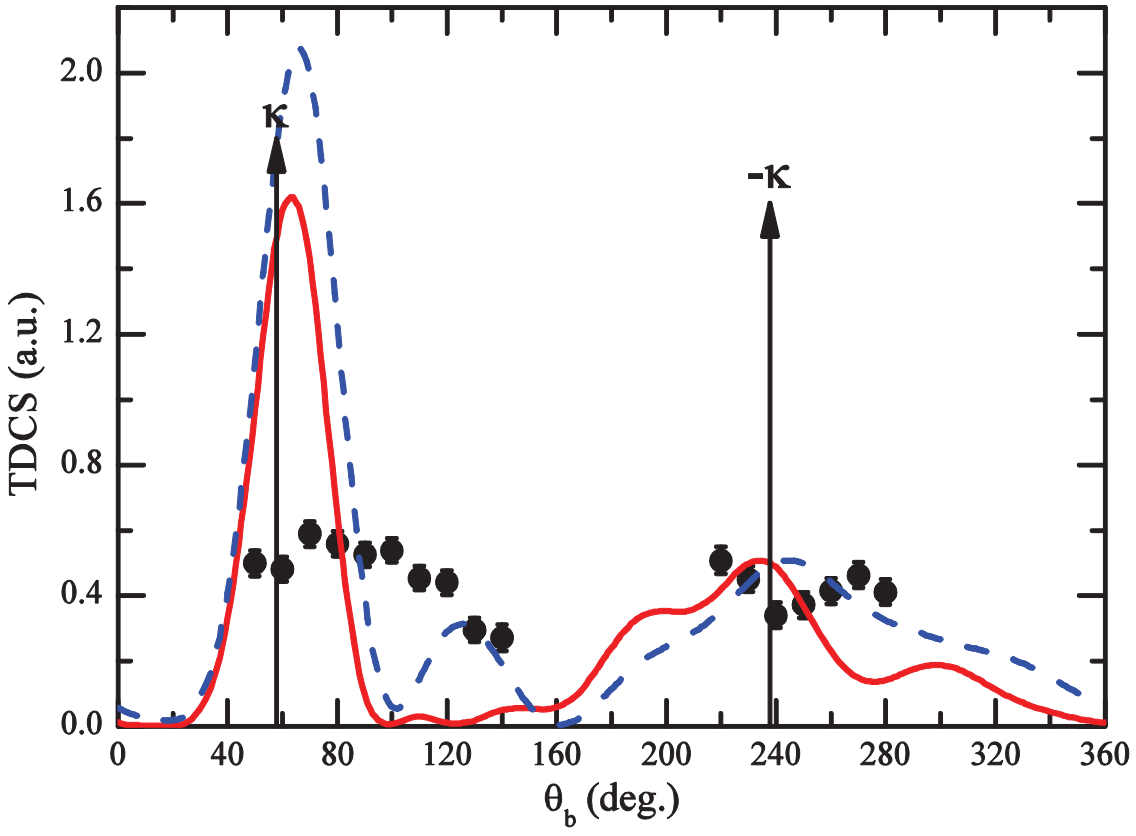

Figure 4.5: Same as figure 4.4, except that θ_a=-15° and $|\boldsymbol{\kappa}|$=0.74 au.

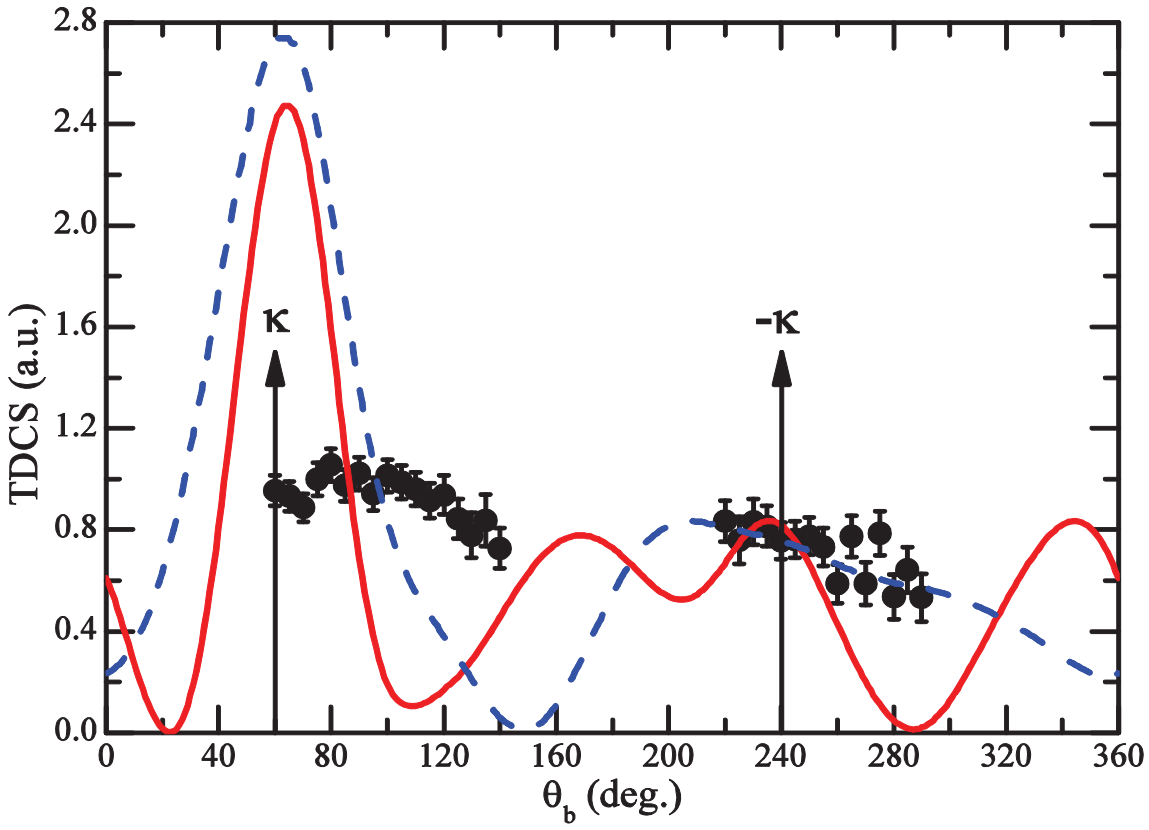

Figure 4.6: Experimental triple differential cross sections for the 10a′+ 2a″ valence orbitals of formic acid (solid black circles), with E_0=250 eV, E_b=10 eV, θ_a=-5° and $|\boldsymbol{\kappa}|$=0.42 au, compared with M3DW-CPE (solid red line) and M3DW (dashed blue line) calculations for the 10a′ orbital only.

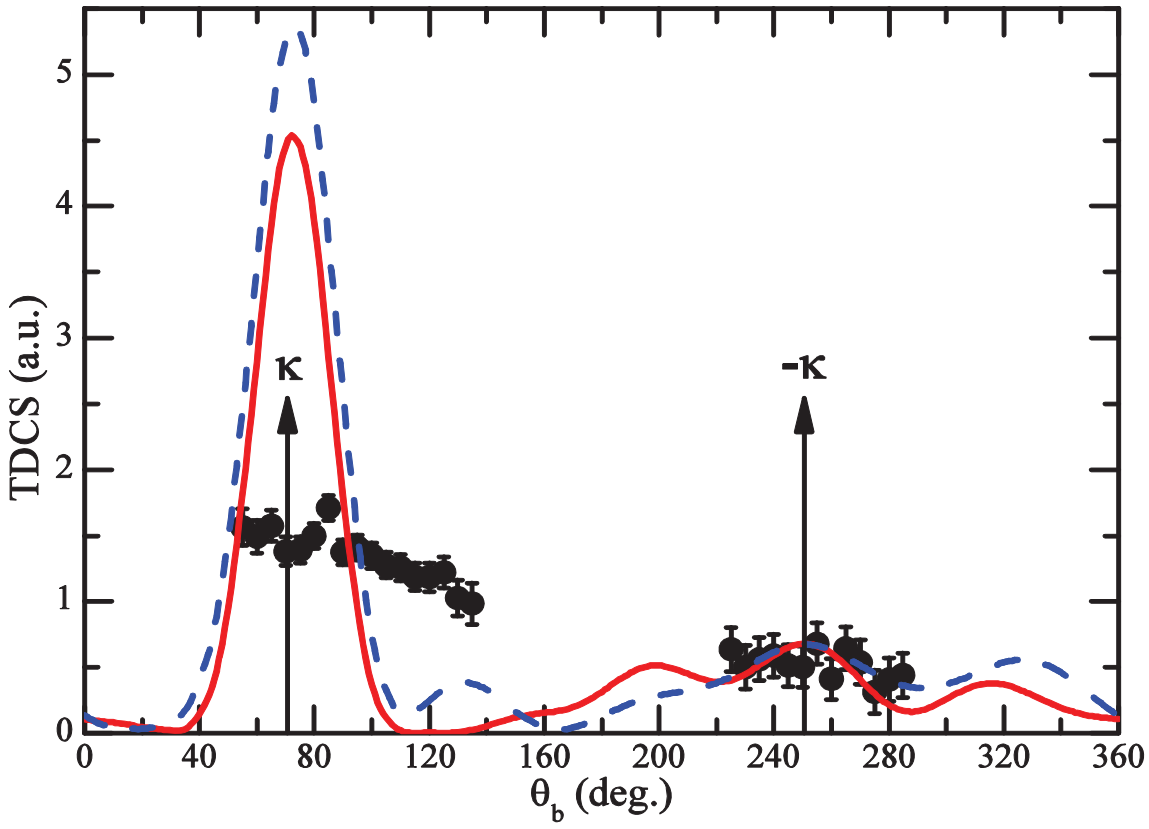

Figure 4.7: Same as figure 4.6, except that θ_a=-10° and $|\boldsymbol{\kappa}|$=0.75 au.

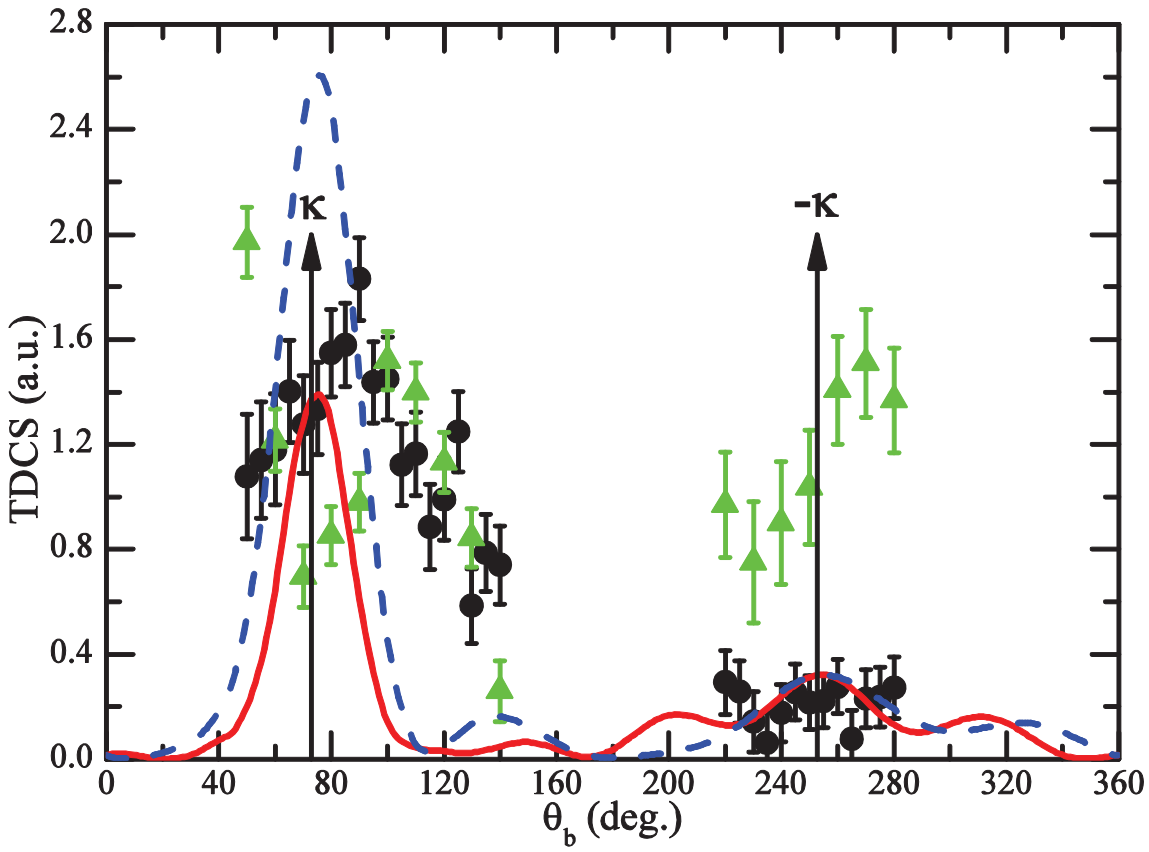

Figure 4.8: Same as figure 4.6, except that θ_a=-15° and $|\boldsymbol{\kappa}|$=1.11 au. The previous experimental results for the $3a_1$+$1b_1$ molecular orbitals of water [38] are also presented here (solid green triangles).

since it is quite possible that the M3DW-CPE gives the correct shape and the additional width of the peak comes from the 2a″ orbital. The additional experimental structure in the binary peak for angles between 90°-120° very likely originates from the 2a″ orbital. Although the details of the cross section will undoubtedly be different for the present kinematics, I believe this proposition is again supported by an examination of the momentum density profiles reported by Bharathi *et al.* [134]. Plotting their momentum profiles against ejected electron angle, and summing the profiles, indicates that the resultant cross section is enhanced in the region from 90°-120°, compared with the cross section for only the 10a′ orbital.

Figures 4.6-8 present the TDCS for electron impact ionization of formic acid with 250eV incident electrons, measured for 10eV ejected electrons, for three scattered electron detection angles of -5°, -10° and -15° respectively. Comparison is again made with the M3DW and M3DW-CPE calculations for the same kinematic configurations. The experimentally determined TDCS for ionization of the summed $1b_1$+$3a_1$ valence orbitals of H_2O [38] under the same kinematics are also presented in figure 4.8. Immediately clear is the difference in the relative size of the binary and recoil peaks at an incident energy of 250 eV when compared to the lower incident energy case. As the scattered electron angle changes

from -5° to -10° to -15°, the magnitude of the recoil peak relative to the binary peak decreases significantly, in contrast to the case in figures 4.4 and 4.5, where the binary-to-recoil ratio is approximately constant as the scattering angle is changed from -10° to -15°. The relative magnitude of the recoil peak compared to the binary peak at a scattering angle of -15° (figure 4.8) is in stark contrast to the data from [38] for H_2O, which under the same conditions produces a recoil peak approximately 4 times greater. In a recent study [139], out of plane TDCS measurements for H_2 and He were compared, and through the use of state-of-the-art theory, certain structures were determined to arise from recoil interactions, the magnitude of which could be increased by minimising the internuclear separation of H_2 to the extent that it represents the localised single centre nuclear charge of helium. In light of this, it seems reasonable to suggest that this lack of recoil interaction in formic acid may be attributed to the molecule's polycentric nature and thus the lack of nuclear charge at the centre of mass, as opposed to the water molecule which has a single oxygen nucleus at its centre (see figure 4.9). Given the location of the centres of mass in tetrahydrofuran and thymine (see figure 6.2 for centres of mass for the nucleobases), little recoil interaction is expected for these two molecules.

In comparison with the theoretical calculations, the M3DW again predicts quite well the shape of the recoil peaks in all cases, and there is also improved agreement with the M3DW-CPE in this region, especially at the larger momentum transfers. The relative size of the binary and recoil peaks is still predicted with greater agreement by the M3DW-CPE, however both calculations still fail to correctly predict the size and shape of the binary peak, with the exception of figure 4.8, where the M3DW-CPE successfully predicts the correct relative magnitudes of the binary peak and the recoil peak, and the sharper binary peak observed at this larger momentum transfer more closely resembles the peak predicted by the calculation. The sharper binary peak for this set of conditions may be an indication of a smaller contribution from the 2a″ orbital, however this is difficult to conclude with any certainty without being able to resolve the individual molecular orbitals.

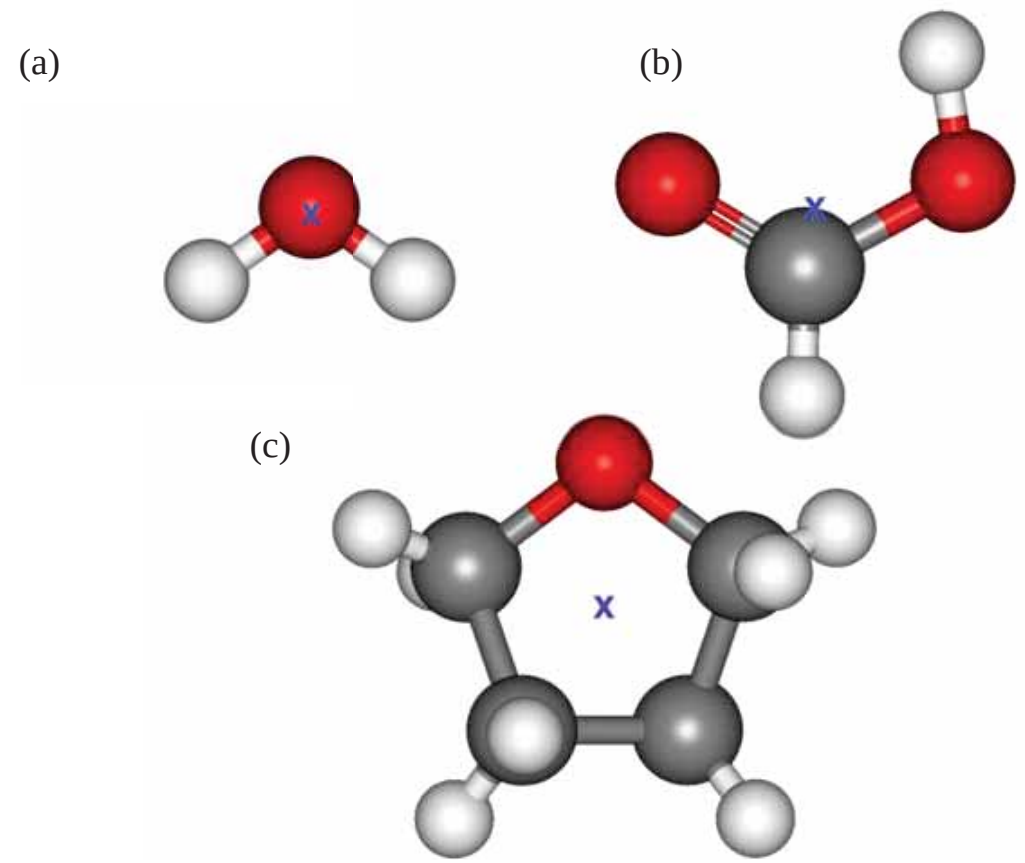

Figure 4.9: The molecular structures of (a) water, (b) formic acid and (c) tetrahydrofuran. Spheres are used to represent carbon (grey), oxygen (red) and hydrogen (white). The centre of mass is denoted with a blue cross.

Tetrahydrofuran

5.1 Introduction

Tetrahydrofuran (THF) is a common organic solvent used in large amounts for a variety of industrial purposes [140]. THF is a large polyatomic ring molecule with molecular formula of C_4H_8O. It is a colourless liquid, having an ether-like odour and a vapour pressure of 129 mTorr at 20°C. The melting point of THF is -108°C and its boiling point is 66°C. THF has a significant dipole moment of 1.63 Debye, a dipole polarisability of 7.97 $Å^3$ and a molar mass of 72.11 $gmol^{-1}$[125].

There is also significant interest in THF as it presents a simple model for the deoxyribose building block of DNA. In particular, the backbone of DNA may be considered as a series of THF molecules held together by phosphate bonds to which the important bases are attached (see section 6.1 for more information regarding DNA). The objective of the present study is to understand how electrons interact with this simple model of part of the DNA backbone. Such studies may help to understand the mechanism of dissociative electron attachment, and the measurement of scattering information can be used to both test, and aid, the development of quantum scattering theory for large molecules.

THF has previously been the subject of several theoretical and experimental studies. The early study by Le Page *et al.* [141] was focused on differences in electron spectroscopy between the gas and solid phases. A resonance feature is reported for gaseous THF at 8.5 eV in the vibrational excitation of the C-H stretch modes, but is shifted approximately 1 eV lower for comparable solid state measurements. Low-energy electron damage in the solid phase was reported by Breton *et al.* [142], who discuss the production of aldehydes in terms of electron resonances, and also lists previous investigations with gas, liquid and solid state THF.

Several absolute experimental scattering measurements in the gas phase have appeared more recently. Zecca *et al.* [83] reported grand total cross-section (GTCS) measurements for

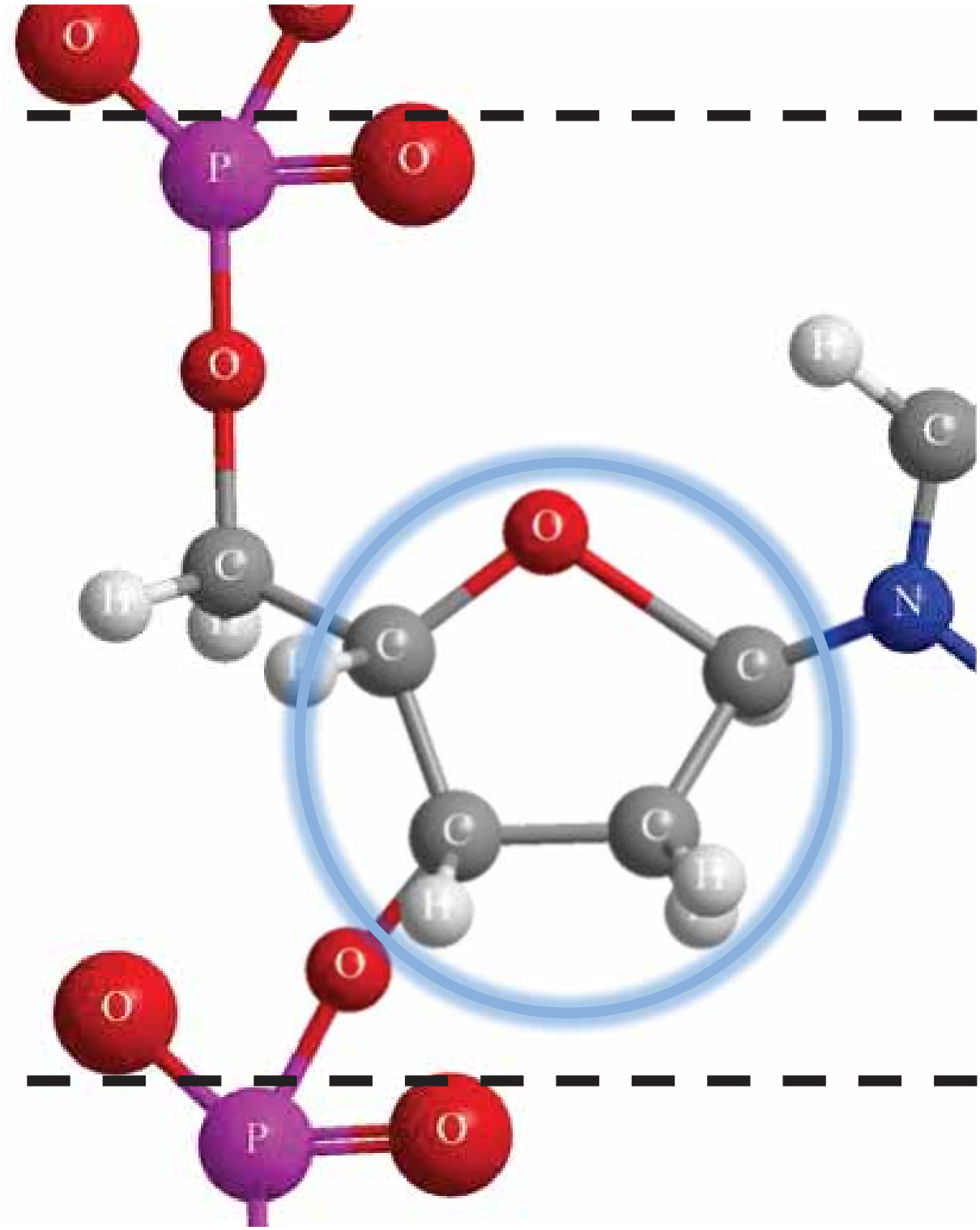

Figure 5.1: Segment of the sugar-phosphate backbone of a single strand of DNA with an attached cytosine molecule. The location of THF in the strand is highlighted by the blue ring. The repeating unit of the strand is marked by the black dashed lines.

both electrons and positrons at energies below 21 eV, while Możejko *et al.* [82] reported similar measurements, using electrons only, from 1-370 eV. Both groups observe a broad shape resonance centred around 6-8eV in the GTCS. The first single differential cross-sections for elastic electron scattering were published by Milosavljevic *et al.* [143] in the

energy range 20-300 eV for scattering angles ranging from 10° to 110°. These benchmark results, as well as the vibrational energy loss spectrum of THF, were published with a view to stimulate theoretical interest. Colyer *et al.* [80] published elastic single differential cross sections (SDCS), as well as integral cross sections (ICS) and momentum transfer cross sections (MTCS), for energies between 6.5 and 50 eV and angles from 10° to 130°. A shape resonance was observed in the elastic channel at 6.5 eV, of width approximately 2 eV FWHM, with a strong preference for backward angles. The authors also reported that preliminary results suggest the same shape resonance has a strong presence in the vibrational excitation channel. Dampc *et al.* [144] also reported elastic SDCS and vibrational excitation of the C-H stretch modes at 10 eV and for scattering angles from 20° to 180°, as well as ICS and MTCS. This study revealed resonance scattering in two energy regions, 6 eV and 9 eV, via broad shape resonances. Most recently, Allan [145] published a study of elastic SDCSs and vibrational excitation of a number of different modes. The emphasis was on the low energy regime, with angular distributions measured as low as 2 eV and excitation functions extending as low as 100 meV. Satisfactory agreement is observed with previous experimental findings, and the vibrational excitation cross sections elucidate two resonant bands at 6.2 and 10.8 eV in agreement with other recent experimental works.

Theoretical investigations concerning THF have also become more common in recent times. SDCS for elastic electron scattering have been computed by Możejko and Sanche [146] using the independent atom method (IAM) for collision energies in the range 50-2000 eV. They also calculated the cross-section for electron impact ionization of THF, from the ionization threshold up to energies of 4000 eV. Integral cross-sections, both elastic and electronically inelastic, have been calculated for THF by Bouchiha *et al.* [147] using the R-matrix method, at collision energies from 1-10 eV. Although they did not observe a shape resonance, a few core-excited resonances are reported. Trevisan *et al.* [87] completed calculations of SDCS and momentum transfer cross sections (MTCS) of elastic electron scattering by THF using the complex Kohn variational method, and report a broad shape resonance in the 8-10 eV energy range in the MTCS. Elastic integral cross-sections for both THF and phosphoric acid, the latter of which constitutes the remainder of the DNA backbone, have been computed by Tonzani and Greene [148], who also utilised a variation of the R-matrix method. Resonances for THF have been observed around 8.6 and 14.1 eV, but the authors indicate that their model usually predict resonances 1-2 eV higher than experiment due to the use of the static exchange approximation. Most recently Winstead and McKoy [81] published elastic integral, SDCS and MTCS from deoxyribose and related molecules, including THF. Using the Schwinger multichannel method, shape resonances in the integral

cross-section and MTCS of THF are reported at energies of 8.3 and 13.5 eV, after compensating for the static exchange approximation.

While no previous dynamical (e, 2e) studies of THF have been reported in the literature, it has been investigated by EMS to study ring puckering and torsion in the ring [149-150]. As the THF molecule is a five membered heterocyclic ring compound, it is able to undergo pseudorotation. This is an internal motion that involves of out-of-plane ring puckering vibrations which occur in a way that makes the phase of the puckering rotate about the ring [151]. Three possible conformations of THF are produced by pseudorotation in the gas phase and are of C_1, C_2 and C_S point group symmetry. All three conformations are very close in energy, indeed, calculations predict that the energy differences are within the error of many computational models [149]. There has been some debate and there still is no general consensus about which conformation is the lowest energy and most populated conformer [149, 152]. However, experimental evidence indicates that both C_2 and C_S conformers coexist at room temperature. Yang *et al.* [149] compared simulated orbital momentum density probability distributions for the two conformers to distributions measured using EMS and determined that the C_S structure is the preferred conformer and the lowest energy structure. A second study undertaken by the same group at higher energy found that at room temperature around 55% of THF molecules are in the C_s conformation and 45% in the C_2 form [150]. Guiliani *et al.* [152] have determined from high-resolution photoabsorption spectroscopy supported by high-level ab initio calculations, that both conformers exist at 25°C, with a Boltzmann analysis predicting 44.5% of THF molecules are in the C_S form and 55.5% in the C_2 form. Dampc *et al.* [153] have also recently observed evidence of both conformers in photoelectron spectroscopy (PES) studies.

5.2 Sample Preparation

The tetrahydrofuran vapour target is formed in a similar manner to the formic acid vapour target. The target gas is obtained from a liquid sample held in a glass vial, of 99% stated purity (Sigma-Aldrich, Australia), and further purified via several freeze-pump-thaw cycles to remove any trapped gases. It enters the interaction region via a 0.69 mm stainless steel capillary, but unlike formic acid THF does not form dimers. This means that the gas capillary does not need to be heated to high temperatures, and as such it has been found that heating the gas lines and capillary to 75°C and the chamber walls to 50°C is sufficient to prevent condensation and clogging of the beam forming needle. Due to the reactive nature of THF, the liquid nitrogen filled cold finger is used during measurements of THF cross sections.

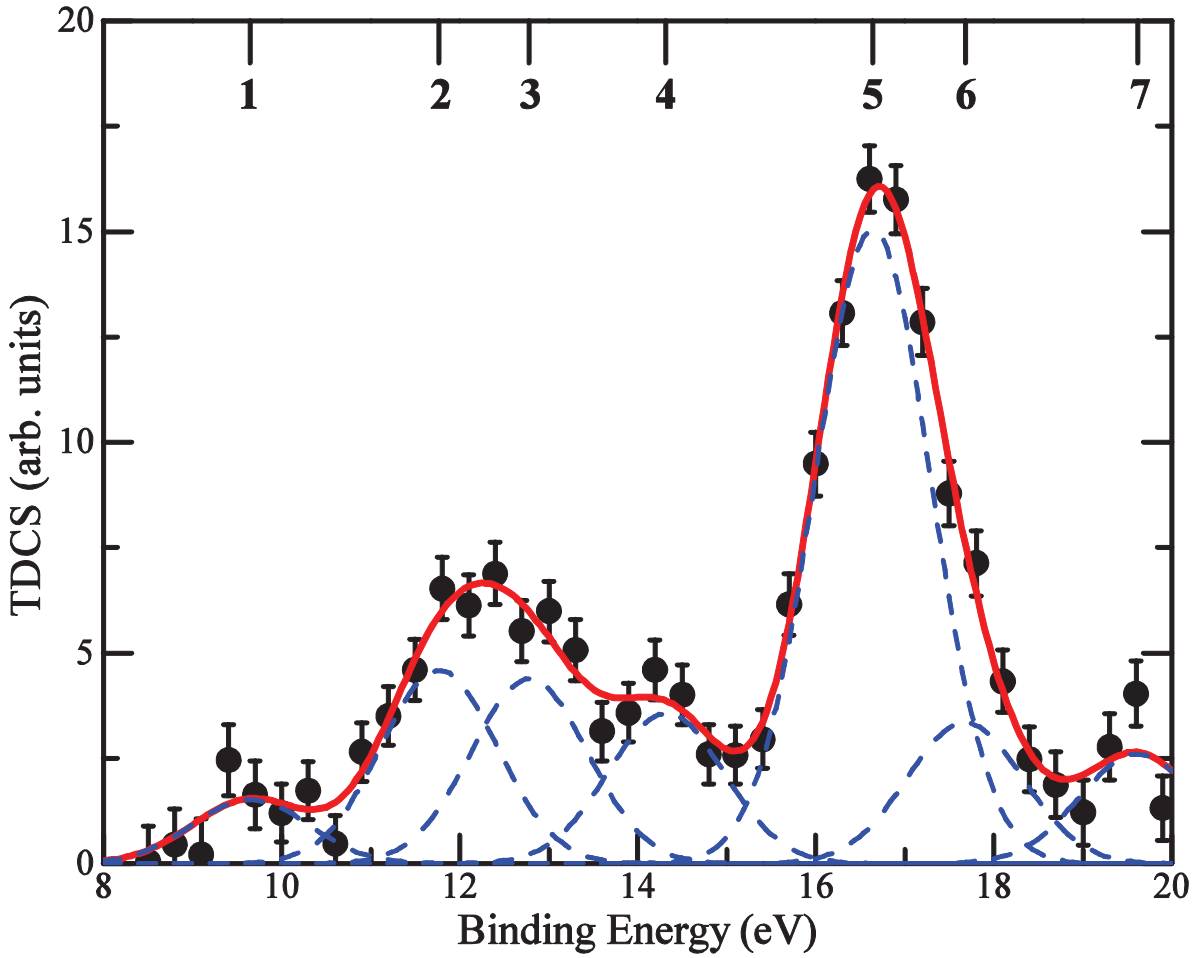

Figure 5.2: Measured binding energy spectrum for the outer valence region of tetrahydrofuran, fitted with a sum of Gaussian functions using the coincidence energy resolution as the peak width.

5.3 Binding Energy Spectrum

It is again necessary to collect a coincidence binding energy spectrum to confirm the molecular state that is under investigation. Figure 5.2 presents a coincidence binding energy spectrum for the outer valence region of tetrahydrofuran. The incident and ejected electron energies were fixed at 250 eV and 10 eV, respectively, while the scattered electron energy was scanned across a range of energies. The detection angles for the scattered and ejected electrons were chosen to be -10° and 90°, respectively. The experimental (e, 2e) binding energy resolution, known to be 1.5 eV FWHM, has been used to define the peak width parameter for fit a sum of Gaussian functions to the peaks in the spectrum. Seven Gaussian functions have been used to fit the data, as labelled 1 to 7 in figure 5.2. The fitting of binding energy spectra usually requires the Gaussian widths to be a convolution of the instrumental energy resolution and the natural widths, however, given the narrow widths of the molecular orbitals in THF compared to the binding energy resolution [154], it is again valid to ignore the natural widths of the molecular orbitals.

	Present Results	Theory [152, 149]		EMS [150]	PES [154]
		C_2	C_s		
1	9.7 (0.6)	9.94 (9b)	9.91 (12a′)	9.7	9.67
2	11.8 (0.6)	11.65 (11a)	11.65(11a′)	12.14	11.41
3	12.8 (0.6)	12.20 (10a)	11.89 (8a″)		11.99
		12.43 (8b)	12.26 (10′)		12.48
		12.62 (9a)	12.30 (7a″)		12.90
4	14.3 (0.6)	14.21 (7b)	13.74 (6a″)		14.00
		14.82 (6b)	14.49 (9a′)	14.54	14.45
		14.95 (8a)	15.29 (5a″)		15.29
5	16.6 (0.6)	16.57 (7a)	16.29 (8a′)	16.74	16.70
6	17.7 (0.6)	16.93 (5b)	16.83 (7a′)		
7	19.6 (0.6)	18.64 (6a)	18.67 (6a′)	19.74	19.42

Table 5.1: Tetrahydrofuran binding energies (in eV), with the error in the Gaussian peak position quoted in brackets. Giuliani *et al.* [152] do not report energies and orbital assignments for the peak designated number 7, so instead assignment and energies are reported from Yang *et al*. [149] in this instance.

The outer valence region of THF is complicated by the presence of many molecular orbitals, indeed there are eleven molecular orbitals for each of the C_2 and C_s conformers of THF that are calculated to lie within the binding energy range presently measured. This is without considering the orbitals resulting from the C_1, which have been discounted on the basis of previously published works [150, 152]. The highest occupied molecular orbitals (HOMOs) of THF are dominated by the O(2p) and H(1s) orbitals [154]. Table 5.1 shows the binding energy for each orbital, as well as the assignments and energies as determined via EMS [150] and PES [154]. As the resolution of the coincidence spectrometer is relatively large, it is insufficient to resolve contributions from the two major conformers. Photoelectron

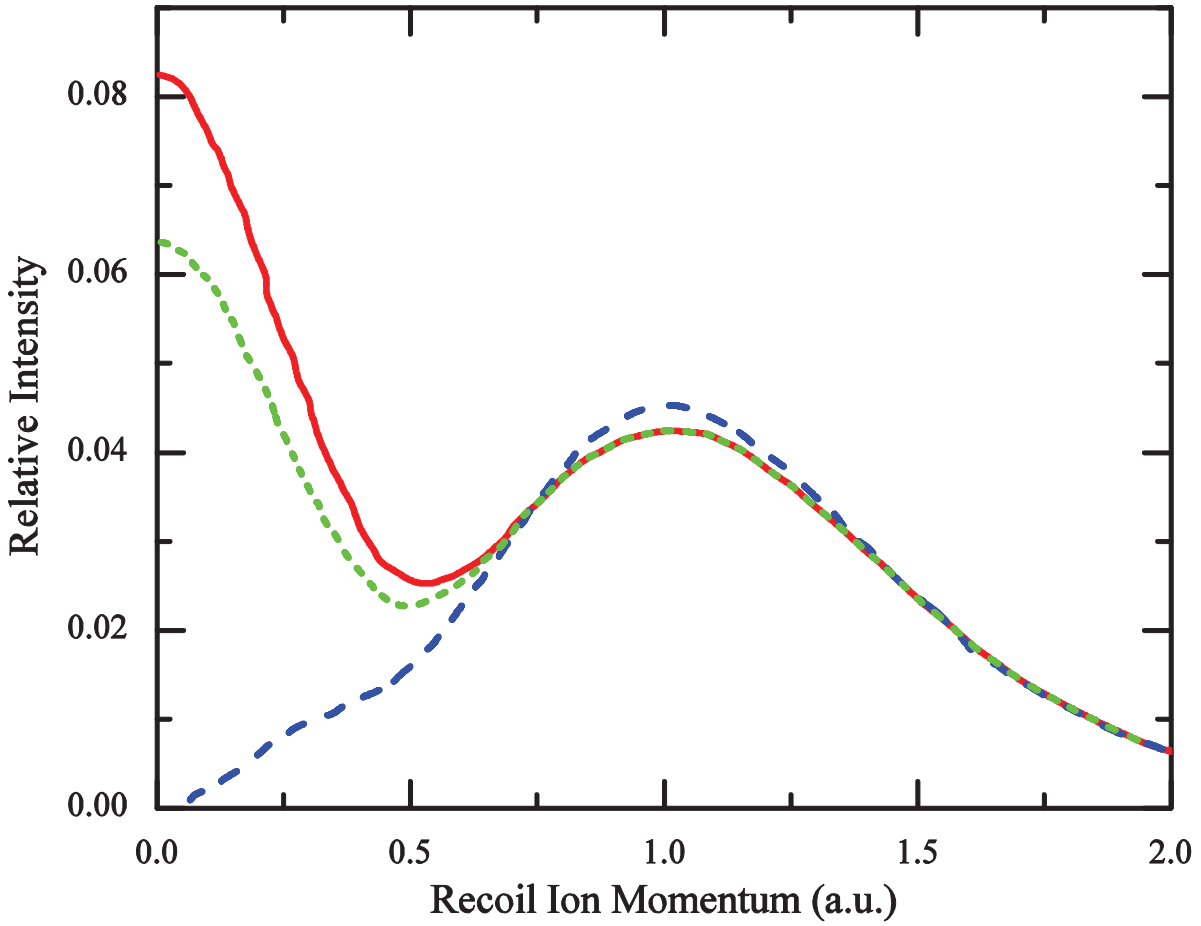

Figure 5.3: The momentum density profiles for the 12a′ (solid red line), 9b (dashed blue line) and 20a (short dashed green line) molecular orbitals of tetrahydrofuran which correspond to the C_S, C_2 and C_1 symmetries respectively, as published by Duffy *et al.* [155].

spectroscopy measurements of Giuliani *et al.* [152] with a significantly higher resolution of 50 meV also found the two conformers indistinguishable, although they were able to observe vibrational structure associated with excitation of the ground ionic state in these measurements. The first peak in figure 5.2 at an energy of 9.7 eV is fitted by a single Gaussian function and assigned to the combined outermost valence orbitals of THF, 9b and 12a′, which correspond to the HOMO of the C_2 and C_S conformers, respectively. This first peak is not completely resolved from the next broad peak in the experimental data, the HOMO-1, which has been fitted with two Gaussian functions and includes contributions from up to eight orbitals, four attributed to each conformer. As a result there may be small contributions to the measured TDCSs from this energy overlap.

In this chapter I present triple differential cross sections for the ionization of the combined highest occupied molecular orbitals (12a′+9b) of tetrahydrofuran, corresponding to the outermost orbitals of the C_2 and C_S conformers. The experiments were performed at a relatively low incident electron energy of 250 eV, whilst the ejected electron energy was

chosen to be 10 eV. Examination of the momentum density probability distributions for the HOMO presented earlier in Ning *et al.* [150] and later in Duffy *et al.* [155], indicates that for recoil ion momenta below 0.5 au, one may expect the contribution from the 12a′ orbital to be considerably larger than that of the 9b orbital. Specifically, under the chosen kinematics this translates to ejected electron angles of approximately 60°, where the 12a′ state dominates and angles in the region of 120°, where the contributions are thought to be approximately equal (see figure 5.3).

5.4 Angular Distributions

Figures 5.4-6 present the experimental results for the HOMO of tetrahydrofuran in polar coordinates. The experimental data exhibits relatively large error as a result of the small magnitude of the coincidence cross section for the chosen molecular orbitals and electron energies. Since the experimental data is not on an absolute scale, the maximum values were normalized to unity. The data have been fitted with a function of the form:

$$f(\theta_b) = \sum_n a_n P_n(\cos(\theta_b - \alpha)) \tag{5.1}$$

where P_n are the Legendre polynomials. The binary and recoil regions have been fitted separately and it is noted that the fit has no physical meaning and is solely to enable better visualisation of the distributions. The same approach has previously been utilised by Avaldi *et al.* [27] and Cavanagh *et al*. [36]. Table 5.2 details the value of the symmetry angles for the binary and recoil regions determined from the fit, α_{bin} and α_{rec}, respectively, n_{max} the highest order Legendre polynomial used in each fit and the direction of the momentum transfer.

The data presented in figure 5.4 is for a scattering angle of -5°, and it is evident from the relative size of the peaks in the binary and recoil regions that there is a large amount of interaction between the ejected electron and the target nucleus under the selected kinematic arrangement. The data exhibits a local minimum very close to the momentum transfer direction in both binary and recoil lobes, and although the Legendre polynomial fit does not follow the clear dip in the experimental data, the symmetry angle from the fit α_{bin} (see table 5.2) coincides almost exactly with the momentum transfer direction θ_{κ}.

At a slightly larger scattering angle of -10°, the TDCS presented in figure 5.5 exhibits a broader binary peak, again with a local minimum near the momentum transfer direction. This minimum appears deeper than in figure 5.4, however the scatter on the experimental data in this region is quite large, making it difficult to conclude whether this minimum is in fact deeper or possibly shallower than in the -5° case. The ratio of binary intensity to recoil intensity is much greater than for the -5° scattering angle case, likely due to the kinematics for

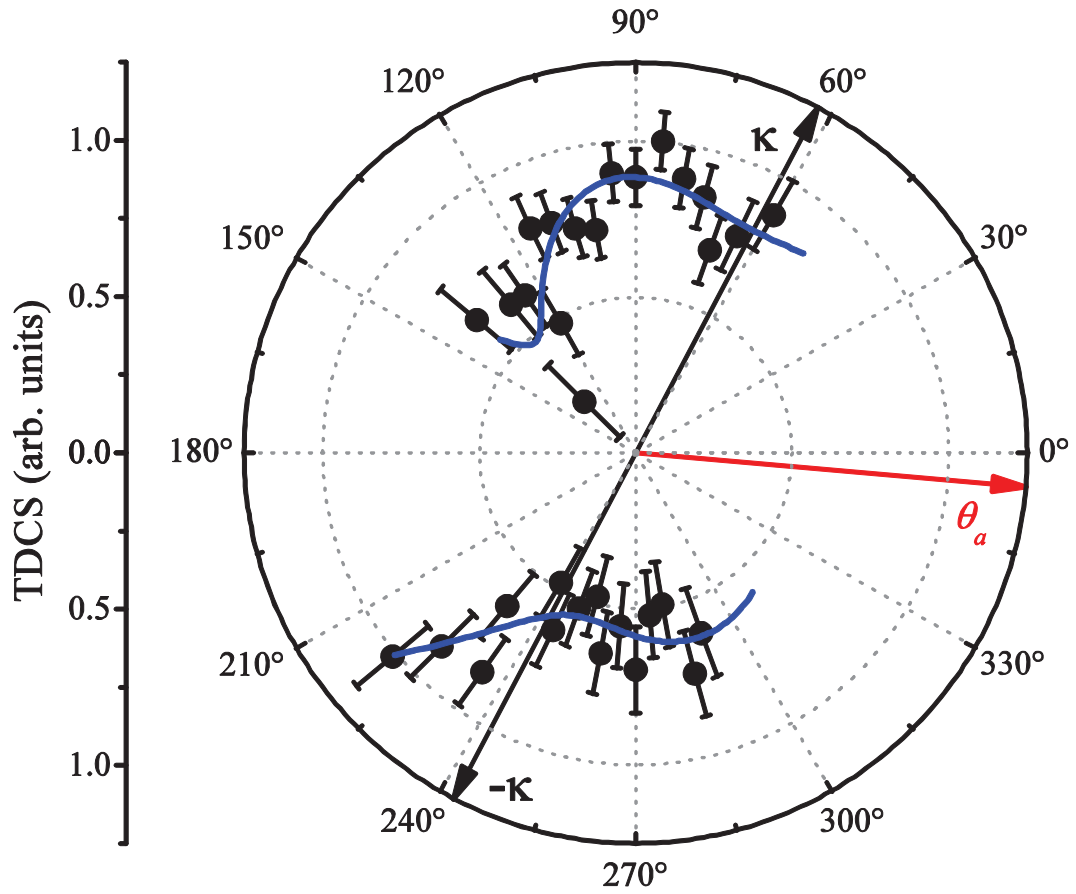

Figure 5.4: Polar plot of the triple differential cross section for the HOMO (12a′+9b) of THF (solid black circles), with E_0=250 eV, E_b=10 eV, θ_a=-5° and $|\boldsymbol{\kappa}|$=0.40 au. The solid blue line is a fit of equation 5.1 to the data.

θ_a	n_{max}	α_{bin}	θ_κ	n_{max}	α_{rec}	$\theta_{-\kappa}$
-5	3	62.5	62.3	2	289.2	242.3
-10	2	88.5	70.5	3	236.2	250.5
-15	2	85.7	73.6	3	244.4	253.6

Table 5.2: Values of the symmetry angles α_{bin} and α_{rec} (in degrees) for fits of equation 5.1 to the binary and recoil regions, respectively, of the experimental (e, 2e) cross sections for the ionization of the combined outermost valence orbitals (12a′+9b) of tetrahydrofuran. n_{max} is the highest order polynomial used for each fit while θ_κ and $\theta_{-\kappa}$ represent the direction of the momentum transfer vector, $\boldsymbol{\kappa}$ (in degrees), for each case.

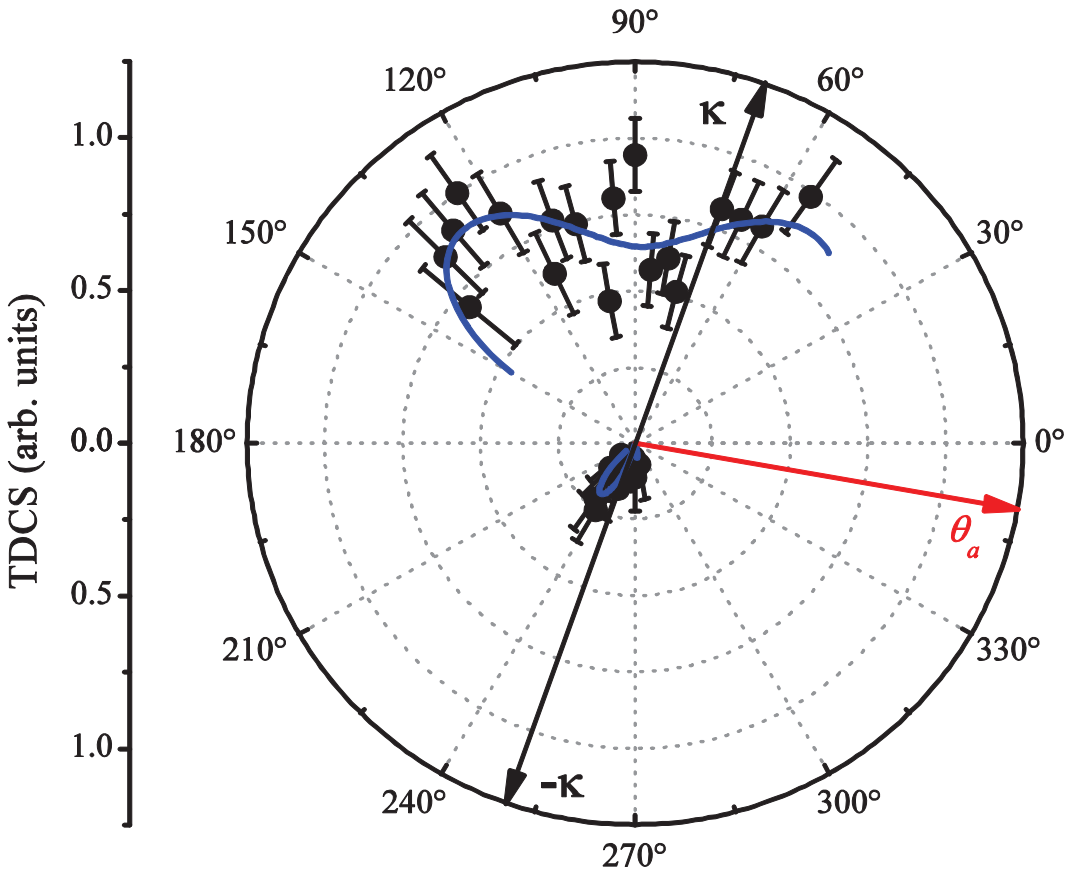

Figure 5.5: Same as figure 5.4, except that θ_a=-10° and $|\boldsymbol{\kappa}|$=0.75 au.

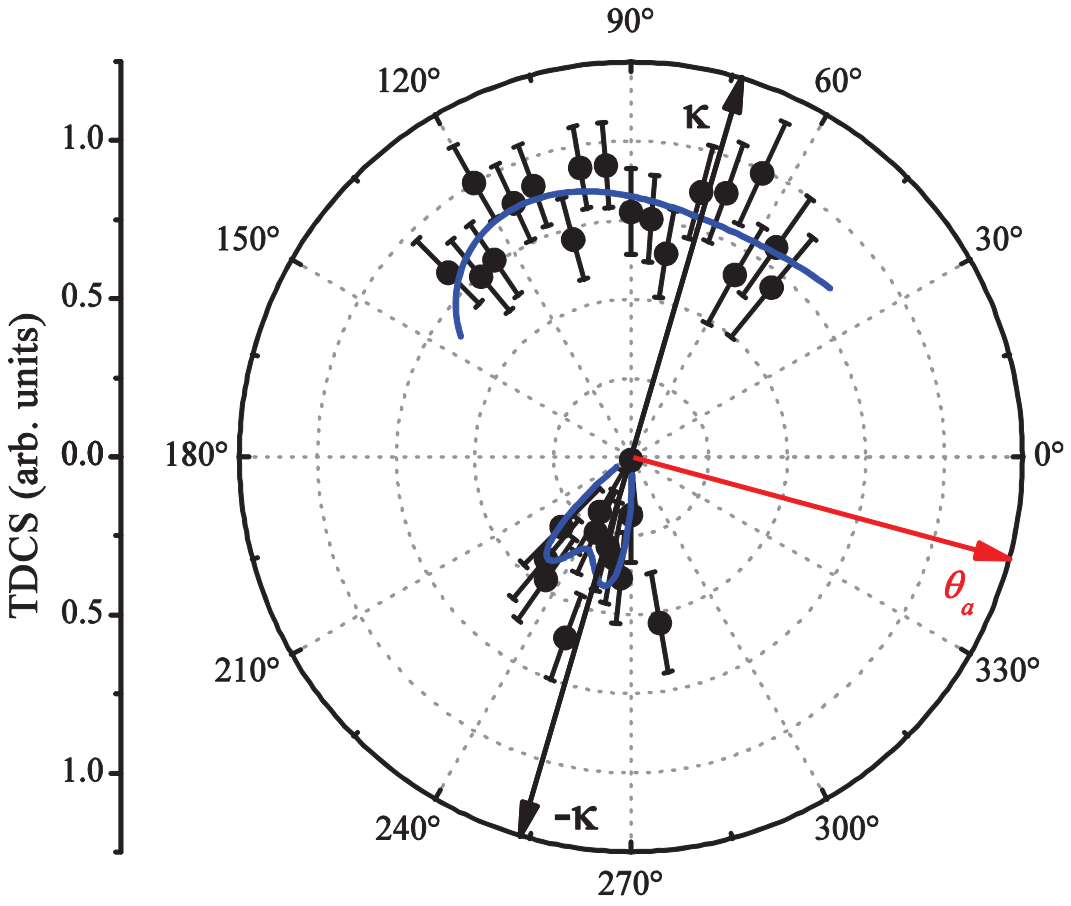

Figure 5.6: Same as figure 5.4, except that θ_a=-15° and $|\boldsymbol{\kappa}|$=1.11 au.

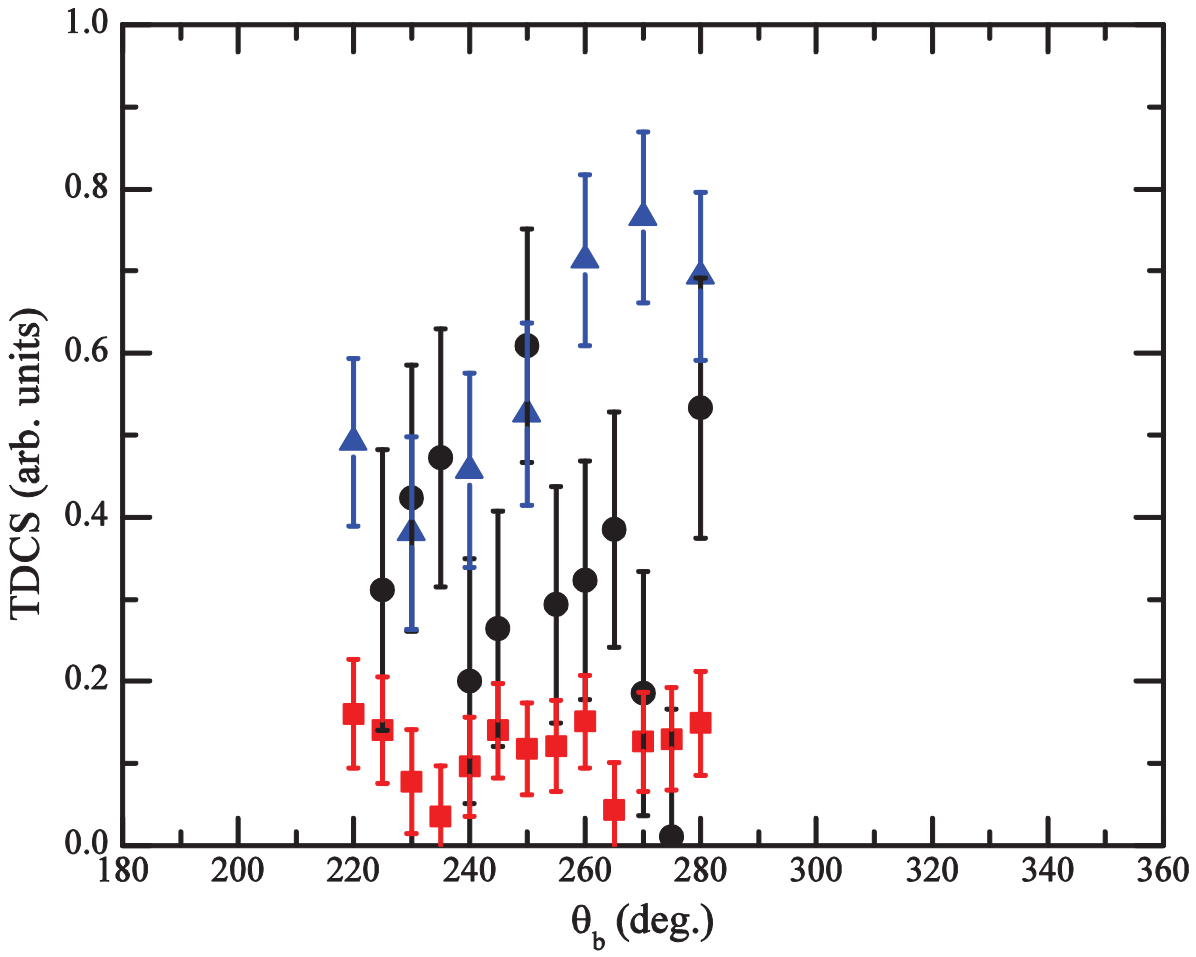

Figure 5.7: Comparison of the relative size of the recoil peaks for THF (black circles), formic acid (red squares) and water (blue triangles), with E_0=250 eV, E_b=10 eV and θ_a=-15°. The binary peak maxima of the TDCSs have been normalised to unity, thus the magnitude of the recoil peak is indicative of its relative size to the binary peak.

the -10° scattering angle arrangement being quite close to bound Bethe ridge conditions. On the bound Bethe ridge the kinematics satisfy the condition that during the collision all of the momentum transferred is transferred to the bound target electron. Under such conditions, the collision kinematics correspond to a binary electron-electron collision, where the ion plays no role, and practically no recoil lobe is expected [90].

For the case of -15°, the largest scattered electron angle presented here, the binary lobe of the TDCS is again very broad, effectively isotropic within the error of the experiment. The relative size of the recoil peak is also small. This finding is similar to the conclusions of the previous study on formic acid [41], where the size of the recoil peak relative to the binary peak decreased greatly as the scattering angle was increased and was found to be significantly smaller than for water under the same kinematics (see figure 5.7 for a comparison of the recoil peaks for each molecule). It was suggested that this trend is due to the location of the

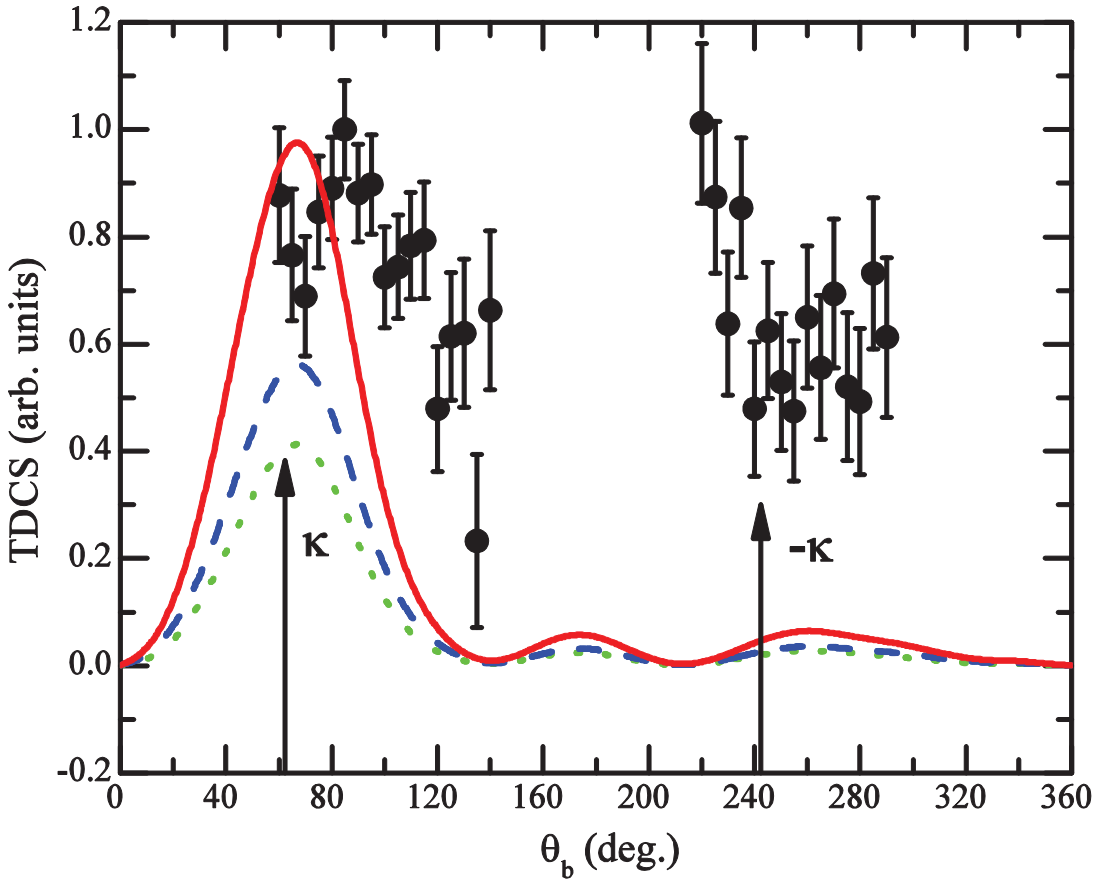

Figure 5.8: Experimental triple differential cross sections for the HOMO (12a′+9b) of THF (solid black circles), with E_0=250 eV, E_b=10 eV, θ_a=-5° and $|\boldsymbol{\kappa}|$=0.40 au, compared with the M3DW calculation for the 12a′ orbital (dashed blue line), the 9b orbital (dotted green line) and the sum of the individual orbitals (solid red line).

molecules' centre of mass, which in the cases of both formic acid and tetrahydrofuran is quite some distance from a nuclear charge centre. Building upon arguments presented in Al-Hagan *et al.* [139] it was postulated that the lack of nuclear charge at the centre-of-mass results in decreased recoil scattering for larger incident electron scattering angles.

It is difficult to discern a clear minimum in the experimental binary peak for this case, although the symmetry angle determined from the Legendre polynomial fit is close to the momentum transfer direction. In figure 5.4 and figure 5.5 the symmetry angle determined from the fits is observed to be close to the minima in the experimental cross section. This suggests that the THF cross sections potentially have a double lobe structure in the binary region, and is symmetric close to the momentum transfer direction. As the momentum transfer is increased when the scattered electron angle is increased, the kinematic conditions for scattering angles of -5°, -10° and -15° correspond to being below, on and above the bound Bethe ridge. The double lobe structure appears below the bound Bethe ridge, possibly becomes more pronounced on the Bethe ridge, and then becomes barely discernable above the

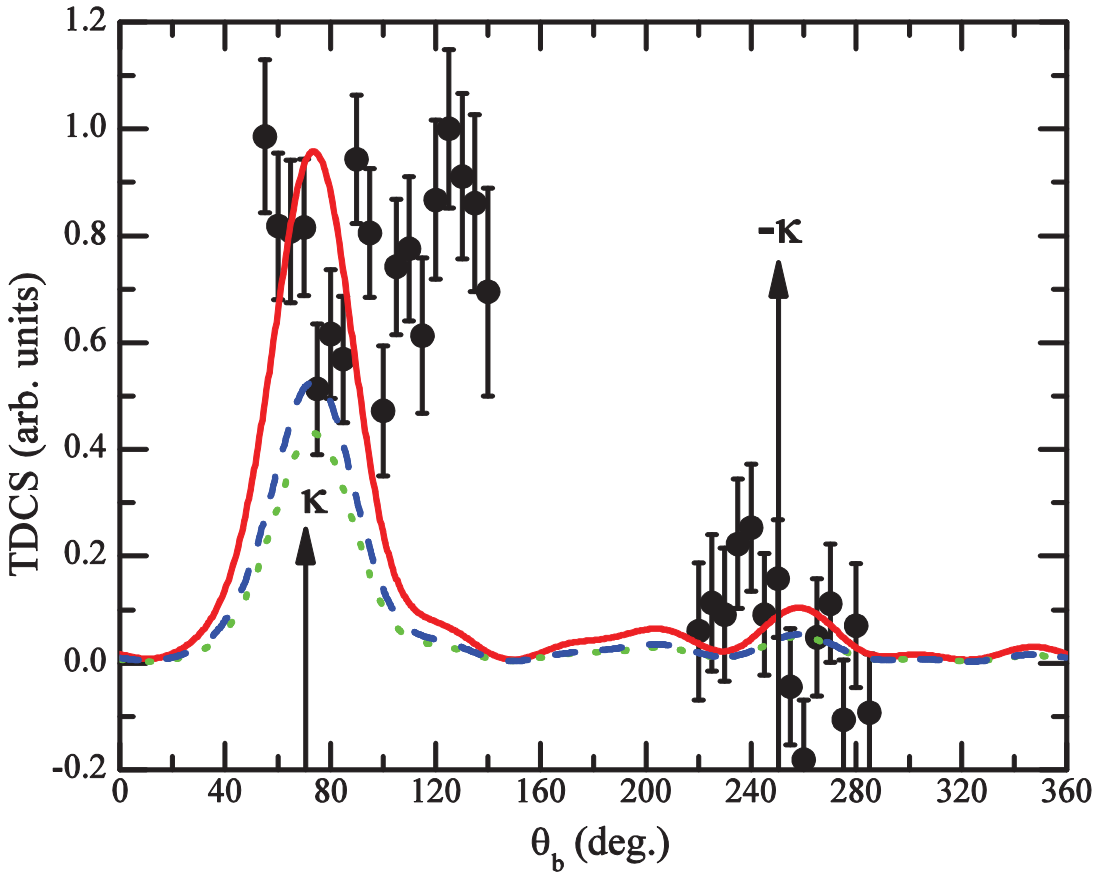

Figure 5.9: Same as figure 5.8, except that θ_a=-10° and $|\boldsymbol{\kappa}|$=0.75 au.

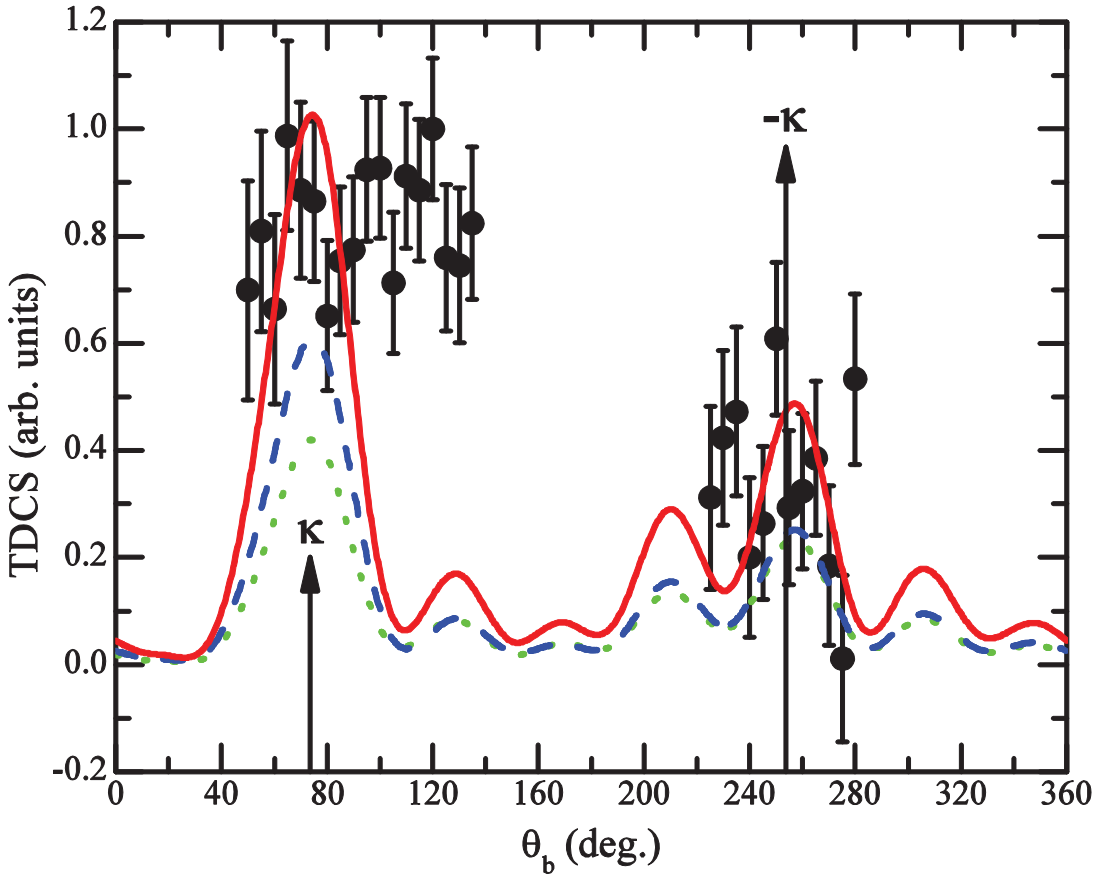

Figure 5.10: Same as figure 5.8, except that θ_a=-15° and $|\boldsymbol{\kappa}|$=1.11 au.

bound Bethe ridge at -15°. Double binary peak structures have previously been observed for ionization of atomic p-states, so it is expected that this may be indicative of contributions to the cross section from the atomic oxygen 2p state [156].

Figures 5.8-10 compare the present results with the molecular 3-body distorted wave (M3DW) theoretical calculations. The experimental cross sections represent an average over all molecular orientations and the M3DW calculations have approximated this average using the orientation averaged molecular orbital (OAMO) approximation. This approximation works very well for highly symmetric molecular states, however the OAMO is zero for the 9b and 12a′ states of THF due to antisymmetric cancellations of different regions of space. To avoid these cancellations, the absolute value of the wave function was averaged rather than the actual wave function [42]. It is seen that the M3DW for all scattering angles predicts a binary peak very close to the momentum transfer direction, for both the 9b and 12a′ states. This means that the sum (with each orbital assigned equal weight) also has a peak for this direction where the experiment observes a minimum in the cross section. As mentioned above, atomic cross sections for p-states have been found to have a double binary peak with a minimum near the momentum transfer direction. Assuming that this split peak originates from the 2p nature of the molecular state, the M3DW would not be able to reproduce this feature of the data as the OAMO automatically produces an s-orbital type angular dependence, meaning that the cross sections will always have a binary peak near the momentum transfer direction, regardless of the shape of the orbital under investigation.

Figure 5.8 compares the present experimental data with the M3DW calculations for both orbitals. Given that the different orbitals show no variation to the calculated cross sections with respect to their shapes, it is not possible to identify contributions from the individual orbitals. PCI causes a slight shift of the binary peak to larger ejected electron angles consistent with symmetry angle listed in table 5.2. The M3DW grossly underestimates the size of the recoil peak in the experimental cross section. Tóth and Nagy [55] recently published a similar DWBA calculation for electron ionization of CH_4 which also struggled to predict the correct magnitude of the recoil peak. If PCI is neglected in the wave function of the final state, the M3DW effectively reduces to the DWBA calculation. Tóth and Nagy demonstrated the strength of the nuclear term in the static potential is related to the recoil peak magnitude, and attributed their underestimation of the recoil peak to a nuclear interaction that is too weak, due to the spreading of the nuclear charge over a spherical shell.

The M3DW calculation at a scattered electron angle of -10° (figure 5.9) predicts the size of the recoil peak correctly, however the experimental shift of the symmetry angle from the momentum transfer is much greater than the M3DW predicts. Presented in figure 5.10, the

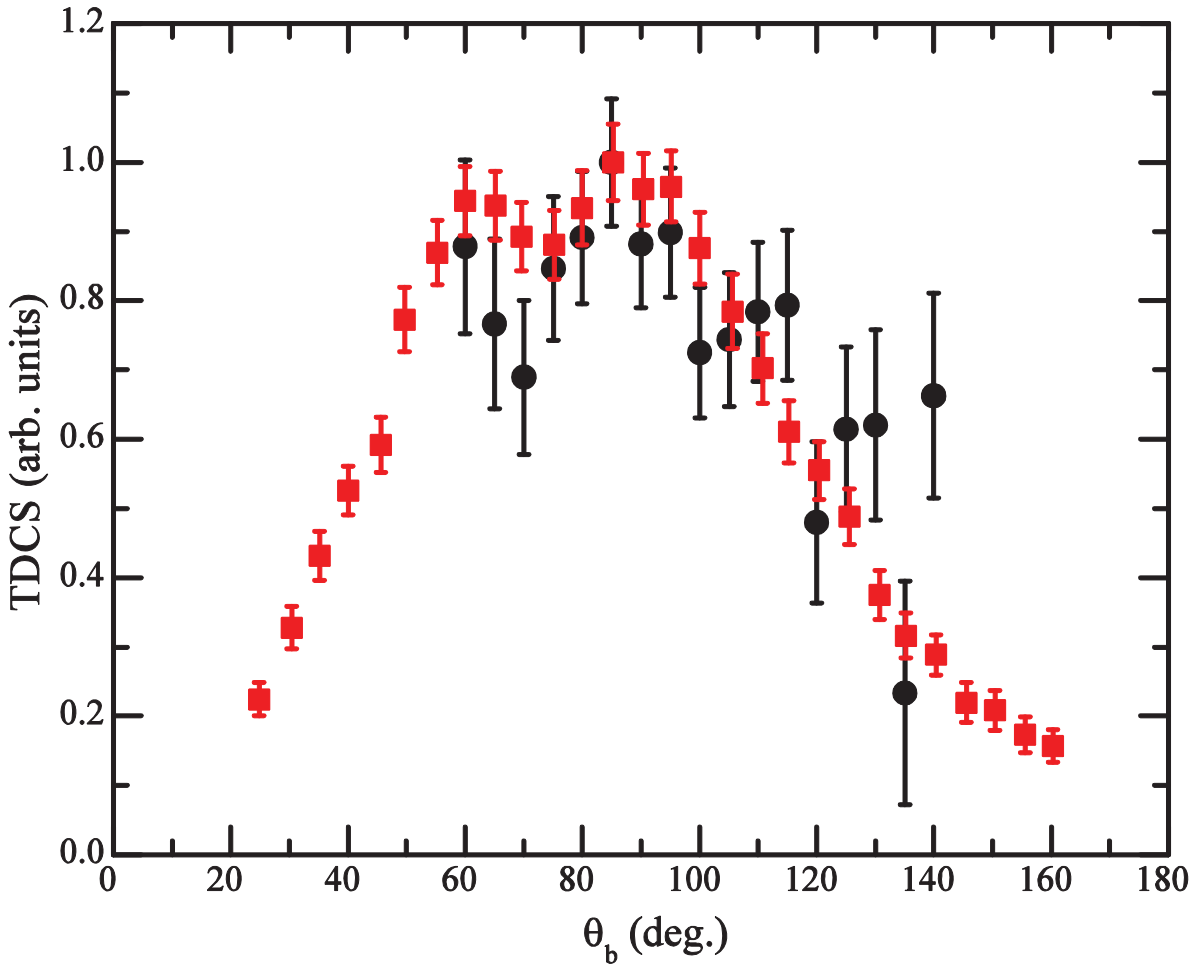

Figure 5.11: Comparison of experimental TDCSs for ionization from the HOMO of THF (solid black circles), with E_0=250 eV, E_b=10 eV, θ_a=-5°, and ionization from the HOMO of methane [40] (solid red squares), under different kinematics of E_0=526.2 eV, E_b=12 eV, θ_a=-6°.

-15° scattering angle case is very similar in that the recoil peak magnitude is correctly predicted but the shift of the symmetry angle from the momentum transfer direction is again underestimated. The M3DW appears to be more successful in predicting the relative height of the recoil peak for larger scattered electron angles, which correspond to smaller impact parameter collisions. The weakening of the nuclear interaction reported by Tóth and Nagy is evidently more important for large impact parameters than for small, however it is difficult to see why back scattering should be more important for electrons that are further away from the target nucleus.

According to the calculated M3DW cross sections for each case, and as predicted by Ning *et al.* [150] and Duffy *et al.* [155], the 12a′ state seems to dominate the 9b state in the binary peak region near 60° while above 120° the two states make approximately equal contributions, although this is likely fortuitous given that most of the initial state information of the molecular orbital is lost. Broad binary peaks have been observed for the HOMO of

other molecules. Figure 5.11 presents a comparison between the current measurement for the HOMO of THF at θ_a=-5° to the recent study of Lahmam-Bennani *et al.* [40] on methane ($1t_2$), albeit under slightly different kinematics. Very broad binary regions appear to be typical of (e, 2e) studies on the HOMOs of molecules, regardless of the shape of these orbitals. It is expected that this is a result of the delocalisation of these orbitals across the entire molecule.

The Pyrimidine Bases

6.1 Introduction

DNA (or deoxyribose nucleic acid) contains the genetic instructions that are necessary for the development and function of most living organisms. Its main role is the storage of information, often likened to a blueprint as it contains the instructions to construct other components of cells, such as proteins. DNA consists of two long polymer chains, made of phosphate groups and 2-deoxyribose sugars, for which THF is a good analogue, joined together by ester bonds (see figure 6.1). Attached to the sugar groups is one of four molecules, adenine, cytosine, guanine or thymine, termed bases. It is the sequence of these bases along the DNA backbone that is responsible for the encoding of information. The double helix is stabilised via hydrogen bonding, with each base having just one complimentary base with which to form these bonds. Within the structure of cells, DNA is organised into long structures known as chromosomes, which are duplicated before a cell undergoes division. The majority of a cell's DNA is stored in the nucleus, however some is stored in organelles, such as mitochondria.

Due to the difficult nature of reliable measurement or calculation of cross section data for electron scattering from large molecules, there is limited information on species of biological interest. In contrast, there is great interest in this information as inputs for the study of the biological effects of radiation via Monte Carlo simulation. Experimentally, elastic differential cross sections (DCS) for electron scattering from water have been around for some time [59], while data has recently appeared concerning formic acid [61], as well as variations of the tetrahydrofuran ring [80, 157], alanine [158] and pyrimidine [159]. Unusually, due to the difficulties in handling these sorts of targets, theoretical calculations for the large biomolecules are preceding experimental study. Theoretical studies concerning electron scattering from the DNA bases have been performed by Możejko and Sanche [160]

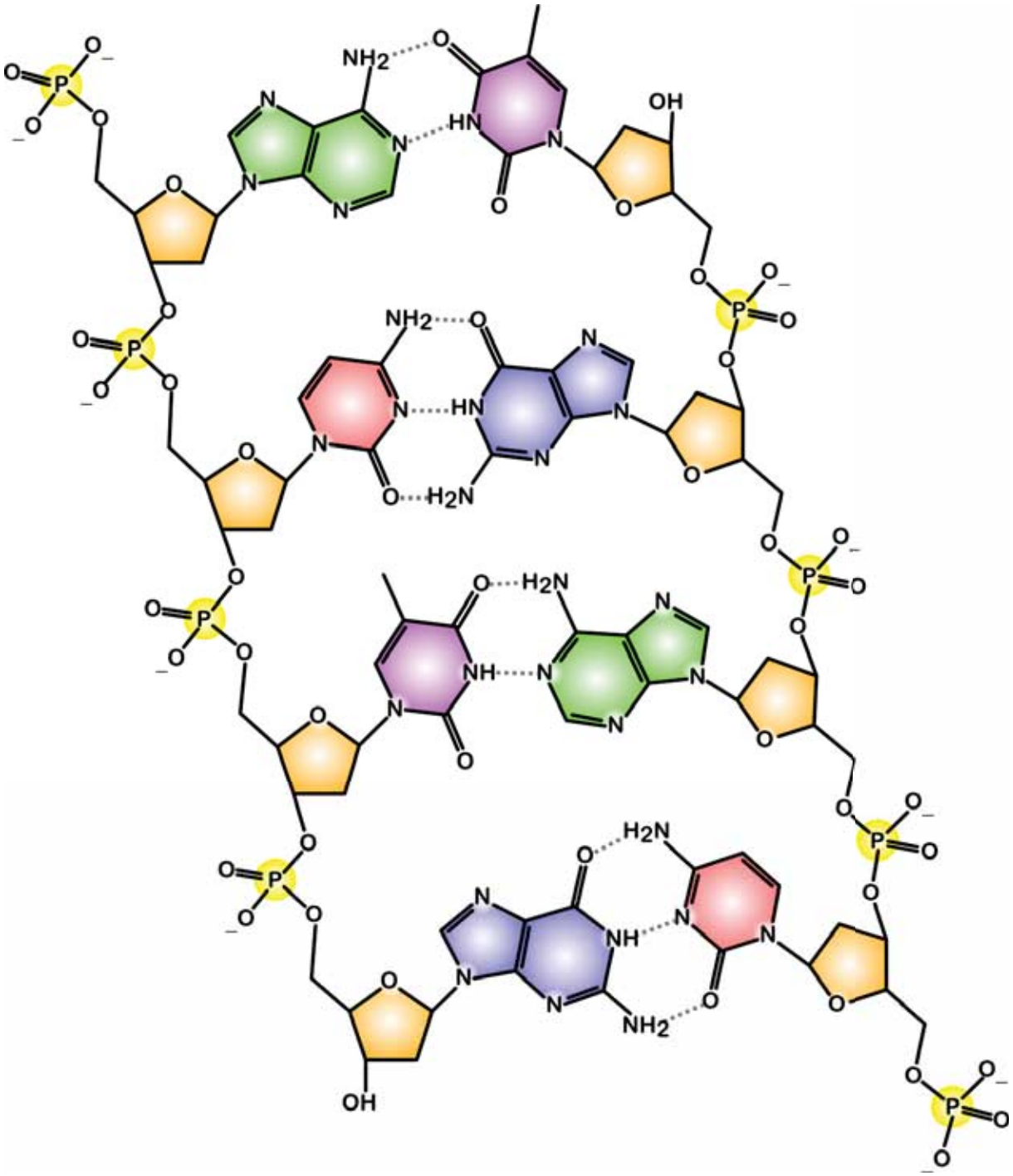

Figure 6.1: The structure of part of a DNA double helix. The individual components are the phosphate groups (yellow) and 2-deoxyribose (orange), as well as the nucleobases, adenine (green), cytosine (red), guanine (blue) and thymine (purple). Adenine and thymine always pair together, likewise cytosine and guanine, and pairing is achieved via hydrogen bonding. Image obtained from [161].

and Blanco and García [162-163], who have calculated elastic cross sections for all of the DNA bases, differential in energy as well as in angle. An interesting outcome of both of these studies was the realisation that the angular distribution at a given energy for any one of the DNA bases can be related quite accurately to the others by the ratio of their molecular weights or the number of electrons in the target. Owing to the difficulty of preparing a gaseous target

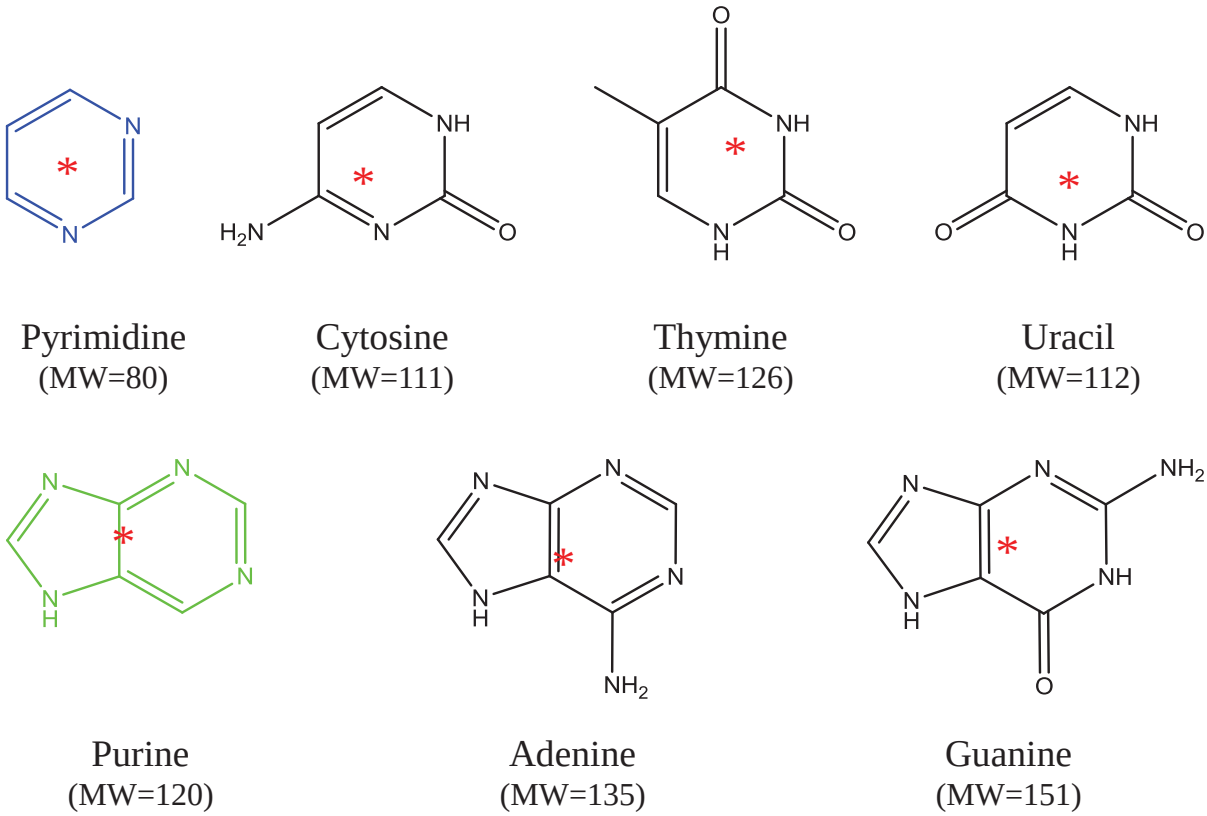

Figure 6.2: Chemical structure of the pyrimidine molecule (shown in blue) and the pyrimidine nucleobases, cytosine, thymine and uracil and the chemical structure of the purine molecule (shown in green) and the associated purine nucleobases, adenine and guanine. The molecular weights are given in mol. and the centre of mass for each molecule is denoted by a red asterisk.

of the DNA bases, electron momentum density probability distributions do not currently exist. However, there has been EMS data published recently by Ning *et al.* [164] for pyrimidine, indicating that there is an interest from the scientific community in momentum density distributions of the nucleobases.

The present study reports the first experimental cross sections for the elastic scattering of electrons from two of the DNA bases, cytosine and thymine. Angular distributions have been measured for a number of energies between 60 and 500 eV, and for angles between 15° and 130°. Theoretical cross sections calculated by the screen-correction additivity rule (SCAR) method by Blanco and García [163] are also presented for cytosine and thymine under the same conditions. In the SCAR calculation the atoms constituting the DNA bases are individually represented by an interacting complex potential, whose real part accounts for the elastic scattering of the incident electrons while the imaginary part represents the inelastic processes, and are constructed using the procedure of Staszewska *et al.* [165]. Subsequent improvements to the complex potential were made by a physical formulation for the absorption potential [166], through the inclusion of screening effects and advancements in the

description of the electron's indistinguishability [167]. The molecular scattering amplitude is then derived from the sum of all the relevant atomic amplitudes, with consideration of the molecular structure by the inclusion of some screening coefficients [168], yielding the molecular differential cross sections. The measured elastic cross sections are relative, and are only attributed an absolute scale by comparison to theory. Comparison is made with the existing theoretical results by Możejko and Sanche [160]. Due to the structural similarities between the two DNA bases and pyrimidine (see figure 6.2), cross sections are also compared to the previous experimental study of Maljković *et al.* [159].

6.2 Physical Characteristics

The DNA bases can be classified into two different types: adenine and guanine are termed purine bases as their chemical structures are an extension of the purine molecule, similarly cytosine and thymine are called pyrimidine bases (figure 6.2). There is a fifth base, a pyrimidine base called uracil, which takes the place of thymine in ribose nucleic acid (RNA), and differs from thymine by lacking the methyl group on its ring. From here on, only the pyrimidine bases cytosine and thymine shall be considered further.

Cytosine, systematically known as 4-aminopyrimidin-2(1H)-one, is a pyrimidine derivative ($C_4H_5N_3O$) (see figure 6.2). Under standard conditions it is a white powder, with a decomposition temperature of 320-325°C. Cytosine has a very large dipole moment of 7.19 Debye [169] while its molar mass is 111.1 $gmol^{-1}$ [125]. Thymine, systematically named 5-methylpyrimidine-2, 4(1H, 3H)-dione, is also a pyrimidine derivative ($C_5H_6N_2O_2$) (see figure 6.2). It too exists as a white powder under standard conditions, with a melting point between 316-317°C, and a decomposition temperature slightly higher at 335°C. Thymine has a dipole moment of 4.93 Debye [169] and its molar mass is 126.1 $gmol^{-1}$ [125].

The pyrimidine base targets are converted to their gaseous state via heating in a molecular oven (see section 3.2.2 for more detail). Both targets are solid powders at room temperature and are of stated purity greater than 99% (Sigma-Aldrich, Australia). The temperature required to achieve a gas density great enough to enable measurement is dependent on the target in question. Figure 6.3 shows the vapour pressure of each of the nucleobases as a function of temperature. Due to their radically different vapour pressures, the molecular oven was heated to 135°C and 225°C to produce good signal during measurement of thymine and cytosine respectively. The targets are then trapped via a LN_2 filled cold finger as detailed previously.

The elastic differential cross sections are measured via the crossed beam method. Electrons from a source are crossed perpendicularly with the gas target before being energy

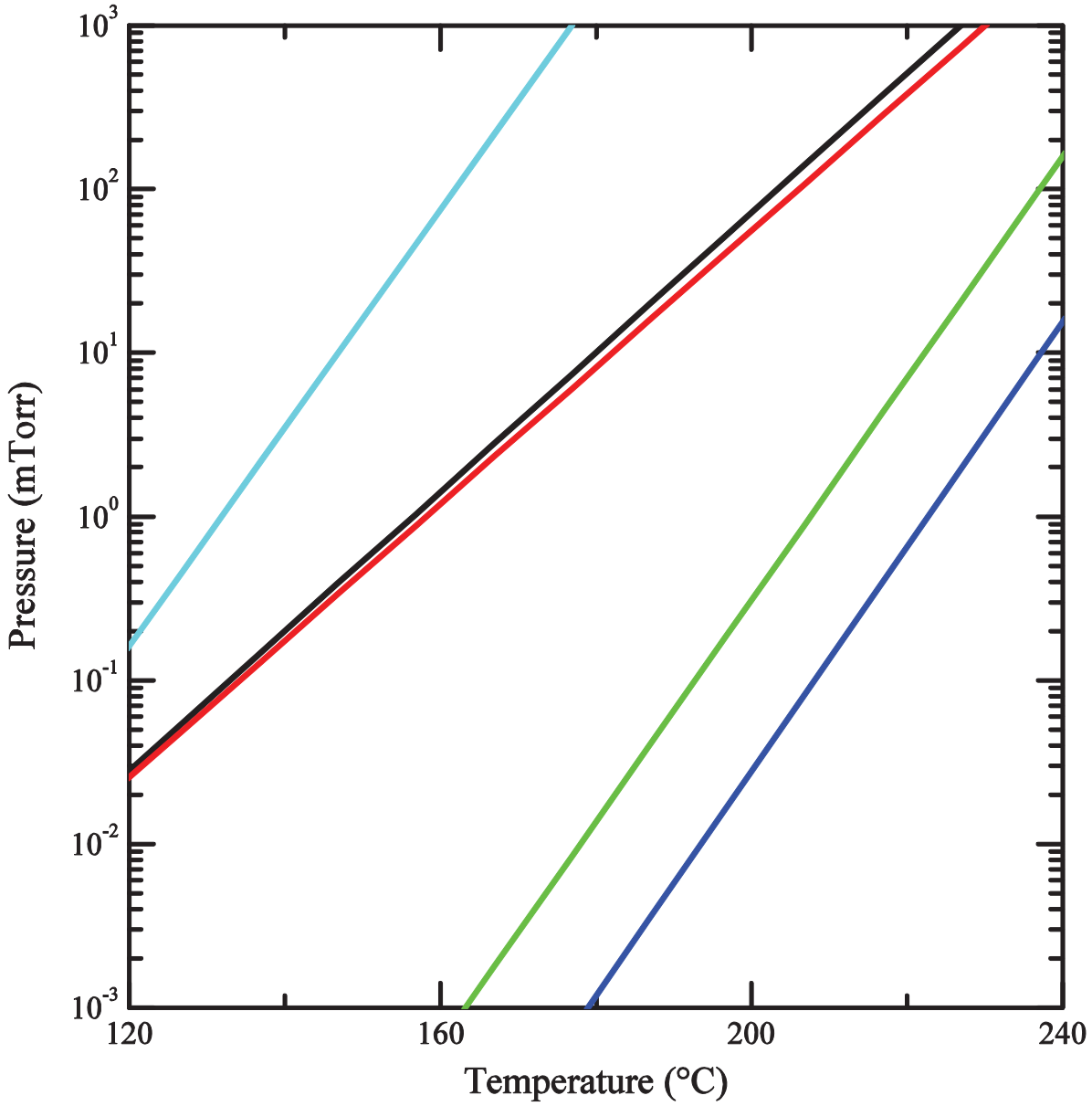

Figure 6.3: Gas pressure of the nucleobases uracil (black), adenine (red), guanine (green), cytosine (blue) and thymine (cyan), as a function of temperature.

selected via a hemispherical analyser and detected by a channel electron multiplier. As elastic collisions involve the detection of only a single particle, the second detector in the (e, 2e) spectrometer was removed for the duration of the study. Angular distributions are measured by varying the in-plane angle of elastic electrons at a fixed energy. As the normal mode of operation for the apparatus is to measure coincident electron ionization, there is no provision in the experiment for the use of the relative flow technique to establish absolute values for the cross sections. As a result, the measured cross sections have achieved absolute scale via normalisation to the corresponding SCAR calculation to give the best visual fit.

Brinkmann and Trajmar [170] showed that it is not sufficient to simply view the region of overlap in crossed beam experiments as, depending on the nature of the molecular

beam forming device, significant volume correction factors may be needed to account for changes in the scattering geometry as a function of the scattering angle. Volume correction factors have not been applied to the elastic differential cross sections presented in this thesis. In the study of Brinkmann and Trajmar [170], it was calculated that for a backing pressure of 0.1 Torr and a source aspect ratio of γ=0.12, a correction factor of 0.8 would be need to be applied to a cross section at a 10° scattering angle with less correction needed as the scattering angle increases. In actuality, the aspect ratio of the system is much smaller at γ=0.03 and backing pressures are likely in the order of 10 mTorr based on the temperatures that the oven was operated and the data presented in figure 6.3. This would result in a smaller number density, a much better collimated beam and consequently less correction would be required due to the tighter confinement [170]. Similarly, based on the low angular resolution of the spectrometer (approximately ±2.5°) and for a very high backing pressure case (10 Torr) a correction factor of 0.8 would again be required at the 10° detection angle. Based on this, correction factors have not been applied to the measured cross sections. It is expected that for the current spectrometer arrangement correction factors between 0.90 and 1 would need to be applied to the SDCS, and less correction would be needed at larger scattering angles.

6.3 Elastic Angular Distributions

Relative DCS's for elastic scattering from cytosine are presented in figure 6.4, for six different incident electron energies, namely 500 eV, 400 eV, 300 eV, 200 eV, 100 eV and 60 eV. The data is presented alongside other available experimental and theoretical cross sections. Relative DCS's for elastic electron scattering from thymine are presented in figure 6.5, for the same incident electron energies as cytosine, except that the 60 eV measurement is omitted due to difficulty obtaining a stable electron beam. Generally, the measured cross sections are very strongly forward peaked, as a result of the large dipole moments of both molecules. A shoulder is observed in the SDCS of both targets, whose location is between 30° and 80° and appears to be correlated with electron energy. The magnitude of the shoulder is seen to be greater for thymine than for cytosine. There is an apparent lack of backward scattering in the measured cross sections for all but the lowest energy cases (100 eV and below).

In figure 6.4, comparison is made between the present cytosine data and the SCAR calculation. Absolute values are assigned to the measured relative cross sections via normalization to the SCAR calculation. Excellent agreement is seen between the calculated and measured data sets, particularly with regard to the depth and location of the minima in the

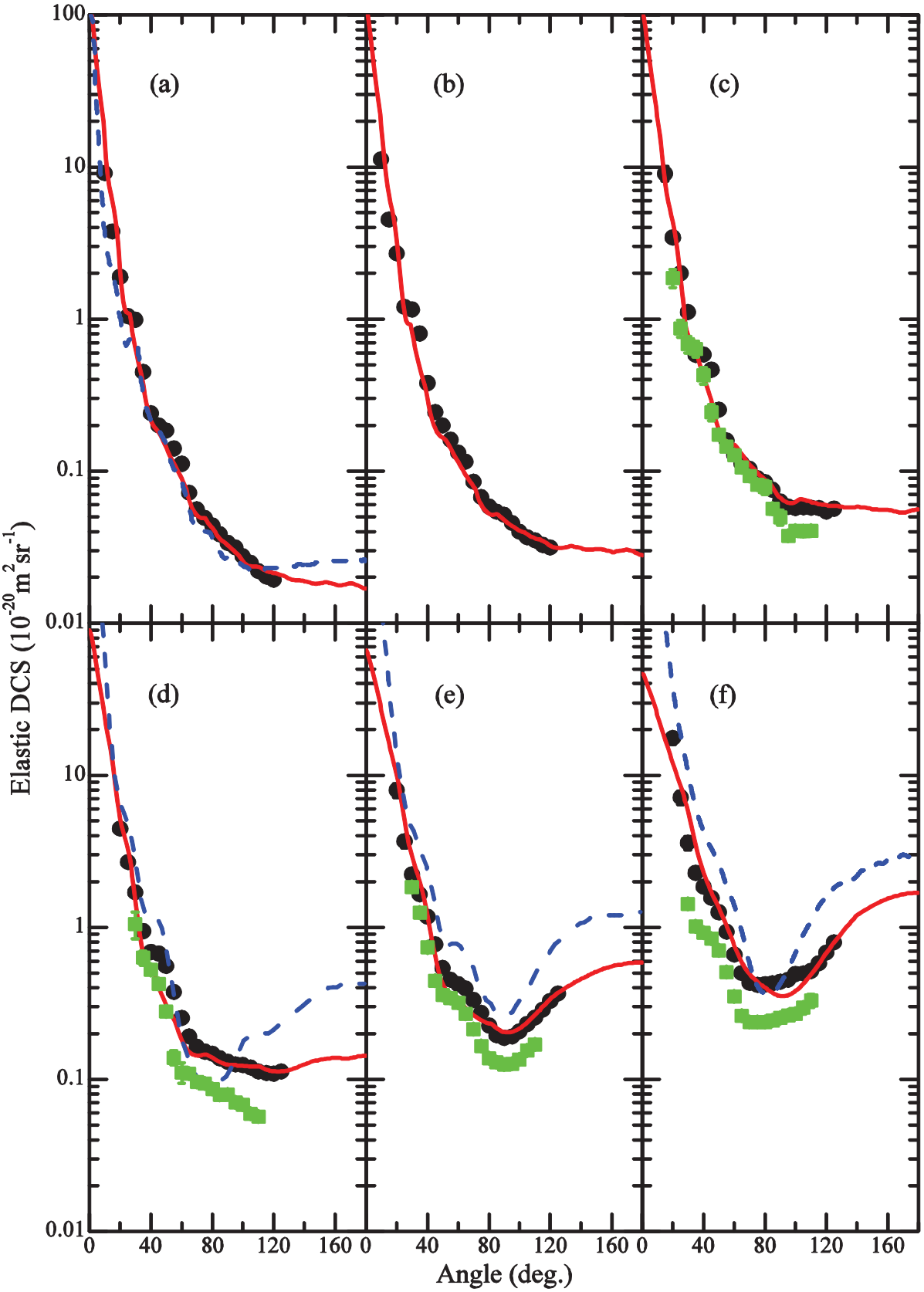

Figure 6.4: Relative DCS for electron scattering from cytosine (circles) at energies of (a) 500 eV, (b) 400 eV, (c) 300 eV, (d) 200 eV, (e) 100 eV and (f) 60 eV. The present data is attributed absolute values via normalisation to the SCAR calculations at the corresponding energy (solid line). Also shown are the IAM calculations [160] (dashed line) and the data for pyrimidine [159] (squares), where available. The statistical error in the present experimental data is less than 10% and less in most cases.

angular distributions. Perhaps the one failing of the SCAR calculation is the underestimation of the slight shoulder in the cross section at approximately 60°, most prominent at 200 eV and 100 eV (panels (d) and (e)). The present data is also compared to the available independent atom method (IAM) calculation of Możejko and Sanche [160], however data is only available for four energies in the presently measured range, namely 500, 200, 100 and 50 eV (panels (a) and (d-f) respectively), with the 50 eV calculation compared to the present measurements at 60 eV. Good agreement is also seen with the IAM calculation, however it tends to overestimate the size of the cross section at backward angles. The IAM results at all available energies overestimate the size of the shoulder at approximately 60°, and predict a strong minimum in the 200 eV cross section which is not observed in the present data. The measured cytosine distributions are finally compared to previous experimental data for pyrimidine of Maljković *et al.* [159] at 300, 200, 100 and 50 eV (panels (c-f)). No internormalisation is used to compare between the cytosine and pyrimidine data. Clearly, the shape of the pyrimidine cross sections and the recently measured cytosine distributions are quite similar. The absolute magnitude of the cytosine cross section, as assigned by the SCAR calculation, is slightly greater than the pyrimidine cross section, particularly around the DCS's minimum, which can likely be attributed to the previously mentioned difference in molecular weight [162].

Figure 6.5 compares the present thymine data with the results of the SCAR calculation, with absolute values attributed to the experimental data via normalization to the theory. The SCAR calculation is again quite successful at reproducing the measured cross sections, however the issue with regards to the underestimation of a shoulder in the cross sections at approximately 60° is again present. It is most evident in the case of 200 eV incident electrons (panel (d)), where the underestimation of the shoulder also appears to flatten the shape of the calculated cross section near 80°, whereas the measured results are gradually decreasing. The thymine data is also compared to the IAM calculation [160], again only available at 500 eV, 200 eV and 100 eV (panels (a), (d) and (e)). Good agreement with the thymine case is also seen for the IAM calculation, however many of the same issues remain. The predicted cross sections are still overestimated at backward angles, and the deep minimum predicted by the IAM calculation at 200 eV does not manifest itself in the measured cross section. However, the IAM results produce the shoulder in the cross sections near 60° with greater accuracy in the case of thymine, particularly with regards to their magnitude, and with remarkable reproduction of the experimental DCS for 100 eV incident electrons with the exception of the overestimation at larger angles. The present data is again compared to the previous experimental cross sections on pyrimidine [159], for 300 eV, 200 eV and 100 eV

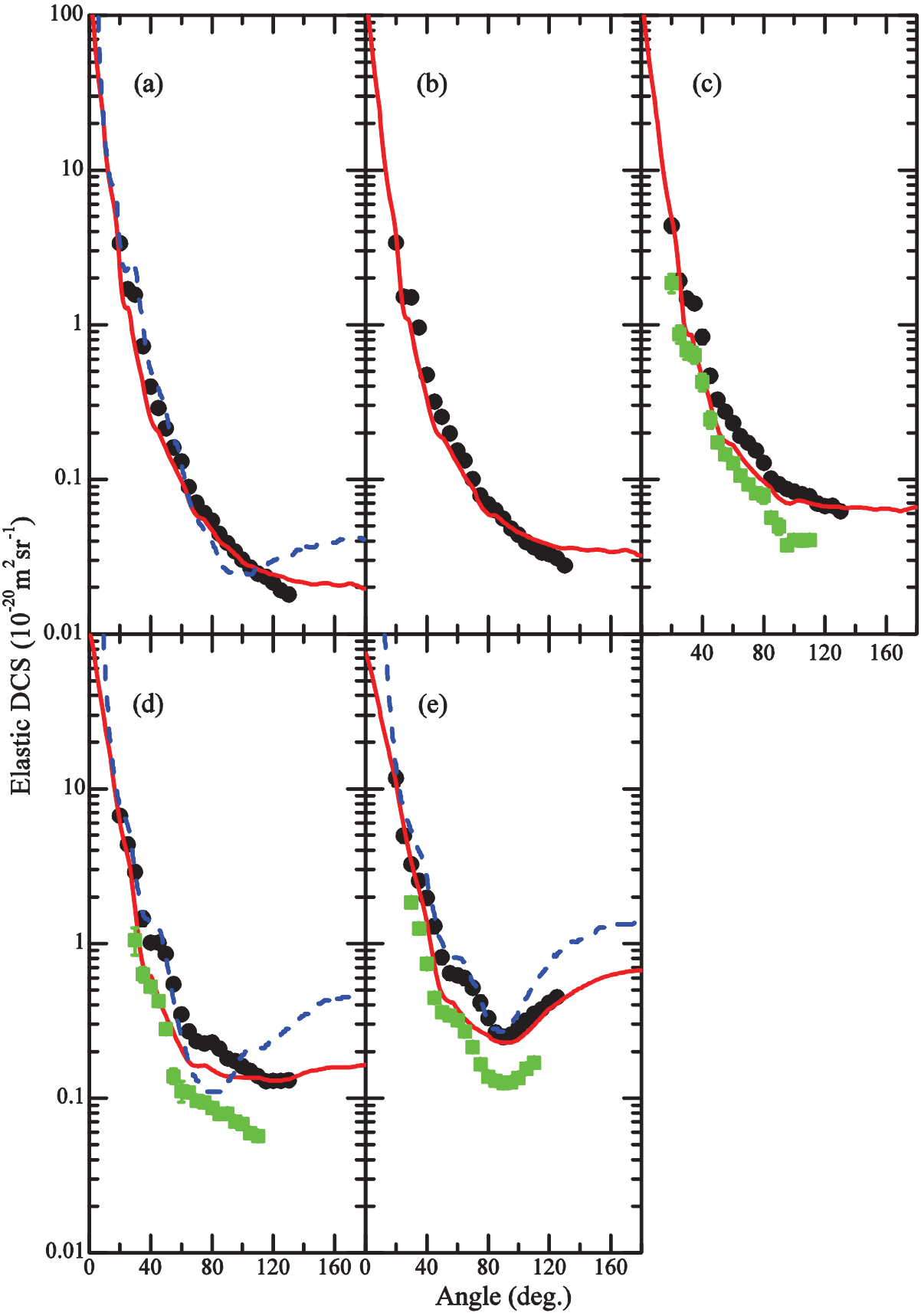

Figure 6.5: Same as for figure 2, but the present experimental data is for thymine and no data is presented for 60 eV.

incident electrons (panels (c-e)). The shape of the presently measured thymine cross sections again correlates quite well with the pyrimidine data, however it is worth noting that the strength of the shoulder at approximately 60° is greater for thymine than for both cytosine and pyrimidine. The absolute magnitude of the thymine cross section, as assigned by the SCAR calculation, is greater than both the cytosine and pyrimidine cross sections, which is expected by its larger molecular weight.

There is a greater difference between the SCAR and IAM calculations for both cytosine and thymine at lower incident energies, as is discussed in detail in Blanco and backward angles. In contrast to the SCAR result of Blanco and García [162], the IAM does not take into account simultaneous interactions of the incident electron with multiple target atoms and ignores geometrical screening corrections for each individual atom from the rest of the molecule. These are incorporated in an approximate way in the SCAR calculations through the screen corrected additivity rule. At larger electron incident energies, atomic cross sections are reported to become smaller and thus the overlapping corrections become smaller, and hence, the inclusion of screening effects becomes less important at higher incident electron energies.

Relative angular distributions of thymine and cytosine are very similar in shape and they also appear similar to the recent experimental cross sections of Maljković *et al.* [159] on pyrimidine. A shoulder in the angular distributions is shown to be present at approximately 60°, and observed to be stronger for thymine than it is for cytosine. This likeness in the angular dependence of DCS values may be expected due to the similarities in the molecular structures of pyrimidine, thymine and cytosine. To obtain a complete picture, and reduce the reliance on the theoretical calculations, absolute elastic SDCSs are needed.

6.4 Binding Energy Spectrum

(e, 2e) measurements have been made for thymine rather than for cytosine, owing to the lower temperature required to produce the molecular beam. A coincidence binding energy spectrum has been collected to confirm the molecular state that is under investigation. Figure 6.6 presents a coincidence binding energy spectrum for the outer valence region of thymine. The incident and ejected electron energies were fixed at 250 eV and 20 eV, respectively, while the scattered electron energy was scanned across a range of energies. The detection angles for the scattered and ejected electrons were chosen to be -10° and 75°, respectively. The fitting of binding energy spectra usually requires the Gaussian widths to be a convolution of the instrumental energy resolution and the natural widths, obtained from photoelectron spectroscopy (PES) data. Unlike formic acid and tetrahydrofuran, where the natural widths of

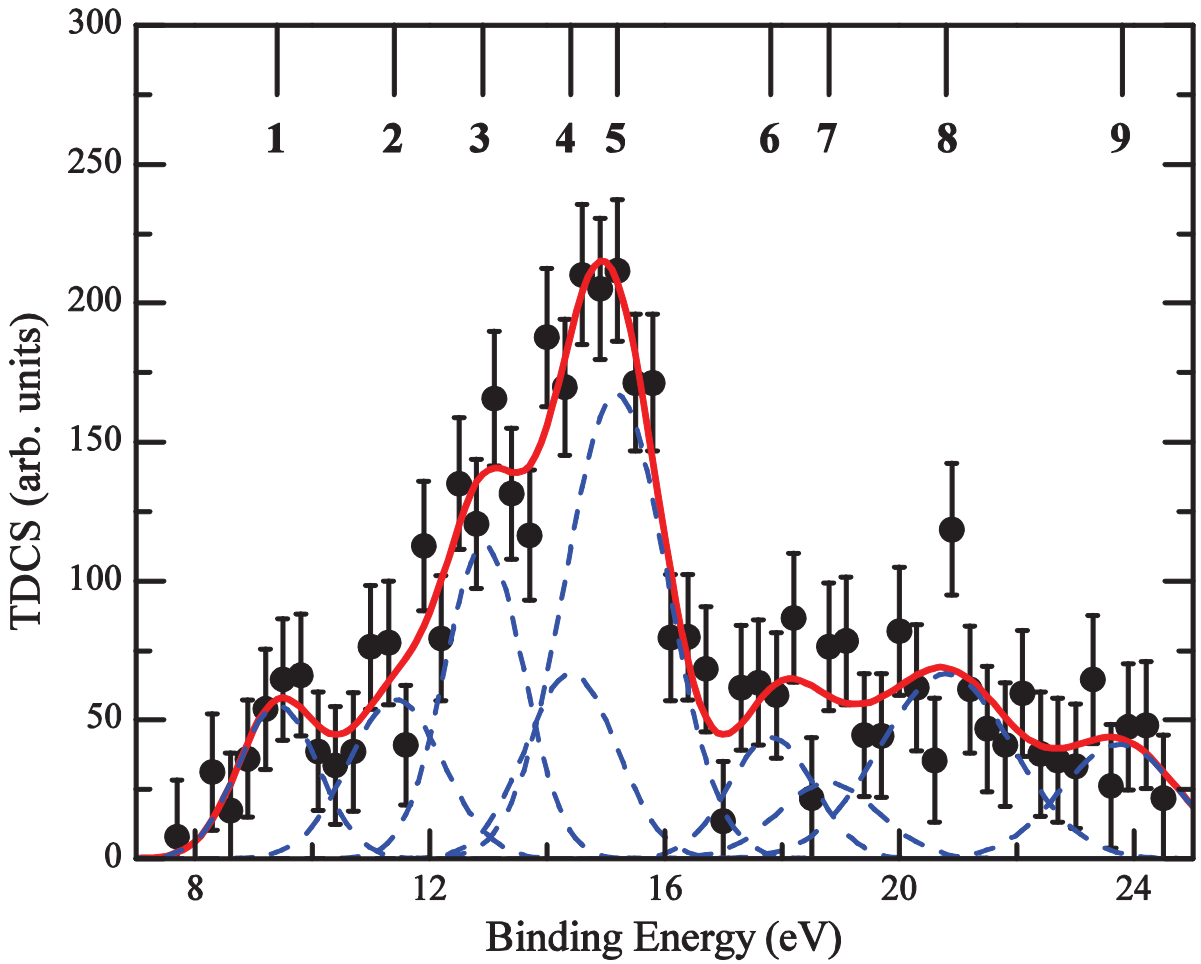

Figure 6.6: The measured binding energy spectrum for the outer valence region of thymine fitted with a sum of Gaussian functions using a convolution of the binding energy resolution and the natural width of the molecular orbitals to define the peak width parameters.

the molecular orbitals were small relative to the experimental (e, 2e) binding energy resolution, the natural widths of the orbitals in thymine are comparable to the binding energy resolution. In this instance, the natural widths and the binding energy resolution were summed in quadrature for each individual peak. Nine Gaussian functions have been used to fit the data, and are labelled as 1 to 9 in figure 6.6.

Similar to formic acid and tetrahydrofuran, thymine has a highly complex valence region that contains many molecular orbitals, and in fact there are nineteen individual orbitals in the 15 eV region that is investigated here. Thymine can also exist as *–cis* and *–trans* conformers, the difference manifesting itself in the rotation of the methyl group that is attached to the hexagonal ring. The differences in orbital ionization energies between the structures are very small, in the order of a few meV, and unlike THF the different conformers do not result in a symmetry change of the molecule. Thus, there is no difference in orbital assignments and momentum profiles for the two conformers of thymine. Presented in table

	Present Results	**FWHM**	**Molecular Orbital [171]**	**Type [171]**	**Theory (OVGF) [171]**	**PES [171]**
1	9.4 (0.6)	1.6	6a″	π_6	8.85	9.2
2	11.4 (0.6)	1.9	5a″	π_5	10.46	10.48
			18a′	$\sigma_{LP\ O}$	10.46	
			17a′	$\sigma_{LP\ O}$	11.36	
3	12.9 (0.6)	1.6	4a″	π_4	12.52	12.25
4	14.4 (0.6)	1.8	16a′	σ	13.92	13.32
			3a″	π_3	13.81	
			15a′	σ	13.83	
			2a″	π_2	14.85	14.87
			14a′	σ	15.02	
5	15.2 (0.6)	2.1	13a′	σ	15.49	15.58
			1a″	π_1	16.08	
			12a′	σ	16.35	
6	17.8 (0.6)	1.7	11a′	σ	17.37	17.93
7	18.8 (0.6)	2.0	10a′			
8	20.8 (0.6)	2.7	9a′			20.85
9	23.8 (0.6)	2.3	8a′			22.09
			7a′			
			6a′			

Table 6.1: Binding energies (in eV) for thymine and the Gaussian peak FWHM (in eV), with the error in the Gaussian peak position quoted in brackets. Orbital assignments, orbital type, OVGF calculations and experimental PES spectra are all taken from Trofimov *et al.* [171].

6.1 are the binding energies (in electron volts) and peak widths for the molecular states of thymine, as well as the assignments, types and energies as determined via the outer valence Green's function (OVFG) method and via experimental PES [171]. Since the binding energy

resolution of the coincidence spectrometer is again large relative to the spacing between the orbitals, individual peaks fitted to the data in figure 6.6 may represent the collective addition of multiple orbitals.

The highest occupied molecular orbital of thymine is the 6a″ state, a combination of π bonds between the individual atoms in thymine, resulting in a molecular orbital that is entirely out-of-plane and delocalised across the entire molecule. The HOMO-1 is the 5a″ state, and is again a delocalised, out-of-plane molecular orbital. The HOMO and HOMO-1 orbitals are separated by 1.8 eV, which indicates that a TDCS measurement of the HOMO orbital would be sufficiently resolved, however there may be small contributions to the resultant TDCS from this overlap. Given that the molecular orbitals measured for formic acid and tetrahydrofuran are also very similar in description, it is expected that the TDCS for this state will have a very broad binary peak. The next two molecular orbitals are closely spaced in energy to the HOMO-1, the 18a′ and 17a′, which are orbitals arising from the lone pairs of electrons on the double bonded oxygen atoms.

The maximum in the binding energy spectrum is at 14.8 eV, where a strong peak is observed that is wider than the binding energy resolution of the experiment. It has been fitted with two separate Gaussian functions and is thought to contain contributions from eight individual molecular orbitals. Based on the energy assignments from the experimental PES spectra [171], it is observed that the nearby 2a″ and 14a′ states will likely be major contributors to the TDCS at this particular energy, although it is difficult to exclude contributions from other nearby states based on the current information.

In this chapter I present triply differential angular cross sections for the ionization of the 2a″+14a′ molecular state of thymine. It was expected that the (e, 2e) cross section for this molecule would be small, as was the case for THF, and that it would be difficult to keep the spectrometer operational with thymine constantly depositing on the electrostatic lens elements. These particular molecular orbitals were chosen because the relative size of this peak is quite large compared to the other orbitals in the binding energy spectrum, to reduce the data collection time. The experiments were performed at a relatively low incident electron energy of 250 eV, for scattered electron detection angles of -10° and -15°, while the ejected electron energy was chosen to be 20 eV. This is opposed to the usual 10 eV, again with a view to improve the collection time by reducing the number of random counts in the ejected channel. Based on the types of orbital designated in table 6.1, it was expected that the contribution to the TDCS from the 14a′ orbital (s-type) would be considerably larger than that of the 2a″ (p-type) at smaller recoil ion momenta. Conversely, at larger recoil ion momenta the contribution from the 2a″ orbital should be greater than the 14a′. Generally, under the

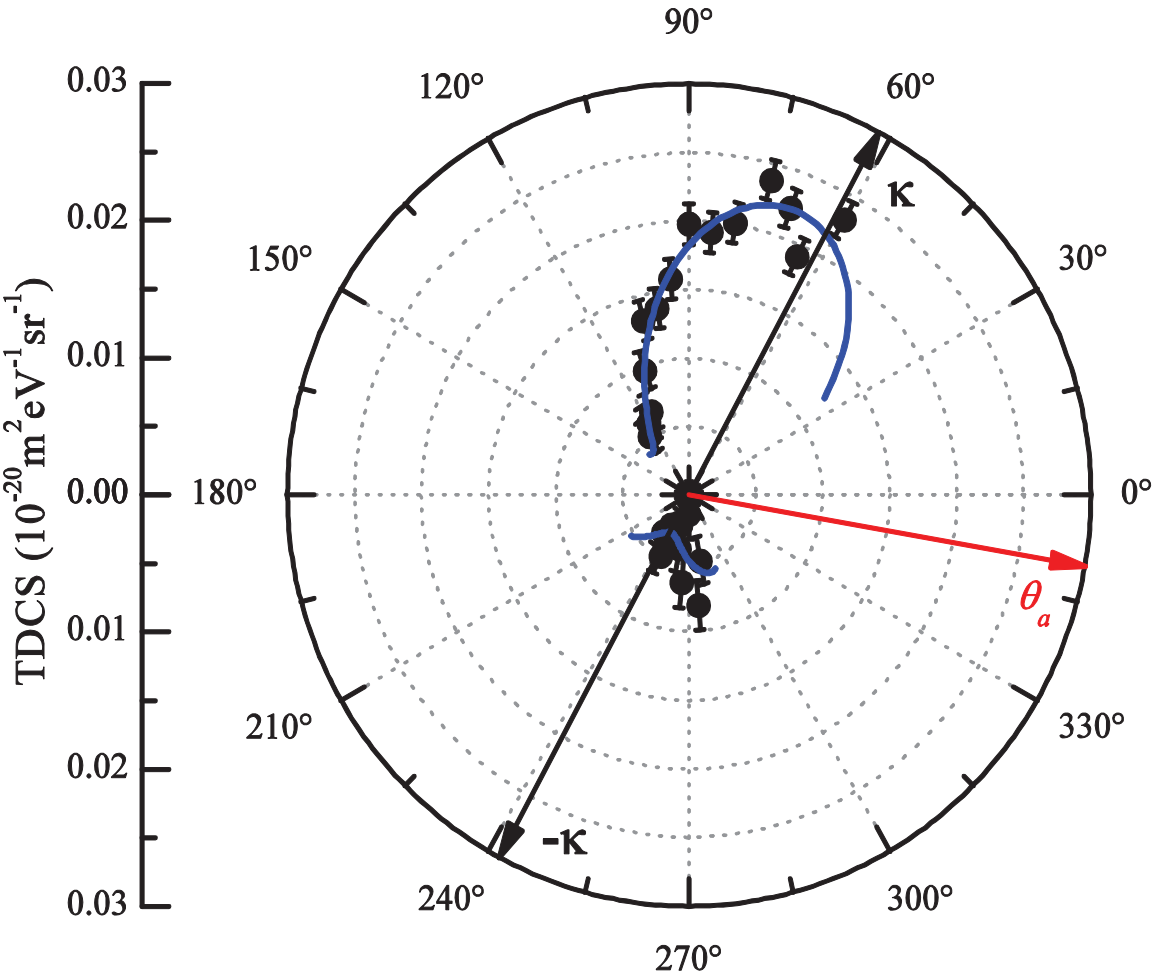

Figure 6.7: Polar plot of the triple differential cross sections for the 2a″+14a′ molecular orbitals of thymine (solid black circles), with E_0=250 eV, E_b=20 eV, θ_a=-10° and $|\boldsymbol{\kappa}|$=0.78 au. The solid blue line is a fit of equation 5.1 to the data.

chosen kinematics this translated to ejected electron angles around the momentum transfer direction where the 14a′ state dominates, while the 2a″ was expected to dominate at the larger ejected electron angles (around 120°).

6.5 Triply Differential Angular Distributions

Figures 6.7 and 6.8 present the experimental results for the combined 2a″ and 14a′ molecular states of thymine. As the experimental data are relative, they have been attributed absolute scale via normalisation of the binary region to a theoretical distorted-wave Born approximation (DWBA) calculation [172], which is discussed in more detail later. The data has been fitted with a sum of Legendre polynomials, as per equation 5.1. The binary and recoil regions have been fitted separately. It is again noted that this fit is to enable better visualization of the distributions and no physical meaning is attributed to the function. Table 6.2 shows the value of the symmetry angles for the binary and recoil regions determined from

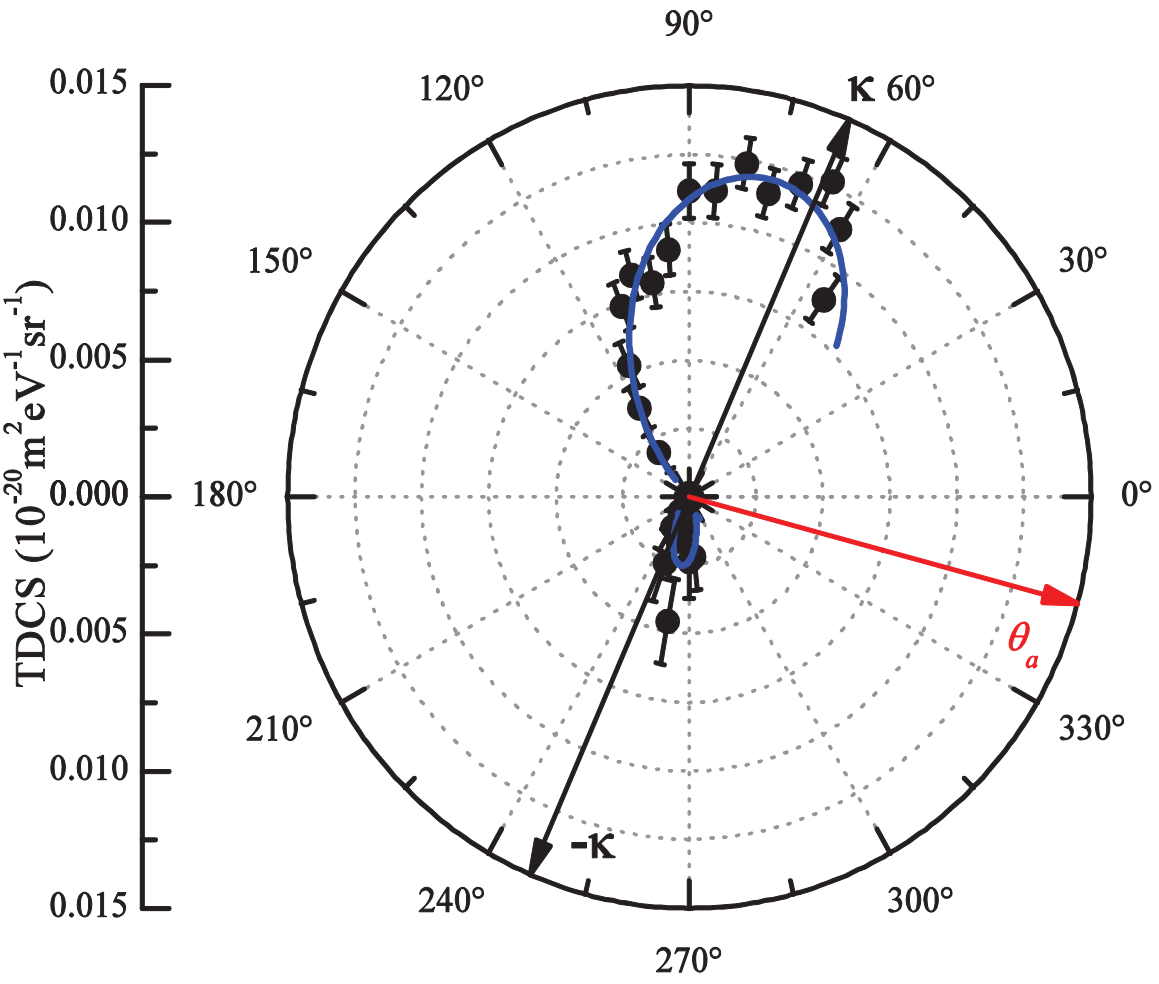

Figure 6.8: Same as figure 6.7, except that θ_a=-15° and $|\boldsymbol{\kappa}|$=1.12 au.

θ_a	n_{max}	α_{bin}	θ_κ	n_{max}	α_{rec}	$\theta_{-\kappa}$
-10	2	69.3	61.8	2	244.7	241.8
-15	2	75.1	66.6	2	263.5	246.6

Table 6.2: Values of the symmetry angles α_{bin} and α_{rec} for fits of equation 5.1 to the binary and recoil regions (in degrees), respectively, of the experimental (e, 2e) cross section for the ionization of the combined 2a″+14a′ orbitals of thymine. n_{max} is the highest order polynomial used for each fit and the angles θ_κ and $\theta_{-\kappa}$ represent the direction of the momentum transfer vector, $\boldsymbol{\kappa}$ (in degrees), in each case.

the fit, α_{bin} and α_{rec}, respectively, n_{max} the highest-order Legendre polynomial used in each fit and the direction of the momentum transfer, $\boldsymbol{\kappa}$.

The data presented in figure 6.7 is for scattered electrons detected at -10°. The TDCS exhibits a single, narrow binary lobe centred about the momentum transfer direction θ_κ, as

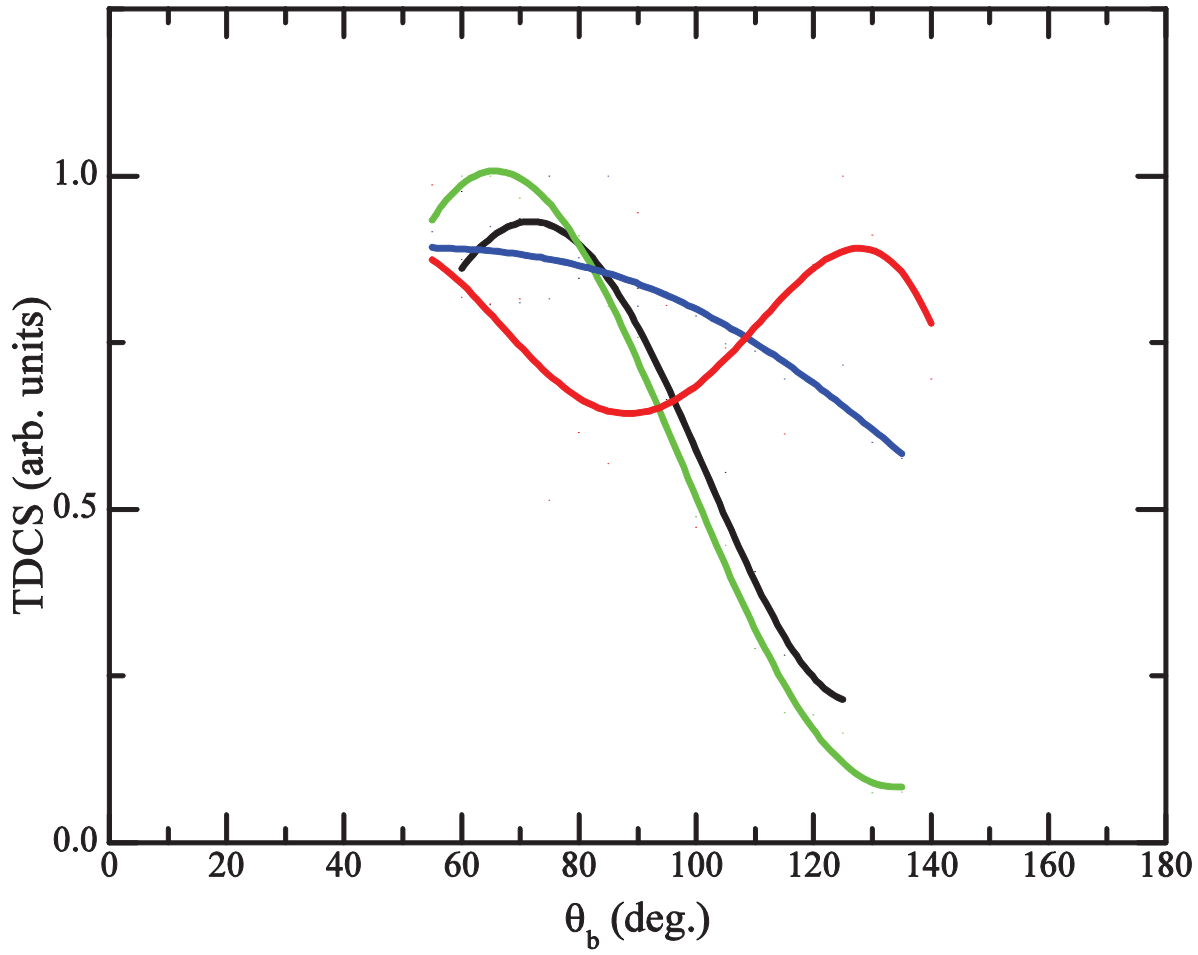

Figure 6.9: A comparison of the Legendre polynomial fits of the binary peaks for the molecules measured in this thesis: thymine (black), THF (red) and formic acid (blue). Helium (green) is included for comparison. The measurements were all performed at similar conditions, where E_0=250 eV and θ_a=-10°.

suggested by the fit of the Legendre polynomials, with a small (approximately 5°) shift to larger angles. It appears that there is some splitting of the binary lobe near the momentum transfer direction, albeit relatively small, which may be an indication of contributions from the 2a″ molecular orbital. The magnitude of the recoil lobe compared to the binary lobe is also very small, in agreement with the findings for formic acid and tetrahydrofuran, whose recoil lobes were also smaller at larger scattering angles. It was suggested previously [41] this lack of recoil intensity is due to the location of the molecules' centre of mass, which in the case of thymine (refer to figure 6.2) and the other molecules studied here (refer to figure 4.9), is quite some distance from a charge centre.

For a scattering angle of -15°, as presented in figure 6.8, the data again exhibits a single, narrow binary lobe that is shifted slightly towards larger angles. Again, the binary lobe is significantly larger than the recoil lobe, consistent with the lack of a charge centre at thymine's centre of mass. However, there is little indication of the 2a″ orbital in the -15° cross

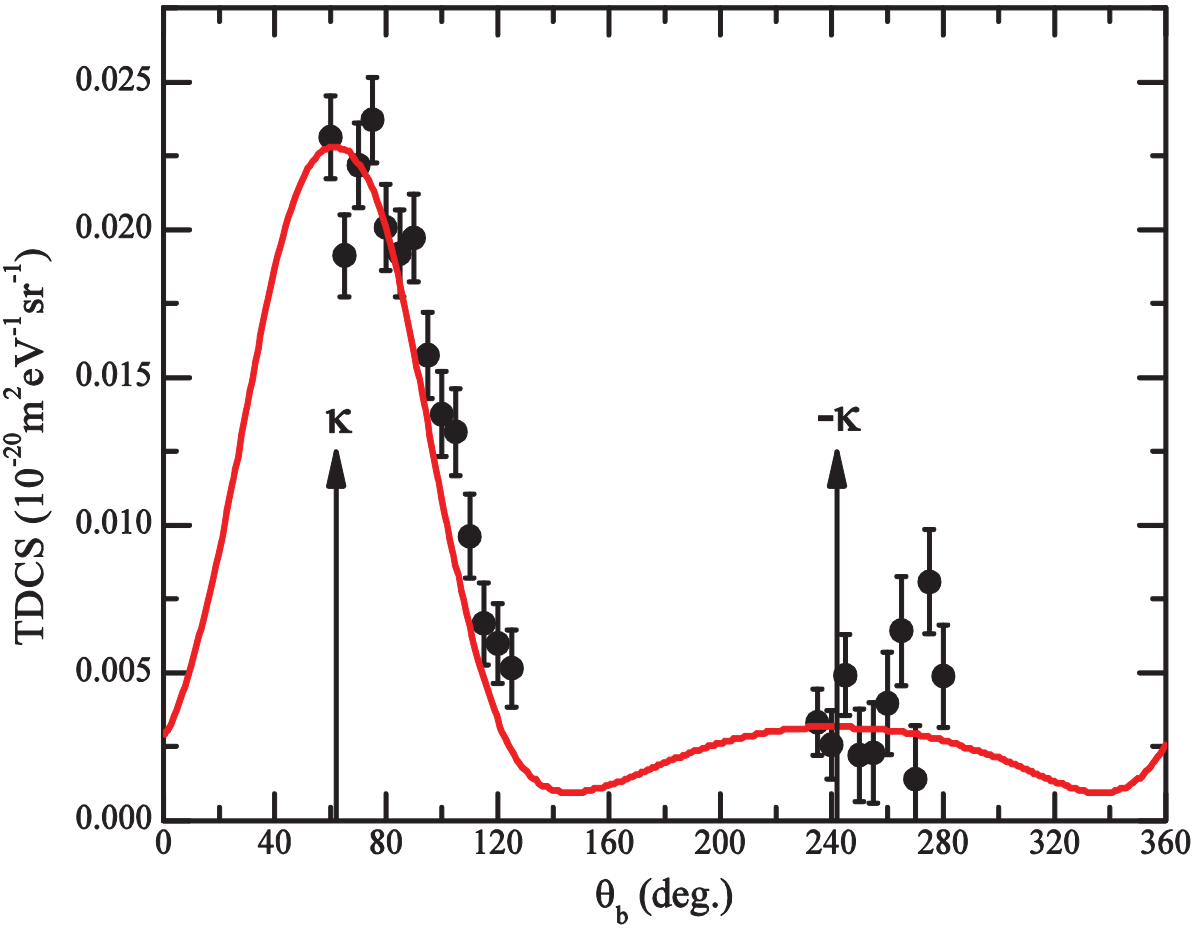

Figure 6.10: Experimental triple differential cross sections for sections for the 2a″+14a′ molecular orbitals of thymine (solid black circles), with E_0=250 eV, E_b=20 eV, θ_a=-10° and $|\boldsymbol{\kappa}|$=0.78 au, compared with the DWBA calculation for the same orbitals (solid red line).

section. Figure 6.9 presents the Legendre polynomial fits for the molecules studied in this thesis, at the common conditions of 250 eV incident energy and -10° scattering angle. Helium is also included for comparison. Here it is quite evident that in comparison to the previously measured cross sections for formic acid and THF, the binary lobe of thymine is significantly narrower. Some of this difference can likely be attributed to the more localised nature of the 2a″ and the 14a′ molecular orbitals, as they are inner valence orbitals. In contrast, the measured orbitals for formic acid and THF were the outermost molecular orbitals, and tended to be delocalised across the entire molecule. However, the majority of this difference is most likely due to negligible contributions from the 2a″ state. The binary lobe of the present thymine measurement is approximately as wide as the helium 1s binary lobe (see figure 6.9). This is a strong suggestion of the 2a″ orbitals absence as, being a p-type state, it is expected to make greater contributions to the TDCS at larger ejected electron angles, and thus larger recoil ion momenta. Without measured or calculated momentum density profiles however, it is difficult to discount contributions from the 2a″ molecular orbital.

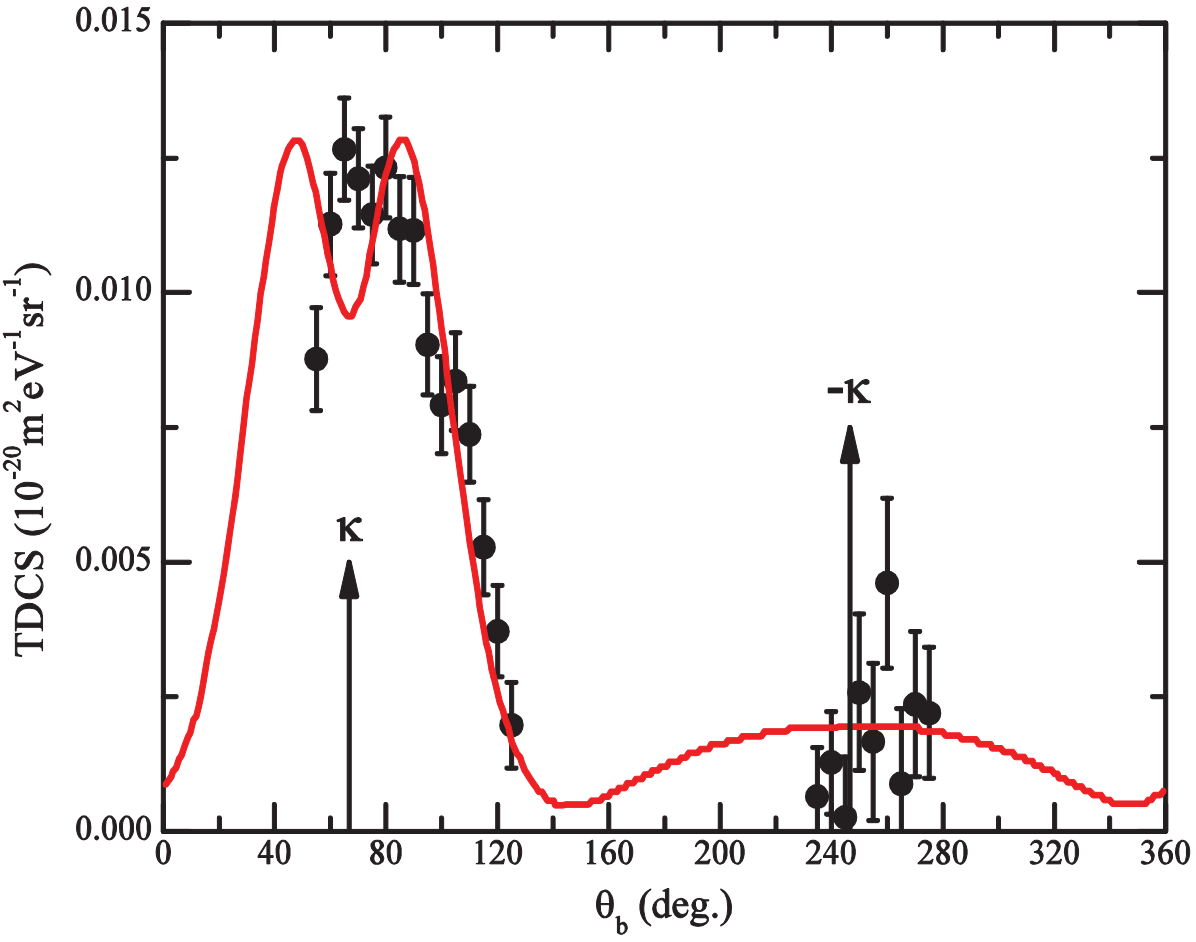

Figure 6.11: Same as figure 6.10, except that θ_a=-15° and $|\boldsymbol{\kappa}|$=1.12 au.

Figures 6.10 and 6.11 compare the present results for thymine with a calculation developed using the distorted-wave Born approximation (DWBA) framework under the same kinematics and for the same molecular orbitals [172]. The incident and scattered channels are described by the use of a plane-wave function multiplied by a molecular wavefunction that is the result of a liner combination of atomic orbitals. The ejected electron instead utilises a distorted-wave function, as it is significantly lower in energy than the other, and very susceptible to distortion effects. Further information regarding the theoretical calculation can be found in Champion *et al.* [173]. For a scattered electron detection angle of -10° (figure 6.10), it is observed that the DWBA is very successful at correctly reproducing both the relative magnitude of the binary and recoil peaks, as well as their shapes. The small splitting of the binary peak evident in the experimental cross section is not predicted by the calculation, suggesting that this is likely just a result of scatter in the experimental data. In figure 6.11, at a scattered angle of -15°, the DWBA calculation is again successful. The magnitude of the recoil peak compared to the binary peak, as well as the shape of the recoil peak, both appear to be predicted quite well by the theory. However, there is some discrepancy in the shape of the binary peak. The calculation predicts a double lobe structure

in the binary region which is not observed in the experimental data, and also predicts a broader binary peak when the experimental results appear to be narrower. This appears to be another good indicator that the 2a″ is making little contribution to the experimental cross sections, as it is undoubtedly responsible for the split binary peak in the DWBA calculation.

Conclusion

7.1 Summary of Results

The experimental cross sections presented within this thesis examine the interactions between electrons and four biologically relevant molecular targets: formic acid, tetrahydrofuran (THF), cytosine and thymine. This study represents the first experimental measurements of the triple differential cross section (TDCS) for electron impact ionization of these molecules. Similarly, this is the first time that single differential cross sections (SDCS) for elastic electron scattering from cytosine and thymine have been measured. This is owing to the difficulty in obtaining vapour targets as well as protecting the experimental apparatus from these highly reactive substances. The large, polyatomic, polycentric nature of these molecules poses a significant challenge to even the most sophisticated scattering theories. Interactions between electrons and these molecules are also of great fundamental importance for understanding the mechanisms of radiation damage, modelling the processes by which energy is deposited and DNA strands are damaged, and in predicting areas of high dosage and of high probability for radiation damage. Electronic interactions are of particular importance as it is now understood that almost half of the radiation damage done to a biological entity is as a result of secondary electrons released during the primary ionizing collision, many of which have energies below the ionization threshold [57]. Monte-Carlo charged particle track structure simulations are used to predict the path of these secondary electrons through biological media, which require accurate electron scattering cross sections as inputs. Electron scattering cross sections for water have been used in these codes to reasonable approximation [174], however for a complete understanding of the radiation damage process other biological molecules need to be considered. In this study, I have presented TDCSs for formic acid, chosen for its role as a simple building block for biological systems; THF, which can be considered a good analogue for the backbone of DNA; and the nucleobase thymine. I have also presented single

differential cross sections SDCSs for the elastic scattering of electrons from the DNA bases cytosine and thymine.

The experimental measurements were performed in a conventional electron coincidence spectrometer, operating in the coplanar asymmetric geometry. Electron impact ionization experiments were all conducted with incident electrons of intermediate energy, ranging from 100 eV up to 250 eV, with a fixed ejected electron energy of 10 eV, with the exception of thymine where the ejected energy was fixed at 20 eV. Scattered electron detection angles ranged from -5° to -15°. Elastic differential cross sections for cytosine and thymine have also been measured in the coincidence spectrometer, for incident electron energies between 60 eV and 500 eV. Due to the mechanical restrictions of the spectrometer, as well as difficulties with the spatial dimensions of the incident electron beam, the electron detection angles range between 10° and 135°.

There are many recurring themes that have emerged from this (e, 2e) study. For all targets considered, the magnitude of the recoil lobe compared to the binary lobe appears to be a function of the scattered electron detection angle, tending to decrease as this angle increases. At the higher incident energy (250 eV) and the larger scattering angles (-10° and -15°) the size of the recoil lobe is greatly reduced, in contrast to water which, under the same kinematics, exhibits a binary-recoil ratio of unity [38]. This lack of recoil interaction is postulated to result from the absence of nuclear charge at the molecule's centre of mass. The TDCSs for the highest occupied molecular orbitals of formic acid and THF both have very broad binary lobes, whereas the binary lobe for the two inner valence orbitals of thymine exhibit helium-like behaviour. This suggests that the breadth of the binary lobe is proportional to the extent of delocalisation of the molecular orbital across the entire molecule, as well as being sensitive to the shape of the orbitals under investigation.

Varying agreement is seen with the theoretical (e, 2e) calculations. The molecular three-body distorted wave (M3DW) style calculations predict the relative size of the binary and recoil peaks quite well, except for the case of THF at a scattering angle of -5°. Impressive shape agreement is seen with the recoil peaks of formic acid, but the M3DW tends to predict large sharp binary peaks. This is likely due to contributions to the binary peak at large angles from the 2a″ state, which has not been included due to limitations with the orientation averaged molecular orbital (OAMO) approximation [41]. The M3DW again predicts narrow binary peaks for THF, and has very limited success in predicting the shape of the recoil peaks. The calculation is again limited by the OAMO approximation, as the two orbitals of THF studied are highly symmetric, so instead a modified version was used [42]. The distorted-wave Born approximation (DWBA) calculation presented for thymine [172] is much more

successful at predicting the binary peak shape, as well remarkable agreement in predicting the relative magnitudes of the binary and recoil peaks. The DWBA calculation does however predict a slightly broader split binary peak in the -15° case, most likely due to contributions from the 2a″ molecular orbital which are not observed in the experimental data.

Excellent agreement is seen between the measured elastic SDCSs of cytosine and thymine and the two theoretical models presented. The screening corrected additivity rule (SCAR) calculation [163] is quite successful at reproducing the shape of the thymine and cytosine cross sections, but tends to underestimate a shoulder which is present in the measured data at approximately 60°. While the independent atom method (IAM) calculation [160] reproduces this shoulder with greater accuracy, it consistently overestimates the cross section at backward angles. The shapes of the published pyrimidine cross sections are also very similar to cytosine and thymine, a derivative of the similarities in their molecular structures.

7.2 Future Directions

Conventional electron coincidence experiments generally suffer from two specific restrictions: the mechanical restriction to the accessible angular range due to the physical size of the apparatus in use as well as the inability to produce TDCS's on an absolute scale.

The limited angular range is clearly evident in all presented cross sections, where large angular regions are unable to be investigated. In 1996, a publication by Read and Channing [175] describes a device termed a magnetic angle changer (MAC) which is able to effectively rotate the scattering plane with respect to the incident electron beam without distorting the TDCS so that inaccessible angular ranges become accessible. This is achieved using two pairs of concentric solenoids which are arranged to generate a magnetic field that is localized at the interaction region. The MAC is designed and arranged so that the incident electron beam will always pass through the common centre of the solenoid coils and the outgoing scattered and ejected electrons are deflected as they emerge from the interaction region. The MAC device has been successfully employed to measure the TDCS of argon in an (e, 2e) experimental apparatus similar to the apparatus described within in this thesis [176]. I propose that additional experimental measurements could incorporate a MAC device into the current (e, 2e) apparatus so that the previously unexplored angular regions can be measured. There should be good cause for doing so however, as the normalisation between regions of different magnetic field strength, and the usually small cross sections in these previously unmeasurable regions, can add great lengths of time to individual measurements. There are other techniques available, namely recoil-ion momentum spectroscopy (see Ullrich *et al.* [177-178] for

comprehensive reviews of this subject), which are available and are much more successful at rapidly measuring the full angular range. At this stage however, no measurements on molecules of biological relevance have been published.

The other failing of the current experimental arrangement is the inability to report absolute values for the measured TDCS. This is of particular importance to charged particle track structure analyses where the relative probability of events occurring from different targets is crucial. Absolute TDCS's provide the ability to achieve internormalisation between all targets concerned. Traditionally TDCS's are given an absolute magnitude via comparison with theory, indeed this is the case with atomic helium and the highly successful CCC calculation of Fursa and Bray [12]. Recently, a method has been devised that involves a mixture of two gases, the target gas as well as a helium standard [179]. If the target gas has a few discrete orbitals so that ionization from the helium 1s orbital can be distinguished from all other events, then it is possible to make some relation between the TDCS's of the two gases as a function of pressure. The absolute scale of a calculated helium cross section can then be applied to the target TDCS. The major limitation of this method is the need for the target to not have any contribution to the TDCS at an energy in the vicinity of the helium 1s ionization energy (24.6 eV). For molecules this can be quite difficult to achieve, and molecular nitrogen and water have been identified as suitable candidates for being normalisation of this fashion. This is unfortunate, but due to the great quantity and energy spread of molecular orbitals in molecules as large as the ones under investigation, it is not possible to use this method for all targets, including those studied in this thesis.

Although a number of cross sections have been reported for the molecules in this present study there are several additional experiments that could be performed. In an effort to provide benchmark cross sections for their use in charged particle track structure analysis (CPTSA), a number of different electron detection angles, electron detection energies and even different kinematic geometries could be investigated that would not only be of value in providing benchmark cross sections but would also provide the opportunity for more rigorous testing of scattering theories. With a view to further understand the binary peak shapes as a function of electron delocalisation, the entire valence region of these molecules could be investigated rather than just one or two for each molecule. It is the intention that a rigorous study of the remaining DNA and RNA bases be conducted to provide benchmark cross sections for use in CPTSA, both elastic and triply differential ionization cross sections. These measurements would certainly be of value, not only in CPTSA but they would also provide further insight into the centre of mass location affects the size of the recoil peak as a function of distance from a charge centre as well as for different molecular orbital shapes.

Appendix A: Experimental (e, 2e) Data

8.1 Formic Acid

This appendix contains the experimental data for the electron impact ionization of the formic acid monomer, as presented in chapter 4. The binding energy spectrum data is given in arbitrary units, while the angular distributions have been given absolute scale via normalisation to the M3DW-CPE calculation in the recoil region and as such are reported in atomic units.

ε_i	**TDCS**	ε_i	**TDCS**	ε_i	**TDCS**
11.2	0.49 (0.11)	14.8	1.14 (0.14)	18.4	0.12 (0.12)
11.5	0.66 (0.13)	15.1	1.10 (0.12)	18.7	0.34 (0.14)
11.8	0.68 (0.11)	15.4	1.10 (0.14)	19.0	0.22
12.1	0.77 (0.13)	15.7	1.16 (0.13)	19.3	0.34
12.4	0.57 (0.12)	16.0	1.02 (0.14)	19.6	-0.04
12.7	0.53 (0.12)	16.3	0.94 (0.13)	19.9	0.12
13.1	0.08 (0.12)	16.6	0.84 (0.14)	20.3	0.11
13.3	0.23 (0.12)	17.0	1.31 (0.13)	20.5	0.30
13.7	0.39 (0.13)	17.2	1.06 (0.13)	20.7	0.13
13.9	0.47 (0.12)	17.4	1.17 (0.14)	21.1	0.19
14.1	0.75 (0.13)	17.8	0.92 (0.13)		
14.5	1.26 (0.13)	18.1	0.74 (0.15)		

Table 8.1: The measured coincidence binding energy spectrum for the outer valence region of the formic acid monomer, for E_0=250 eV, E_b=10 eV, θ_a=-5° and θ_b=90°. Binding energies ε_i are reported in eV while the measured TDCS and the associated errors (reported in parentheses) are relative values.

	E_0=100 eV			E_0=250 eV	
θ_b	θ_a=-10°	θ_a=-15°	θ_a=-5°	θ_a=-10°	θ_a=-15°
50	0.50 (0.04)				1.08 (0.24)
55		0.95 (0.07)		1.56 (0.14)	1.14 (0.22)
60	0.48 (0.04)		0.95 (0.06)	1.49 (0.12)	1.18 (0.21)
65		0.85 (0.06)	0.93 (0.06)	1.58 (0.12)	1.40 (0.20)
70	0.59 (0.04)		0.89 (0.06)	1.38 (0.11)	1.28 (0.19)
75		0.84 (0.07)	1.00 (0.07)	1.39 (0.10)	1.34 (0.18)
80	0.56 (0.04)		1.06 (0.06)	1.50 (0.10)	1.55 (0.17)
85		0.82 (0.07)	0.97 (0.06)	1.71 (0.09)	1.58 (0.16)
90	0.52 (0.04)		1.02 (0.06)	1.37 (0.09)	1.83 (0.16)
95		0.55 (0.06)	0.94 (0.06)	1.41 (0.09)	1.44 (0.15)
100	0.54 (0.04)		1.01 (0.07)	1.35 (0.10)	1.45 (0.16)
105		0.64 (0.06)	0.99 (0.07)	1.28 (0.10)	1.12 (0.16)
110	0.45 (0.04)		0.96 (0.07)	1.26 (0.10)	1.16 (0.16)
115		0.80 (0.07)	0.91 (0.07)	1.19 (0.10)	0.89 (0.16)
120	0.44 (0.04)		0.94 (0.08)	1.18 (0.11)	0.99 (0.16)
125		0.56 (0.08)	0.84 (0.08)	1.22 (0.12)	1.25 (0.15)
130	0.29 (0.04)		0.78 (0.09)	1.03 (0.14)	0.58 (0.14)
135		0.64 (0.08)	0.84 (0.10)	0.98 (0.16)	0.79 (0.15)
140	0.27 (0.04)		0.73 (0.08)		0.74 (0.15)
290			0.53 (0.10)		
285		0.58 (0.08)	0.64 (0.09)	0.44 (0.17)	
280	0.41 (0.04)		0.54 (0.09)	0.41 (0.17)	0.27 (0.12)
275		0.60 (0.08)	0.79 (0.09)	0.31 (0.17)	0.24 (0.11)
270	0.46 (0.04)		0.59 (0.08)	0.54 (0.17)	0.23 (0.11)
265		0.63 (0.08)	0.77 (0.08)	0.64 (0.16)	0.08 (0.11)
260	0.41 (0.04)		0.59 (0.08)	0.41 (0.16)	0.28 (0.10)
255		0.53 (0.08)	0.73 (0.08)	0.68 (0.16)	0.22 (0.10)
250	0.37 (0.04)		0.78 (0.07)	0.50 (0.15)	0.22 (0.10)
245		0.55 (0.08)	0.76 (0.07)	0.51 (0.16)	0.26 (0.11)
240	0.34 (0.04)		0.76 (0.07)	0.59 (0.16)	0.18 (0.11)
235		0.66 (0.09)	0.81 (0.08)	0.56 (0.16)	0.06 (0.11)
230	0.45 (0.04)		0.83 (0.09)	0.50 (0.17)	0.14 (0.12)
225		0.59 (0.09)	0.76 (0.09)	0.64 (0.17)	0.26 (0.12)
220	0.51 (0.04)		0.83 (0.08)		0.29 (0.12)

Table 8.2: Experimental triple differential cross sections for the 10a′+ 2a″ valence orbitals of formic acid for a range of incident electron energies and scattering angles, with a set ejected electron energy of 10 eV. The TDCS values are in atomic units, and the error in these values are presented in parentheses.

8.2 Tetrahydrofuran

This appendix contains the experimental data for the electron impact ionization of the tetrahydrofuran molecule, as presented in chapter 5. The binding energy spectrum data is given in arbitrary units, while the angular distributions are also reported as arbitrary units but have been normalised to unity.

ε_i	**TDCS**	ε_i	**TDCS**	ε_i	**TDCS**
8.5	0.03 (0.85)	12.4	6.89 (0.74)	16.3	13.07 (0.77)
8.8	0.46 (0.84)	12.7	5.52 (0.72)	16.6	16.24 (0.78)
9.1	0.21 (0.84)	13.0	5.99 (0.72)	16.9	15.76 (0.80)
9.4	2.45 (0.85)	13.3	5.07 (0.73)	17.2	12.86 (0.79)
9.7	1.63 (0.81)	13.6	3.14 (0.70)	17.5	8.78 (0.76)
10.0	1.19 (0.69)	13.9	3.59 (0.71)	17.8	7.12 (0.77)
10.3	1.73 (0.69)	14.2	4.60 (0.71)	18.1	4.33 (0.74)
10.6	0.47 (0.67)	14.5	4.01 (0.71)	18.4	2.48 (0.77)
10.9	2.64 (0.69)	14.8	2.60 (0.71)	18.7	1.87 (0.78)
11.2	3.51 (0.70)	15.1	2.58 (0.69)	19.0	1.21 (0.78)
11.5	4.60 (0.73)	15.4	2.95 (0.70)	19.3	2.77 (0.78)
11.8	6.53 (0.73)	15.7	6.16 (0.73)	19.6	4.03 (0.78)
12.1	6.12 (0.73)	16.0	9.48 (0.75)	19.9	1.32 (0.76)

Table 8.3: The measured coincidence binding energy spectrum for the outer valence region of the tetrahydrofuran molecule, for E_0=250 eV, E_b=10 eV, θ_a=-10° and θ_b=90°. Binding energies ε_i are reported in eV while the measured TDCS and the associated errors (reported in parentheses) are relative values.

		E_0=250 eV	
θ_b	θ_a=-5°	θ_a=-10°	θ_a=-15°
50			0.70 (0.20)
55		0.99 (0.14)	0.81 (0.19)
60	0.88 (0.13)	0.82 (0.14)	0.66 (0.18)
65	0.77 (0.12)	0.81 (0.13)	0.99 (0.18)
70	0.69 (0.11)	0.82 (0.13)	0.89 (0.16)
75	0.85 (0.10)	0.51 (0.12)	0.86 (0.15)
80	0.89 (0.10)	0.62 (0.12)	0.65 (0.14)
85	1.00 (0.09)	0.57 (0.12)	0.75 (0.14)
90	0.88 (0.09)	0.94 (0.12)	0.78 (0.14)
95	0.90 (0.09)	0.80 (0.12)	0.92 (0.13)
100	0.72 (0.09)	0.47 (0.12)	0.93 (0.13)
105	0.74 (0.10)	0.74 (0.13)	0.71 (0.13)
110	0.78 (0.10)	0.78 (0.14)	0.91 (0.14)
115	0.79 (0.11)	0.61 (0.15)	0.89 (0.13)
120	0.48 (0.12)	0.87 (0.15)	1.00 (0.13)
125	0.61 (0.12)	1.00 (0.15)	0.76 (0.14)
130	0.62 (0.14)	0.91 (0.15)	0.75 (0.14)
135	0.23 (0.16)	0.86 (0.17)	0.82 (0.14)
140	0.66 (0.15)	0.69 (0.19)	
290	0.61 (0.15)		
285	0.73 (0.14)	-0.09 (0.11)	
280	0.49 (0.14)	0.07 (0.12)	0.53 (0.16)
275	0.52 (0.14)	-0.11 (0.11)	0.01 (0.16)
270	0.69 (0.14)	0.11 (0.11)	0.19 (0.15)
265	0.56 (0.13)	0.05 (0.11)	0.39 (0.14)
260	0.65 (0.13)	-0.18 (0.11)	0.32 (0.15)
255	0.47 (0.13)	-0.04 (0.11)	0.29 (0.14)
250	0.53 (0.13)	0.16 (0.11)	0.61 (0.14)
245	0.63 (0.13)	0.09 (0.11)	0.26 (0.14)
240	0.48 (0.13)	0.25 (0.12)	0.20 (0.15)
235	0.85 (0.13)	0.22 (0.12)	0.47 (0.16)
230	0.64 (0.13)	0.09 (0.12)	0.42 (0.16)
225	0.87 (0.14)	0.11 (0.13)	0.31 (0.17)
220	1.01 (0.15)	0.06 (0.13)	

Table 8.4: Experimental triple differential cross sections for the 9b+12a′ valence orbitals of tetrahydrofuran for a range of incident electron energies and scattering angles, with a set ejected electron energy of 10 eV. The values have been normalised to unity, and the error in these values are presented in parentheses.

8.3 Thymine

This appendix contains the experimental data for the electron impact ionization of the thymine molecule, as presented in chapter 6. The binding energy spectrum data is given in arbitrary units, while the angular distributions are also reported in units of $10^{-22}m^2eV^{-1}sr^{-1}$ as they have been normalised to the DWBA calculation in the binary region

ε_i	**TDCS**	ε_i	**TDCS**	ε_i	**TDCS**
7.4	-13 (29)	13.4	131 (24)	19.1	78 (23)
7.7	8 (20)	13.7	117 (24)	19.4	44 (22)
8.0	-6 (20)	14.0	188 (25)	19.7	44 (22)
8.3	31 (21)	14.3	170 (24)	20.0	82 (23)
8.6	17 (21)	14.6	210 (25)	20.3	62 (23)
8.9	36 (21)	14.9	205 (25)	20.6	35 (22)
9.2	54 (22)	15.2	212 (25)	20.9	119 (22)
9.5	64 (22)	15.5	171 (25)	21.2	61 (23)
9.8	66 (22)	15.8	171 (25)	21.5	47 (22)
10.1	39 (21)	16.1	80 (23)	21.8	41 (22)
10.4	34 (21)	16.4	80 (23)	22.1	60 (23)
10.7	38 (21)	16.7	68 (23)	22.4	38 (22)
11.0	76 (22)	17.0	14 (21)	22.7	35 (22)
11.3	78 (22)	17.3	62 (22)	23.0	33 (22)
11.6	41 (22)	17.6	63 (23)	23.3	65 (23)
11.9	113 (23)	17.9	59 (22)	23.6	26 (22)
12.2	79 (23)	18.2	87 (23)	23.9	48 (23)
12.5	135 (24)	18.5	22 (22)	24.2	48 (23)
12.8	121 (23)	18.8	76 (23)	24.5	22 (22)
13.1	166 (24)				

Table 8.5: The measured coincidence binding energy spectrum for the outer valence region of the thymine molecule, for E_0=250 eV, E_b=20 eV, θ_a=-10° and θ_b=75°. Binding energies ε_i are reported in eV while the measured TDCS and the associated errors (reported in parentheses) are relative values.

	E_0=250 eV	
θ_b	θ_a=-10°	θ_a=-15°
55		0.88 (0.10)
60	2.31 (0.14)	1.13 (0.10)
65	1.91 (0.14)	1.27 (0.09)
70	2.22 (0.14)	1.21 (0.09)
75	2.37 (0.15)	1.15 (0.09)
80	2.01 (0.15)	1.23 (0.09)
85	1.92 (0.15)	1.12 (0.10)
90	1.97 (0.15)	1.12 (0.10)
95	1.58 (0.15)	0.90 (0.09)
100	1.38 (0.15)	0.79 (0.09)
105	1.31 (0.15)	0.84 (0.09)
110	0.96 (0.14)	0.74 (0.09)
115	0.67 (0.14)	0.53 (0.09)
120	0.60 (0.14)	0.37 (0.08)
125	0.52 (0.13)	0.20 (0.08)
280	0.49 (0.17)	
275	0.81 (0.18)	0.22 (0.12)
270	0.14 (0.18)	0.24 (0.14)
265	0.64 (0.18)	0.09 (0.14)
260	0.40 (0.17)	0.46 (0.16)
255	0.23 (0.17)	0.17 (0.15)
250	0.22 (0.16)	0.26 (0.15)
245	0.49 (0.14)	0.03 (0.11)
240	0.26 (0.12)	0.13 (0.10)
235	0.33 (0.11)	0.06 (0.09)

Table 8.6: Experimental triple differential cross sections for the 2a″+14a′ molecular orbitals of thymine for a range of incident electron energies and scattering angles, with a set ejected electron energy of 20 eV. The TDCS values are units of $10^{-22}m^2eV^{-1}sr^{-1}$, and the error in these values are presented in parentheses.

Appendix B: Experimental Elastic Data

9.1 Cytosine

This appendix contains the experimental data for elastic collisions of electrons from the cytosine molecule, as presented in chapter 6. The angular distributions have been attributed absolute scale via normalisation to the SCAR calculation to give the best visual fit. The data is reported in units of $10^{-20}m^2sr^{-1}$.

θ	60 eV	100 eV	200 eV	300 eV	400 eV	500 eV
10					11.24 (0.40)	9.09 (0.34)
15				9.06 (0.98)	4.50 (0.25)	3.76 (0.02)
20	17.6 (1.5)	7.98 (0.85)	4.47 (0.11)	3.42 (0.14)	2.70 (0.11)	1.89 (0.05)
25	7.14 (0.7)	3.67 (0.33)	2.67 (0.04)	1.99 (0.02)	1.20 (0.06)	1.05 (0.01)
30	3.59 (0.36)	2.23 (0.15)	1.70 (0.03)	1.11 (0.03)	1.15 (0.06)	0.99 (0.01)
35	2.28 (0.15)	1.65 (0.09)	0.94 (0.01)	0.58 (0.01)	0.80 (0.02)	0.45 (0.01)
40	1.85 (0.08)	1.17 (0.06)	0.69 (0.02)	0.58 (0.01)	0.38 (0.01)	0.24 (0.01)
45	1.57 (0.07)	0.77 (0.04)	0.67 (0.02)	0.46 (0.01)	0.24 (0.01)	0.20 (0.01)
50	1.26 (0.06)	0.54 (0.03)	0.56 (0.01)	0.25 (0.01)	0.20 (0.01)	0.18 (0.01)
55	0.93 (0.06)	0.45 (0.02)	0.38 (0.01)	0.16 (0.01)	0.16 (0.01)	0.14 (0.01)
60	0.66 (0.04)	0.42 (0.02)	0.25 (0.01)	0.13 (0.01)	0.13 (0.01)	0.11 (0.01)
65	0.50 (0.02)	0.40 (0.02)	0.19 (0.01)	0.11 (0.01)	0.12 (0.01)	0.07 (0.01)
70	0.43 (0.02)	0.33 (0.02)	0.16 (0.01)	0.10 (0.01)	0.09 (0.01)	0.06 (0.01)
75	0.42 (0.02)	0.27 (0.02)	0.15 (0.01)	0.09 (0.01)	0.07 (0.01)	0.05 (0.01)
80	0.42 (0.01)	0.23 (0.01)	0.15 (0.01)	0.08 (0.01)	0.06 (0.01)	0.04 (0.01)
85	0.43 (0.01)	0.19 (0.01)	0.14 (0.01)	0.08 (0.01)	0.05 (0.01)	0.04 (0.01)
90	0.44 (0.01)	0.19 (0.01)	0.13 (0.01)	0.06 (0.01)	0.05 (0.01)	0.03 (0.01)
95	0.45 (0.02)	0.19 (0.01)	0.13 (0.01)	0.06 (0.01)	0.05 (0.01)	0.03 (0.01)
100	0.49 (0.02)	0.21 (0.01)	0.12 (0.01)	0.06 (0.01)	0.04 (0.01)	0.03 (0.01)
105	0.50 (0.01)	0.23 (0.01)	0.12 (0.01)	0.06 (0.01)	0.04 (0.01)	0.02 (0.01)
110	0.52 (0.01)	0.25 (0.01)	0.11 (0.01)	0.06 (0.01)	0.04 (0.01)	0.02 (0.01)
115	0.58 (0.02)	0.29 (0.02)	0.11 (0.01)	0.06 (0.01)	0.03 (0.01)	0.02 (0.01)
120	0.68 (0.02)	0.33 (0.02)	0.11 (0.01)	0.05 (0.01)	0.03 (0.01)	0.02 (0.01)
125	0.80 (0.04)	0.37 (0.02)	0.11 (0.01)	0.06 (0.01)		

Table 9.1: Experimental single differential cross sections for electron scattering from cytosine for a range of incident electron energies. The present data is attributed absolute values via normalisation to the SCAR calculations at the corresponding energy, in units of $10^{-20}m^2sr^{-1}$ with the associated error shown in parentheses.

9.2 Thymine

This appendix contains the experimental data for elastic scattering of electrons from the thymine molecule, as presented in chapter 6. The angular distributions have been attributed absolute scale via normalisation to the SCAR calculation to give the best visual fit. The data is reported in units of $10^{-20}m^2sr^{-1}$.

θ	100 eV	200 eV	300 eV	400 eV	500 eV
20	11.73 (1.26)	7.82 (0.01)	4.05 (0.01)	3.36 (0.01)	3.36 (0.28)
25	4.96 (0.47)	5.09 (0.01)	1.78 (0.01)	1.50 (0.01)	1.70 (0.02)
30	3.25 (0.27)	3.39 (0.01)	1.39 (0.01)	1.49 (0.01)	1.56 (0.03)
35	2.54 (0.22)	1.70 (0.01)	1.28 (0.01)	0.95 (0.01)	0.73 (0.04)
40	1.97 (0.18)	1.18 (0.01)	0.77 (0.01)	0.47 (0.01)	0.40 (0.01)
45	1.30 (0.12)	1.19 (0.01)	0.44 (0.01)	0.31 (0.01)	0.29 (0.01)
50	0.81 (0.07)	1.00 (0.01)	0.31 (0.01)	0.25 (0.01)	0.21 (0.01)
55	0.64 (0.06)	0.64 (0.01)	0.25 (0.01)	0.20 (0.01)	0.16 (0.01)
60	0.62 (0.05)	0.41 (0.01)	0.22 (0.01)	0.15 (0.01)	0.13 (0.01)
65	0.60 (0.05)	0.32 (0.01)	0.18 (0.01)	0.13 (0.01)	0.09 (0.01)
70	0.52 (0.04)	0.27 (0.01)	0.16 (0.01)	0.10 (0.01)	0.07 (0.01)
75	0.41 (0.04)	0.26 (0.01)	0.15 (0.01)	0.08 (0.01)	0.06 (0.01)
80	0.33 (0.03)	0.27 (0.01)	0.12 (0.01)	0.07 (0.01)	0.05 (0.01)
85	0.27 (0.02)	0.24 (0.01)	0.10 (0.01)	0.06 (0.01)	0.04 (0.01)
90	0.25 (0.02)	0.21 (0.01)	0.09 (0.01)	0.06 (0.01)	0.04 (0.01)
95	0.26 (0.02)	0.20 (0.01)	0.08 (0.01)	0.05 (0.01)	0.03 (0.01)
100	0.29 (0.02)	0.19 (0.01)	0.08 (0.01)	0.04 (0.01)	0.03 (0.01)
105	0.32 (0.02)	0.17 (0.01)	0.08 (0.01)	0.04 (0.01)	0.03 (0.01)
110	0.35 (0.02)	0.16 (0.01)	0.07 (0.01)	0.04 (0.01)	0.02 (0.01)
115	0.38 (0.02)	0.15 (0.01)	0.07 (0.01)	0.03 (0.01)	0.02 (0.01)
120	0.41 (0.03)	0.15 (0.01)	0.06 (0.01)	0.03 (0.01)	0.02 (0.01)
125	0.45 (0.03)	0.15 (0.01)	0.07 (0.01)	0.03 (0.01)	0.02 (0.01)
130		0.15 (0.01)	0.06 (0.01)	0.03 (0.01)	0.02 (0.01)

Table 9.2: Experimental single differential cross sections for electron scattering from thymine for a range of incident electron energies. The present data is attributed absolute values via normalisation to the SCAR calculations at the corresponding energy, in units of $10^{-20}m^2sr^{-1}$ with the associated error shown in parentheses.

Bibliography

[1] Lenard P *Annalen der Physik* **317** 714-44 (1903)

[2] Rutherford E *Philosophical Magazine* **21** 669 (1911)

[3] Ramsauer C *Annalen der Physik* **369** 513-40 (1921)

[4] Langmuir I and Jones H A *Physical Review* **31** 357 (1928)

[5] Rudberg E *Proceedings of the Royal Society of London Series A* **129** 628 (1930)

[6] Bethe H *Annalen der Physik* **5** 325 (1930)

[7] Hughes A L and McMillen J H *Physical Review* **39** 585 (1932)

[8] Hughes A L and Mann M *Physical Review* **53** 50 (1938)

[9] Amaldi J U, Egidi A, Marconero R and Pizzella G *Review of Scientific Instruments* **40** 1001-4 (1969)

[10] Ehrhardt H, Schulz M, Tekaat T and Willmann K *Physical Review Letters* **22** 89 (1969)

[11] Bray I, Konovalov D A, McCarthy I E and Stelbovics A T *Physical Review A: Atomic, Molecular, and Optical Physics* **50** R2818 (1994)

[12] Fursa D V and Bray I *Physical Review A: Atomic, Molecular, and Optical Physics* **52** 1279 (1995)

[13] Bray I and Fursa D V *Physical Review A: Atomic, Molecular, and Optical Physics* **54** 2991 (1996)

[14] Fursa D V and Bray I *Physical Review A: Atomic, Molecular, and Optical Physics* **59** 282 (1999)

[15] Fursa D V, Bray I, Panajotovic R, Sevic D, Pejcev V, Filipovic D M and Marinkovic B P *Physical Review A: Atomic, Molecular, and Optical Physics* **72** 012706-9 (2005)

[16] Bartschat K and Bray I *Physical Review A: Atomic, Molecular, and Optical Physics* **54** 1723 (1996)

[17] Lahmam-Bennani A *Journal of Physics B: Atomic and Molecular Physics* **24** 2401-42 (1991)

[18] Coplan M A, Moore J H and Doering J P *Reviews of Modern Physics* **66** 985 (1994)

[19] McCarthy I E and Weigold E *Reports on Progress in Physics* **51** 299 (1988)

[20] McCarthy I E *Australian Journal of Physics* **51** 593-607 (1998)

[21] Takahashi M *Bulletin of the Chemical Society of Japan* **82** 751-77 (2009)

[22] Jung K, Schubert E, Paul D A L and Ehrhardt H *Journal of Physics B: Atomic and Molecular Physics* **8** 1330-7 (1975)

[23] Casagrande E M S, Naja A, Mezdari F, Lahmam-Bennani A, Bolognesi P, Joulakian B, Chuluunbaatar O, Al-Hagan O, Madison D H, Fursa D V and Bray I *Journal of Physics B: Atomic and Molecular Physics* **41** 025204 (2008)

[24] Cherid M, Lahmam-Bennani A, Duguet A, Zurales R W, Lucchese R R, Dal Cappello M C and Dal Cappello C *Journal of Physics B: Atomic and Molecular Physics* **22** 3483-99 (1989)

[25] Milne-Brownlie D S, Foster M, Gao J, Lohmann B and Madison D H *Physical Review Letters* **96** 233201-4 (2006)

[26] Hargreaves L R, Colyer C, Stevenson M A, Lohmann B, Al-Hagan O, Madison D H and Ning C G *Physical Review A: Atomic, Molecular, and Optical Physics* **80** 062704-7 (2009)

[27] Avaldi L, Camilloni R, Fainelli E and Stefani G *Journal of Physics B: Atomic, Molecular and Optical Physics* **25** 3551-63 (1992)

[28] Doering J P and Yang J *Physical Review A: Atomic, Molecular, and Optical Physics* **54** 3977 (1996)

[29] Rioual S, Nguyen Vien G and Pochat A *Physical Review A: Atomic, Molecular, and Optical Physics* **54** 4968 (1996)

[30] Hussey M J and Murray A J *Journal of Physics B: Atomic, Molecular and Optical Physics* **35** 3399-409 (2002)

[31] Naja A, Staicu-Casagrande E M, Lahmam-Bennani A, Nekkab M, Mezdari F, Joulakian B, Chuluunbaatar O and Madison D H *Journal of Physics B: Atomic, Molecular and Optical Physics* **40** 3775-83 (2007)

[32] Lahmam-Bennani A, Staicu-Casagrande E M and Naja A *Journal of Physics B: Atomic, Molecular and Optical Physics* **42** 235205 (2009)

[33] Murray A J, Hussey M J, Gao J and Madison D H *Journal of Physics B: Atomic, Molecular and Optical Physics* **39** 3945-56 (2006)

[34] Yang J and Doering J P *Physical Review A: Atomic, Molecular, and Optical Physics* **63** 032717 (2001)

[35] Hussey M J and Murray A J *Journal of Physics B: Atomic and Molecular Physics* **38** 2965-77 (2005)

[36] Cavanagh S J and Lohmann B *Journal of Physics B: Atomic and Molecular Physics* **32** L261-L70 (1999)

[37] Nixon K L, Murray A, Al-Hagan O, Madison D H and Ning C *Journal of Physics B: Atomic, Molecular and Optical Physics* **43** 035201 (2010)

[38] Milne-Brownlie D S, Cavanagh S J, Lohmann B, Champion C, Hervieux P A and Hanssen J *Physical Review A: Atomic, Molecular, and Optical Physics* **69** 032701-4 (2004)

[39] Kaiser C, Spieker D, Gao J, Hussey M, Murray A and Madison D H *Journal of Physics B: Atomic and Molecular Physics* **40** 2563-76 (2007)

[40] Lahmam-Bennani A, Naja A, Staicu-Casagrande E M, Okmus N, Dal Cappello C, Charpentier I and Houamer S *Journal of Physics B: Atomic, Molecular and Optical Physics* **42** 165201 (2009)

[41] Colyer C J, Stevenson M A, Al-Hagan O, Madison D H, Ning C G and Lohmann B *Journal of Physics B: Atomic, Molecular and Optical Physics* **42** 235207 (2009)

[42] Colyer C J, Bellm S M, Lohmann B, Hanne G F, Al-Hagan O, Madison D H and Ning C G *The Journal of Chemical Physics* **133** 124302-7 (2010)

[43] Weck P, Joulakian B and Hervieux P A *Physical Review A: Atomic, Molecular, and Optical Physics* **60** 3013 (1999)

[44] Weck P, Joulakian B, Hanssen J, Fojón O A and Rivarola R D *Physical Review A: Atomic, Molecular, and Optical Physics* **62** 014701 (2000)

[45] Monzani A L, Machado L E, Lee M T and Machado A M *Physical Review A: Atomic, Molecular, and Optical Physics* **60** R21 (1999)

[46] Houamer S, Mansouri A, Cappello C D, Lahmam-Bennani A, Elazzouzi S, Moulay M and Charpentier I *Journal of Physics B: Atomic and Molecular Physics* **36** 3009-24 (2003)

[47] Stia C R, Fojón O A, Weck P F, Hanssen J and Rivarola R D *Journal of Physics B: Atomic and Molecular Physics* **36** L257-L64 (2003)

[48] Gao J, Madison D H and Peacher J L *Physical Review A: Atomic, Molecular, and Optical Physics* **72** 020701-4 (2005)

[49] Gao J, Madison D H and Peacher J L *The Journal of Chemical Physics* **123** 204314-6 (2005)

[50] Gao J, Madison D H and Peacher J L *Physical Review A: Atomic, Molecular, and Optical Physics* **72** 032721-5 (2005)

[51] Champion C, Hanssen J and Hervieux P A *Physical Review A: Atomic, Molecular, and Optical Physics* **63** 052720 (2001)

[52] Champion C *Physics in Medicine and Biology* **48** 2147-68 (2003)

[53] Champion C, Cappello C D, Houamer S and Mansouri A *Physical Review A: Atomic, Molecular, and Optical Physics* **73** 012717-9 (2006)

[54] Avaldi L, Camilloni R and Stefani G *Physical Review A: Atomic, Molecular, and Optical Physics* **41** 134 (1990)

[55] Tóth I and Nagy L *Journal of Physics B: Atomic and Molecular Physics* **43** 135204 (2010)

[56] Boudaïffa B, Cloutier P, Hunting D, Huels M A and Sanche L *Science* **287** 1658-60 (2000)

[57] Cobut V, Frongillo Y, Patau J P, Goulet T, Fraser M J and Jay-Gerin J P *Radiation Physics and Chemistry* **51** 229-43 (1998)

[58] Goodhead D T *International Journal of Radiation Biology* **65** 7 - 17 (1994)

[59] Varella M T D N, Bettega M H F, Lima M A P and Ferreira L G *Journal of Chemical Physics* **111** 6396 (1999)

[60] Ptasinska S, Denifl S, Scheier P and Mark T D *The Journal of Chemical Physics* **120** 8505-11 (2004)

[61] Vizcaino V, Jelisavcic M, Sullivan J P and Buckman S J *New Journal of Physics* **8** 85 (2006)

[62] Huels M A, Hahndorf I, Illenberger E and Sanche L *The Journal of Chemical Physics* **108** 1309-12 (1998)

[63] Boudaïffa B, Cloutier P, Hunting D, Huels M A and Sanche L *Radiation Research* **157** 227-34 (2002)

[64] Hanel G, Gstir B, Denifl S, Scheier P, Probst M, Farizon B, Farizon M, Illenberger E and Märk T D *Physical Review Letters* **90** 188104 (2003)

[65] Denifl S, Ptasinska S, Cingel M, Matejcik S, Scheier P and Mark T D *Chemical Physics Letters* **377** 74-80 (2003)

[66] Abdoul-Carime H, Gohlke S and Illenberger E *Physical Review Letters* **92** 168103-4 (2004)

[67] Aflatooni K, Scheer A M and Burrow P D *The Journal of Chemical Physics* **125** 054301-5 (2006)

[68] Martin F, Burrow P D, Cai Z, Cloutier P, Hunting D and Sanche L *Physical Review Letters* **93** 068101-4 (2004)

[69] Hill M A *Radiation Measurements* **31** 15-23 (1999)

[70] Nikjoo H and Goodhead D T *Physics in Medicine & Biology* **36** 229 (1991)

[71] Nikjoo H, Terrisol M, Hamm R N, Turner J E, Uehara S, Paretzke H G and Goodhead D T *Radiation Protection Dosimetry* **52** 165 (1994)

[72] Nikjoo H, Uehara S, Emfietzoglou D and Cucinotta F A *Radiation Measurements* **41** 1052-74 (2006)

[73] Nikjoo H, O'Neill P, Goodhead D T and Terrissol M *International Journal of Radiation Biology* **71** 467 (1997)

[74] Nikjoo H, Uehara S, Wilson W E, Hoshi M and Goodhead D T *International Journal of Radiation Biology* **73** 355 - 64 (1998)

[75] Martyn H and et al. *Journal of Physics B: Atomic, Molecular and Optical Physics* **41** 055202 (2008)

[76] Johnstone W M, Mason N J and Newell W R *Journal of Physics B: Atomic and Molecular Physics* **26** L147 (1993)

[77] Kato H, Kawahara H, Hoshino M, Tanaka H, Campbell L and Brunger M J *Chemical Physics Letters* **465** 31-5 (2008)

[78] Norcross D W *Journal of Physics B: Atomic and Molecular Physics* **4** 1458 (1971)

[79] Brunger M J and et al. *Journal of Physics B: Atomic and Molecular Physics* **24** 1435 (1991)

[80] Colyer C J, Vizcaino V, Sullivan J P, Brunger M J and Buckman S J *New Journal of Physics* **9** 41 (2007)

[81] Winstead C and McKoy V *The Journal of Chemical Physics* **125** 074302-6 (2006)

[82] Możejko P, Ptasinska-Denga E, Domaracka A and Szmytkowski C *Physical Review A: Atomic, Molecular, and Optical Physics* **74** 012708-5 (2006)

[83] Zecca A, Perazzolli C and Brunger M J *Journal of Physics B: Atomic, Molecular and Optical Physics* **38** 2079-86 (2005)

[84] Shelton W N, Baluja K L and Watson C E *Journal of Physics B: Atomic and Molecular Physics* **4** 71 (1971)

[85] Jarczyk L, Okołowicz J, Strzałkowski A, Bodek K, Hugi M, Lang L, Müller R and Ungricht E *Nuclear Physics A* **316** 139-45 (1979)

[86] Fujimoto M M, Michelin S E, Arretche F, Mazon K T, Lee M-T and Iga I *Journal of the Brazilian Chemical Society* **21** 226-33 (2010)

[87] Trevisan C S, Orel A E and Rescigno T N *Journal of Physics B: Atomic, Molecular and Optical Physics* **39** L255-L60 (2006)

[88] Woodruff D and Delchar T A *Modern Techniques of Surface Science* (Cambridge: Cambridge University Press) (1999)

[89] Joachain C J *Quantum Collision Theory* (Amsterdam: North-Holland Physics Publishing) (1983)

[90] McCarthy I E and Weigold E *Electron-atom collisions* (Cambridge: Cambridge University Press) (1995)

[91] McCarthy I E *Australian Journal of Physics* **48** 1 (1995)

[92] Ehrhardt H, Jung K, Knoth G and Schlemmer P *Zeitschrift für Physik D* **1** 3-32 (1986)

[93] Röder J, Ehrhardt H, Bray I and Fursa D V *Journal of Physics B: Atomic, Molecular and Optical Physics* **30** 1309 (1997)

[94] McCarthy I E and Weigold E *Advances In Atomic, Molecular, and Optical Physics,*(ed D Bates and B Bederson:Academic Press) **Volume 27** 201-44 (1990)

[95] Weigold E and McCarthy I E *Electron Momentum Spectroscopy* (New York: Kluwer Academic/Plenum) (1999)

[96] Berakdar J and Briggs J S *Journal of Physics B: Atomic and Molecular Physics* **29** 2289 (1996)

[97] Haynes M A and Lohmann B *Journal of Physics B: Atomic, Molecular and Optical Physics* **34** L131 (2001)

[98] Murray A J and Read F H *Physical Review Letters* **69** 2912 (1992)

[99] Murray A J and Read F H *Physical Review A: Atomic, Molecular, and Optical Physics* **47** 3724 (1993)

[100] Nixon K L, Murray A J and Kaiser C *Journal of Physics B: Atomic, Molecular and Optical Physics* **43** 085202 (2010)

[101] McCarthy I E and Weigold E *Physical Review A: Atomic, Molecular, and Optical Physics* **31** 160 (1985)

[102] Hood S T, McCarthy I E, Teubner P J O and Weigold E *Physical Review A: Atomic, Molecular, and Optical Physics* **8** 2494 (1973)

[103] McCarthy I E and Weigold E *Physics Reports* **27** 275-371 (1976)

[104] Röder J, Rasch J, Jung K, Whelan C T, Ehrhardt H, Allan R J and Walters H R J *Physical Review A: Atomic, Molecular, and Optical Physics* **53** 225 (1996)

[105] Whelan C T, Walters H R J and Allan R J *Journal of Physics (France) IV* **3** C6-39 (1993)

[106] Whelan C T, Allan R J, Rasch J, Walters H R J, Zhang X, Roder J, Jung K and Ehrhardt H *Physical Review A: Atomic, Molecular, and Optical Physics* **50** 4394 (1994)

[107] Cavanagh S J Electron coincidence studies of atoms and molecules. Griffith University p 140 (1999)

[108] Milne-Brownlie D S Electron coincidence studies of molecules. Griffith University p 138 (2007)

[109] Ramsey N F *Molecular Beams* (New York: Oxford University Press Inc.) (1956)

[110] Heddle D W O *Electrostatic Lens Systems* (Bristol: Adam Hilger) (1991)

[111] Granneman E H A and Weil M J V D *Handbook on syncrotron radiation,* Amsterdam:North-Holland Publishing) **1**(1983)

[112] Dupre C, Lahmam-Bennani A and Duguet A *Measurement Science and Technology* **2** 327 (1991)

[113] Lahmam-Bennani A, Wellenstein H F, Duguet A and Lecas M *Review of Scientific Instruments* **56** 43-51 (1985)

[114] Brunt J N H and et al. *Journal of Physics E: Scientific Instruments* **10** 134 (1977)

[115] Werme L O, Bergmark T and Siegbahn K *Physica Scripta* **8** 149 (1973)

[116] Panajotovic R, Filipovic D, Marinkovic B, Pejcev V, Kurepa M and Vuskovic L *Journal of Physics B: Atomic and Molecular Physics* **30** 5877 (1997)

[117] McCarthy I E, Noble C J, Phillips B A and Turnbull A D *Physical Review A: Atomic, Molecular, and Optical Physics* **15** 2173 (1977)

[118] Shyn T W and Sharp W E *Physical Review A: Atomic, Molecular, and Optical Physics* **19** 557 (1979)

[119] Bray I *Private Communication* (2010)

[120] Bray I and Fursa D V *Journal of Physics B: Atomic and Molecular Physics* **30** 757 (1997)

[121] Bray I and Stelbovics A T *Physical Review Letters* **70** 746 (1993)

[122] Bray I and Stelbovics A T *Physical Review A: Atomic, Molecular, and Optical Physics* **46** 6995 (1992)

[123] Pilling S, Santos A C F, Wolff W, Sant'Anna M M, Barros A L F, de Souza G G B, de Castro Faria N V and Boechat-Roberty H M *Monthly Notices of the Royal Astronomical Society* **372** 1379-88 (2006)

[124] Gutowski M, Skurski P and Simons J *Journal of the American Chemical Society* **122** 10159-62 (2000)

[125] Linstrom P J and Mallard W G eds *NIST Chemistry WebBook, NIST Standard Reference Database Number 69* (National Institute of Standards and Technology, Gaithersburg MD, 20899)

[126] Aflatooni K, Hitt B, Gallup G A and Burrow P D *The Journal of Chemical Physics* **115** 6489-94 (2001)

[127] Tronc M, Allan M and Edard F *Abstract of Contributed Papers, XVth ICPEAC* 335 (1987)

[128] Kimura M, Sueoka O, Hamada A and Itikawa Y *Advances in Chemical Physics* **3** 537 (2004)

[129] Ari T and Haluk Guven M *Journal of Electron Spectroscopy and Related Phenomena* **106** 29-35 (2000)

[130] http://en.wikipedia.org/w/index.php?title=Formic_acid&oldid=400109236 Wikipedia, The Free Encyclopedia (2010)

[131] http://en.wikipedia.org/w/index.php?title=Acetic_acid&oldid=399665895 Wikipedia, The Free Encyclopedia (2010)

[132] http://en.wikipedia.org/w/index.php?title=Amino_acid&oldid=402005603 Wikipedia, The Free Encyclopedia (2010)

[133] Allan M *Journal of Physics B: Atomic, Molecular and Optical Physics* **39** 2939-47 (2006)

[134] Bharathi S M, Datta S K, Grisogono A M, Pascual R, Weigold E and von Niessen W *Journal of Electron Spectroscopy and Related Phenomena* **53** 51-78 (1990)

[135] Nixon K L, Lawrance W D, Jones D B, Euripidies P, Saha S, Wang F and Brunger M J *Chemical Physics Letters* **451** 18-24 (2008)

[136] Nixon K L, Lawrance W D and Brunger M J *Chemical Physics Letters* **474** 23-7 (2009)

[137] Gianturco F A and Lucchese R R *New Journal of Physics* **6** 66 (2004)

[138] von Niessen W, Bieri G and Åsbrink L *Journal of Electron Spectroscopy and Related Phenomena* **21** 175-91 (1980)

[139] Al-Hagan O, Kaiser C, Madison D and Murray A J *Nature Physics* **5** 59-63 (2009)

[140] Thiemer B, Andreesen J R and Schräder T *Archives of Microbiology* **179** 266-77 (2003)

[141] Lepage M, Letarte S, Michaud M, Motte-Tollet F, Hubin-Franskin M J, Roy D and Sanche L *The Journal of Chemical Physics* **109** 5980-6 (1998)

[142] Breton S P, Michaud M, Jaggle C, Swiderek P and Sanche L *The Journal of Chemical Physics* **121** 11240-9 (2004)

[143] Milosavljevic A R, Giuliani A, Sevic D, Hubin-Franskin M J and Marinkovic B P *The European Physical Journal D: Atomic, Molecular, Optical and Plasma Physics* **35** 411-6 (2005)

[144] Dampc M, Milosavljević, R. A, Linert I, Marinković B P and Zubek M *Physical Review A: Atomic, Molecular, and Optical Physics* **75** 042710-7 (2007)

[145] Allan M *Journal of Physics B: Atomic, Molecular and Optical Physics* **40** 3531-44 (2007)

[146] Możejko P and Sanche L *Radiation Physics and Chemistry* **73** 77-84 (2005)

[147] Bouchiha D, Gorfinkiel J D, Caron L G and Sanche L *Journal of Physics B: Atomic, Molecular and Optical Physics* **39** 975-86 (2006)

[148] Tonzani S and Greene C H *The Journal of Chemical Physics* **124** 054312-11 (2006)

[149] Yang T, Su G, Ning C, Deng J, Wang F, Zhang S, Ren X and Huang Y *Journal of Physical Chemistry A* **111** 4927-33 (2007)

[150] Ning C G, Huang Y R, Zhang S F, Deng J K, Liu K, Luo Z H and Wang F *Journal of Physical Chemistry A* **112** 11078-87 (2008)

[151] Harris D O, Engerholm G G, Tolman C A, Luntz A C, Keller R A, Kim H and Gwinn W D *The Journal of Chemical Physics* **50** 2438-45 (1969)

[152] Giuliani A, Limão-Vieira P, Duflot D, Milosavljevic A R, Marinkovic B P, Hoffmann S V, Mason N, Delwiche J and Hubin-Franskin M J *The European Physical Journal D: Atomic, Molecular, Optical and Plasma Physics* **51** 97-108 (2009)

[153] Dampc M, Mielewska B, Siggel-King M R F, King G C and Zubek M *Chemical Physics* **359** 77-81 (2009)

[154] Yamauchi M, Yamakado H and Ohno K *Journal of Physical Chemistry A* **101** 6184-94 (1997)

[155] Duffy P, Sordo J A and Wang F *The Journal of Chemical Physics* **128** 125102 (2008)

[156] Lahmam-Bennani A, Wellenstein H F, Duguet A and Rouault M *Journal of Physics B: Atomic and Molecular Physics* **16** 121 (1983)

[157] Vizcaino V, Roberts J, Sullivan J P, Brunger M J, Buckman S J, Winstead C and McKoy V *New Journal of Physics* **10** 053002 (2008)

[158] Marinković B P, Blanco F, Šević D, Pejčev V, García G, Filipović D M, Pavlović D and Mason N J *International Journal of Mass Spectrometry* **277** 300-4 (2008)

[159] Maljković J B, Milosavljević A R, Blanco F, Šević D, García G and Marinković B P *Physical Review A: Atomic, Molecular, and Optical Physics* **79** 052706 (2009)

[160] Możejko P and Sanche L *Radiation and Environmental Biophysics* **42** 201-11 (2003)

[161] http://en.wikipedia.org/w/index.php?title=DNA&oldid=401579040 Wikipedia, The Free Encyclopedia (2010)

[162] Blanco F and García G *Physics Letters A* **360** 707-12 (2007)

[163] Blanco F and García G *Journal of Physics B: Atomic, Molecular and Optical Physics* **42** 145203 (2009)

[164] Ning C G, Liu K, Luo Z H, Zhang S F and Deng J K *Chemical Physics Letters* **476** 157-62 (2009)

[165] Staszewska G, Schwenke D W, Thirumalai D and Truhlar D G *Physical Review A: Atomic, Molecular, and Optical Physics* **28** 2740 (1983)

[166] Blanco F and García G *Physics Letters A* **295** 178 (2002)

[167] Blanco F and García G *Physical Review A: Atomic, Molecular, and Optical Physics* **67** 022701 (2003)

[168] Blanco F and García G *Physics Letters A* **330** 230 (2004)

[169] Johnson R C, Power T D, Holt J S, Immaraporn B, Monat J E, Sissoko A A, Yanik M M, Zagorodny A V and Cybulski S M *The Journal of Physical Chemistry* **100** 18875-81 (1996)

[170] Brinkmann R T and Trajmar S *Journal of Physics E: Scientific Instruments* **14** 245 (1981)

[171] Trofimov A B, Schirmer J, Kobychev V B, Potts A W, Holland D M P and Karlsson L *Journal of Physics B: Atomic, Molecular and Optical Physics* **39** 305 (2006)

[172] Champion C *Private Communication* (2010)

[173] Champion C, Hannsen J and Hervieux P A *Physical Review A: Atomic, Molecular, and Optical Physics* **65** 022710 (2002)

[174] Muñoz A, Blanco F, García G, Thorn P A, Brunger M J, Sullivan J P and Buckman S J *International Journal of Mass Spectrometry* **277** 175-9 (2008)

[175] Read F H and Channing J M *Review of Scientific Instruments* **67** 2372-7 (1996)

[176] Stevenson M A and Lohmann B *Physical Review A: Atomic, Molecular, and Optical Physics* **73** 020701 (2006)

[177] Ullrich J, Moshammer R, Dörner R, Jagutzki O, Mergel V, Schmidt-Böcking H and Speilberger L *Journal of Physics B: Atomic, Molecular and Optical Physics* **30** 2917 (1997)

[178] Ullrich J, Moshammer R, Dorn A, Dörner R, Schmidt L P H and Schmidt-Böcking H *Reports on Progress in Physics* **66** 1463 (2003)

[179] Hargreaves L R, Stevenson M A and Lohmann B *Journal of Physics B: Atomic, Molecular and Optical Physics* **43** 205202 (2010)